Add on Writing

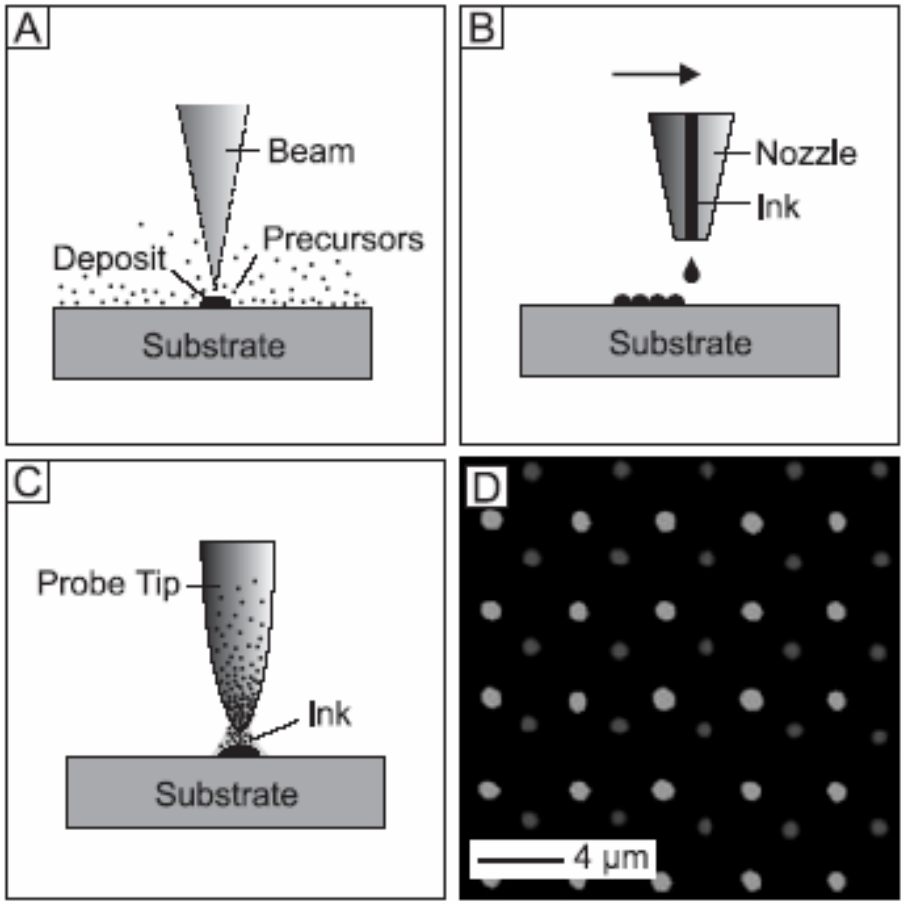

Direct Writing 3D

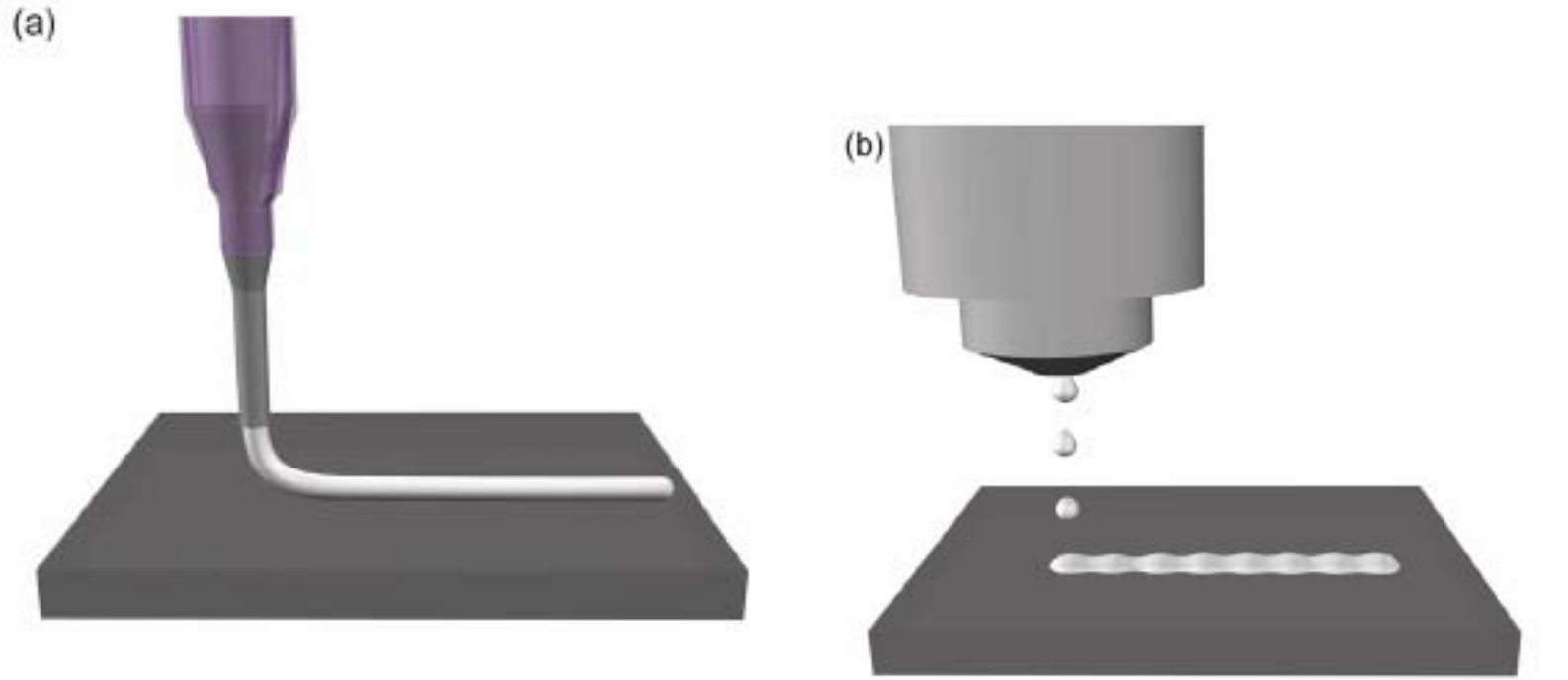

Fig. 1 Schematic view of ink-based deposition schemes: (a) droplet jetting and (b) continuous filament writing. (Reprinted from[31]. ©2002 with permission from Elsevier Ltd.)

Direct Writing

Table 1 *Capabilities of ink-writing techniques.*

Technique	Ink design	Minimum printed feature size	3-D periodic structures
Robotic Deposition[11]	Concentrated colloidal gel[13,14]	200 μm diameter	Yes
"	Concentrated nanoparticle gel[15]	100 μm diameter	Yes
"	Viscous polymer solution[16-18]	200 μm diameter	Yes
"	Concentrated polyelectrolyte complexes[3]	<1 μm	Yes
Three-dimensional printing[19]	Binder solution printed on powder bed	170 μm lateral, 45 μm depth	Yes
Ink-jet printing[20]	Dilute fluid[21]	20 μm lateral, 100 nm height	No
"	Concentrated fluid (max. solids ~40%)[22-25]	70 μm lateral, < 1 μm height	No
Fused deposition	Thermoplastic polymer melt[26]	100 μm diameter	Yes
"	Particle-filled polymer melt[27] (max. solids ~50%)	100 μm diameter	Yes
Micropen writing[28]	Concentrated, shear-thinning colloidal fluid	25 μm diameter	No
Dip-pen nanolithography[29]	Dilute fluid	20 nm	No
Scanning probe contact printing[30]	Dilute fluid	<500 nm	No

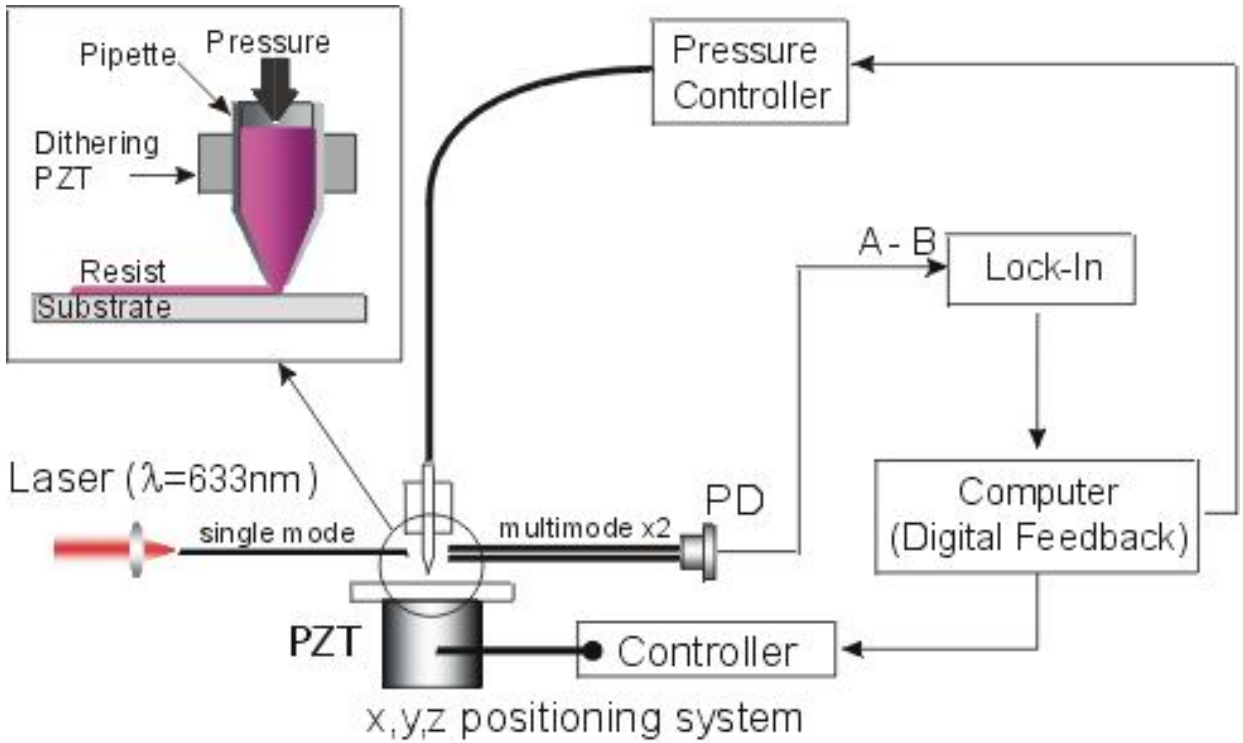
Pipette
Pressure
Dithering
PZT
Resist
Substrate
Pressure
Controller
A - B
Lock-In
Laser (λ=633nm)
single mode
multimode x2
PD
Computer
(Digital Feedback)
PZT
Controller
x,y,z positioning system

Direct Writing

NATURE | VOL 428 | 25 MARCH 2004 |

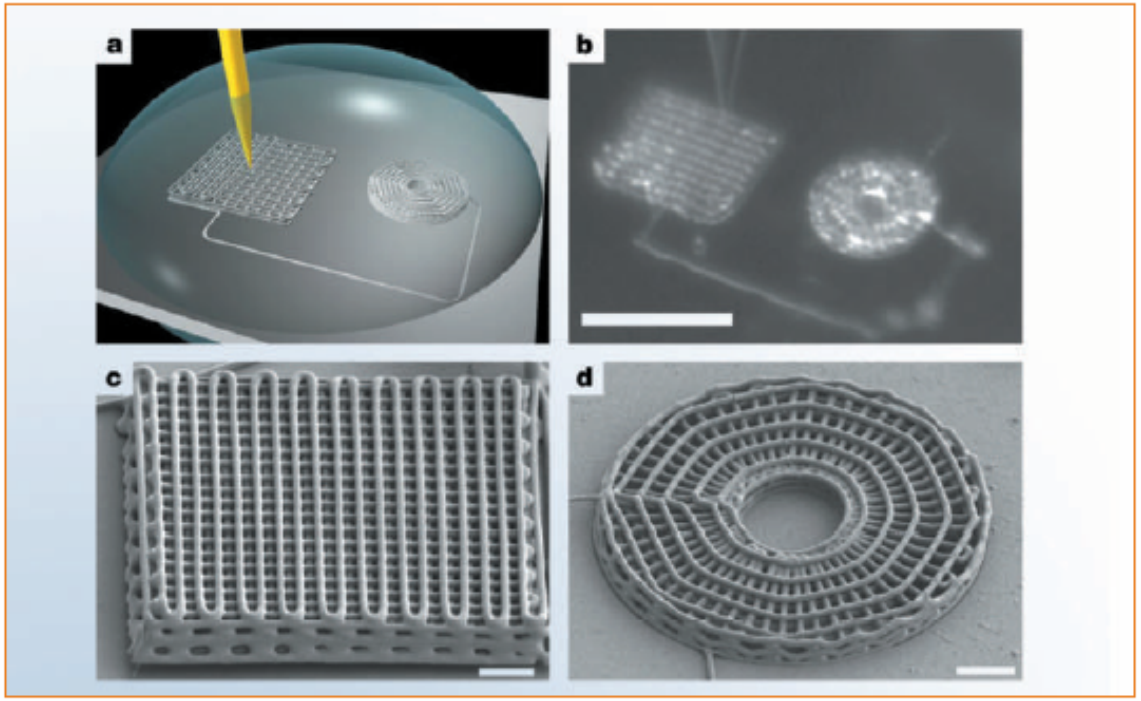

Figure 1 Direct-write assembly of three-dimensional microperiodic structures. **a,** The ink-deposition process (not drawn to scale). A concentrated polyelectrolyte ink is housed in a syringe (yellow) immersed in a coagulation reservoir (grey hemispherical drop) and deposited on to a glass substrate (light grey). **b,** Optical image acquired *in situ* during deposition reveals the features drawn in **a**, including the deposition nozzle that is patterning a three-dimensional lattice, as well as a completed radial array. This image is blurred by the reservoir (scale bar: 100 μm). **c,** Three-dimensional periodic structure with a face-centred tetragonal geometry (filament diameter: 1 μm; 10 layers; scale bar: 10 μm). **d,** Three-dimensional radial array (filament diameter: 1 μm; 5 layers; scale bar: 10 μm).

Inkjet Printer

Figure 1. Microdrop Autodrop Platform (courtesy Microdrop GmbH, Germany).

Inkjet Printing

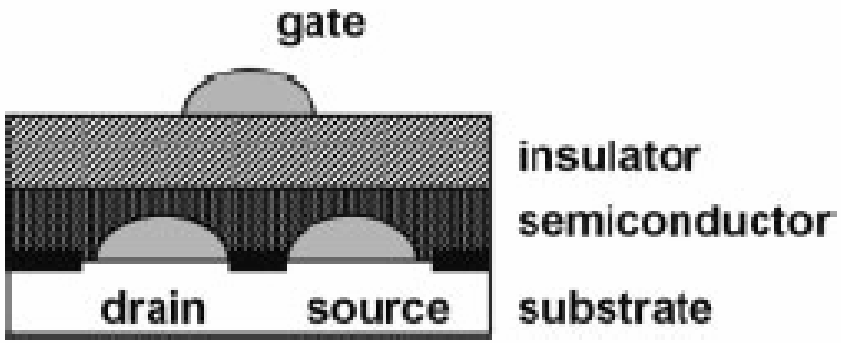

Figure 5. Schematic picture of inkjet printed all-polymer thin film transistor, as constructed by Sirringhaus et al. [41]. Source and drain electrode, consisting of PEDOT/PPS are inkjet printed on a pre-patterned surface. Two spin-coated layers of semiconducting and insulating polymer respectively cover the electrodes. Finally the gate electrode is printed on top.

Inkjet Printing

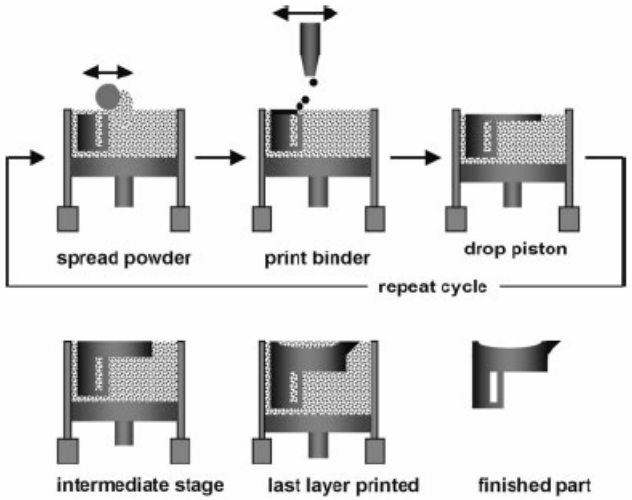

Figure 7. Schematic picture of the three-dimensional printing process.

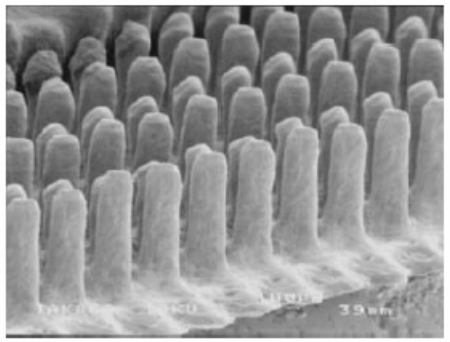

Figure 8. Electron microscopy picture of an array of pillars from lead zirconium titanate, inkjet printed by Bhatti et al. The pillars have an approximate height of 400 μm. (Reprinted from [59] with permission. Copyright 2001 Kluwer Academic Publishers).

Inkjet Printing

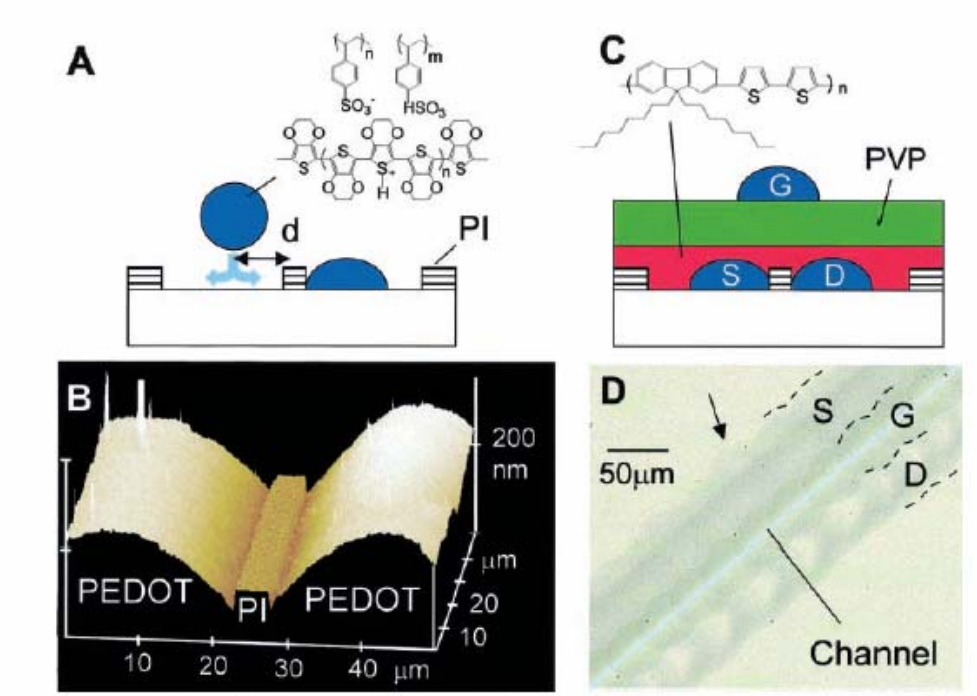

Fig. 1. (**A**) Schematic diagram of high-resolution IJP onto a prepatterned substrate. (**B**) AFM showing accurate alignment of inkjet-printed PEDOT/PSS source and drain electrodes separated by a repelling polyimide (PI) line with $L = 5$ μm. (**C**) Schematic diagram of the top-gate IJP TFT configuration with an F8T2 semiconducting layer (S, source; D, drain; and G, gate). (**D**) Optical micrograph of an IJP TFT ($L = 5$ μm). The image was taken under crossed polarizers so that the TFT channel appears bright blue because of the uniaxial monodomain alignment of the F8T2 polymer on top of rubbed polyimide. Unpolarized background illumination is used to make the contrast in the remaining areas visible, where the F8T2 film is in an isotropic multidomain configuration. The arrow indicates pronounced roughness of the unconfined PEDOT boundary.

Inkjet Printing

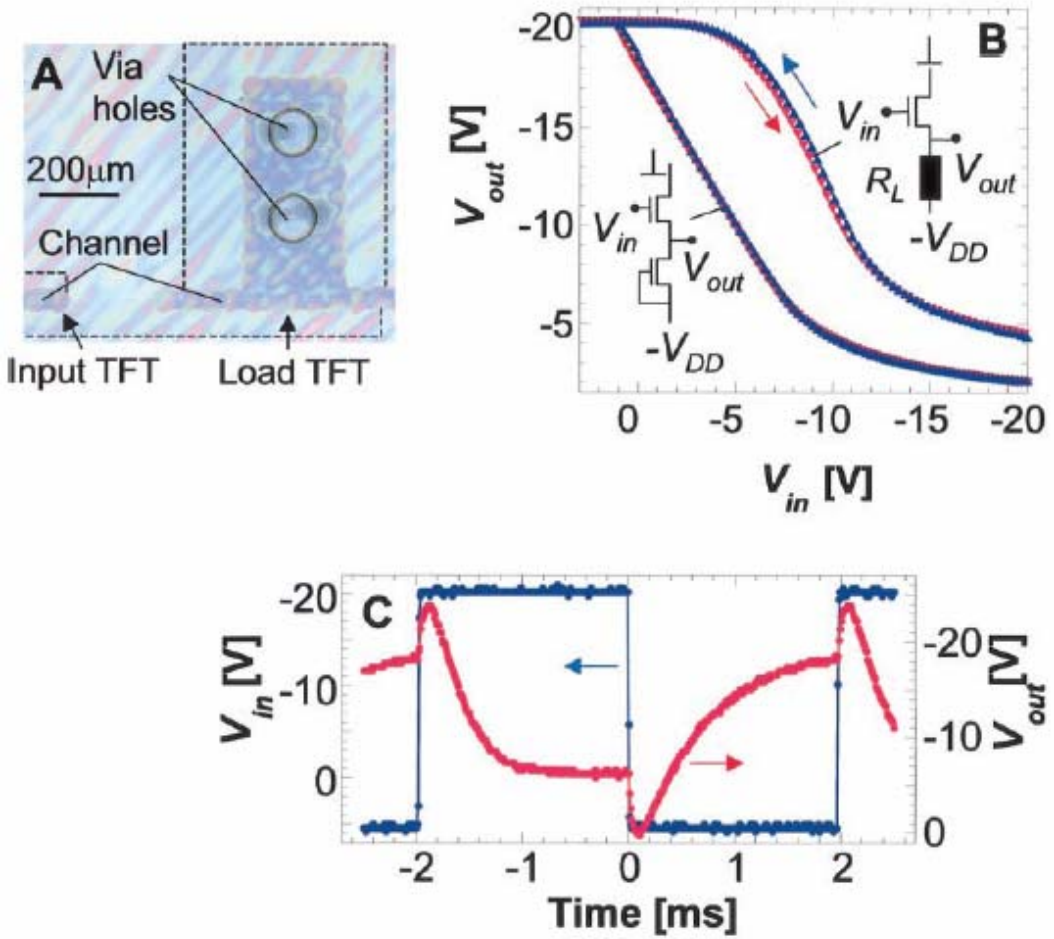

Replication

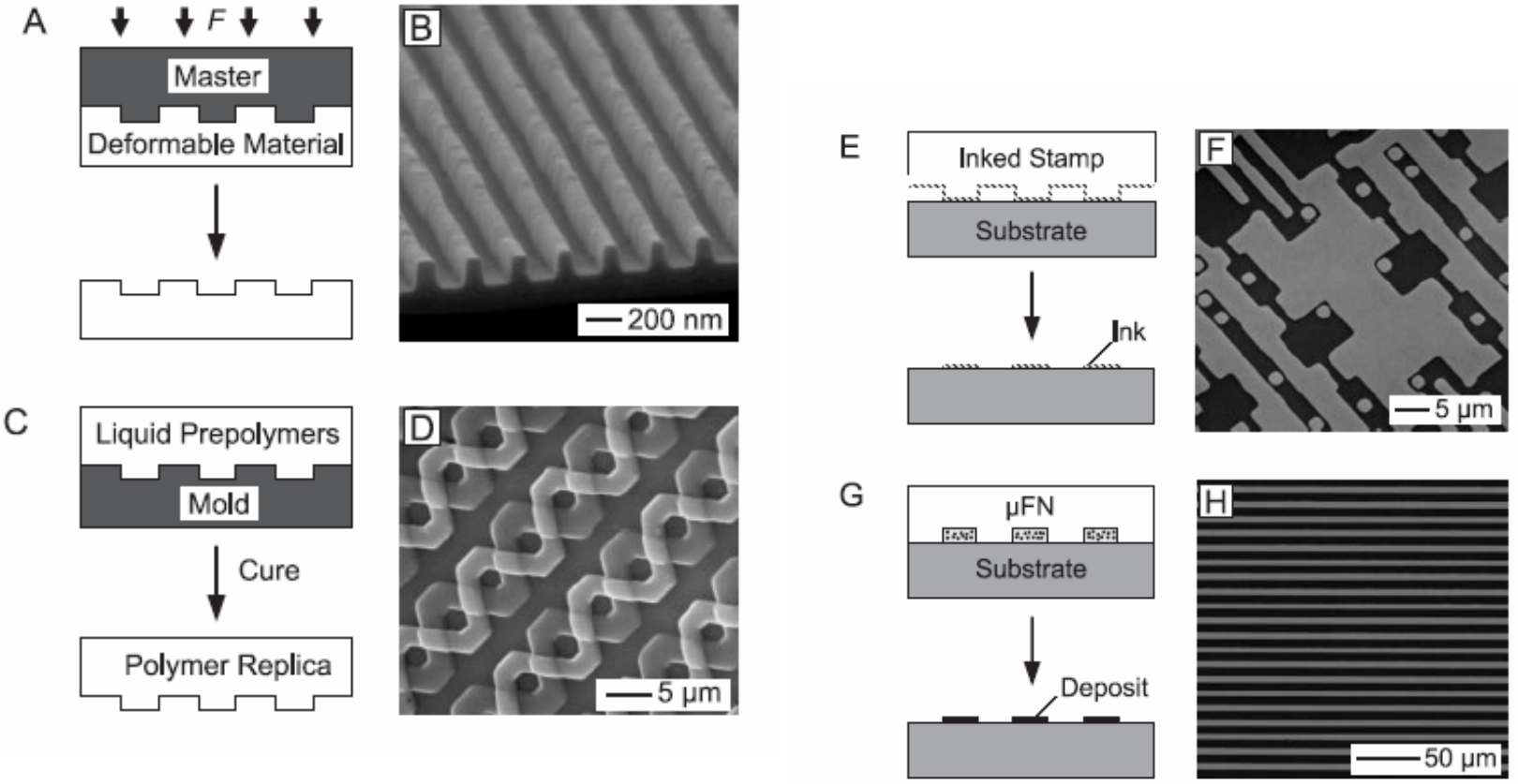

Align the pattern and Exposure

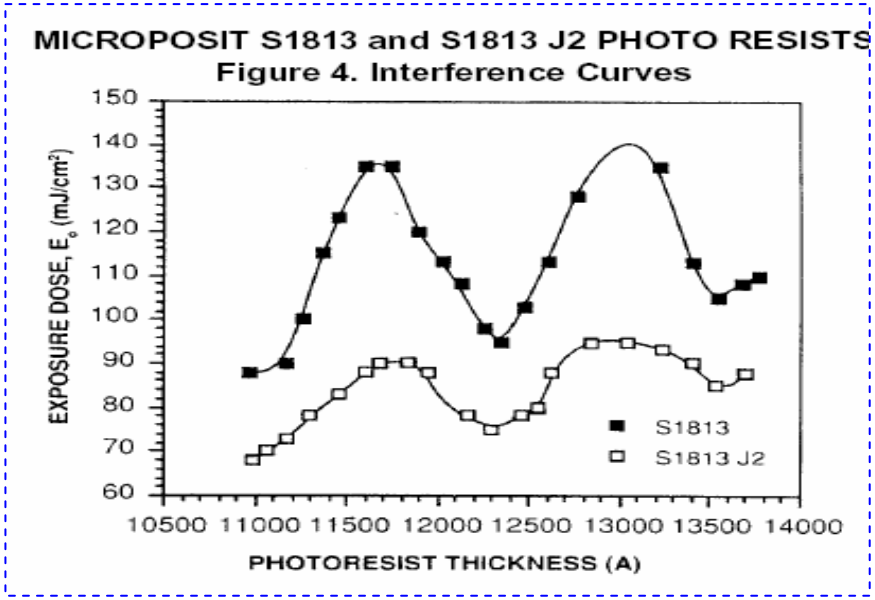

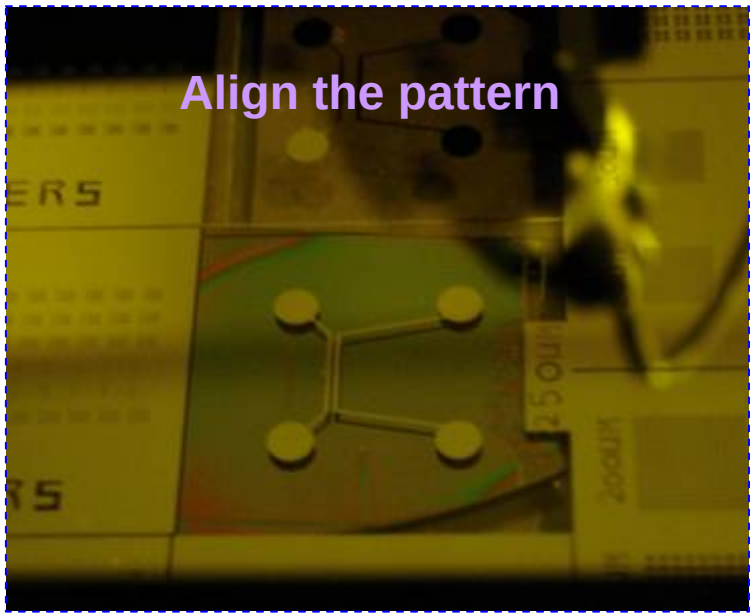

Stepper

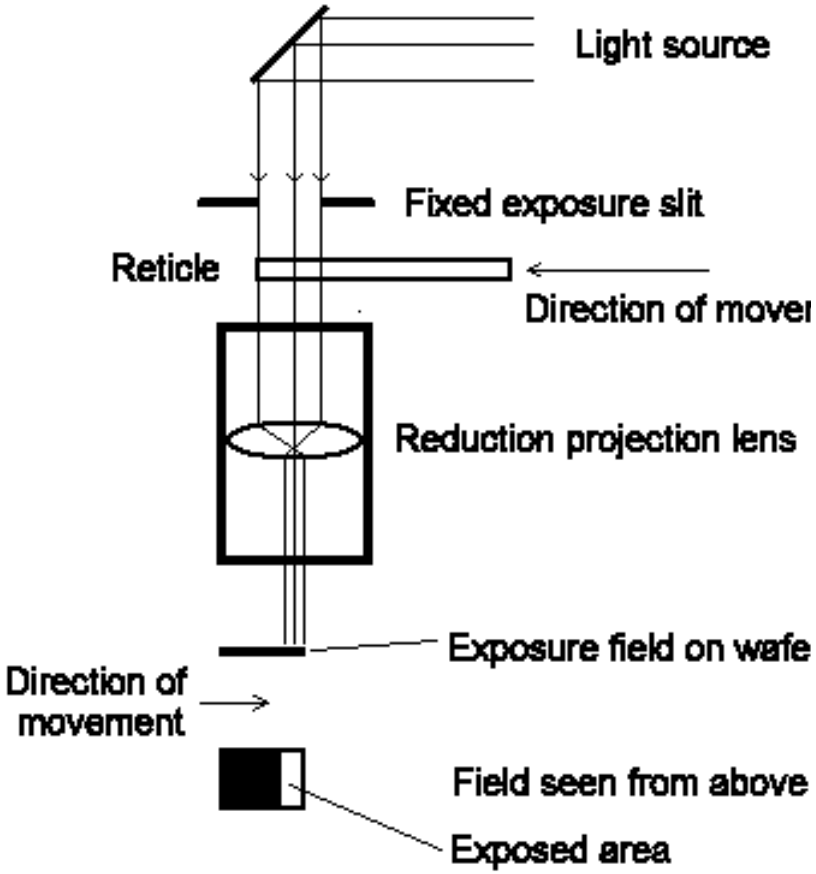
Light source
Fixed exposure slit
Reticle
Direction of move
Reduction projection lens
Exposure field on wafe
Direction of movement
Field seen from above
Exposed area

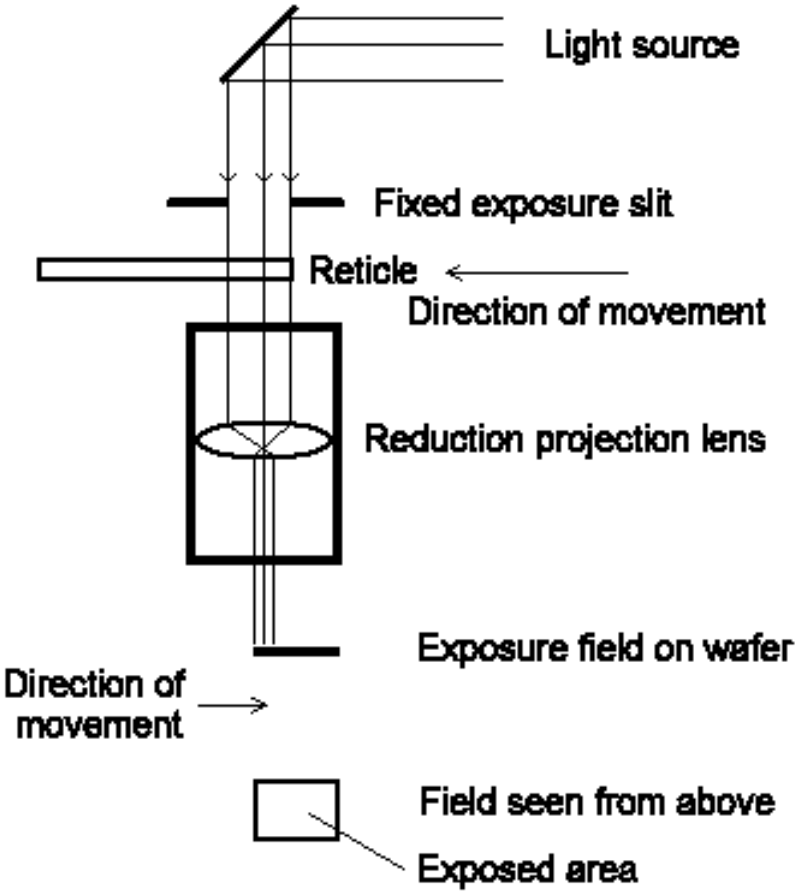
Light source
Fixed exposure slit
Reticle
Direction of movement
Reduction projection lens
Exposure field on wafer
Direction of movement
Field seen from above
Exposed area

Stepper

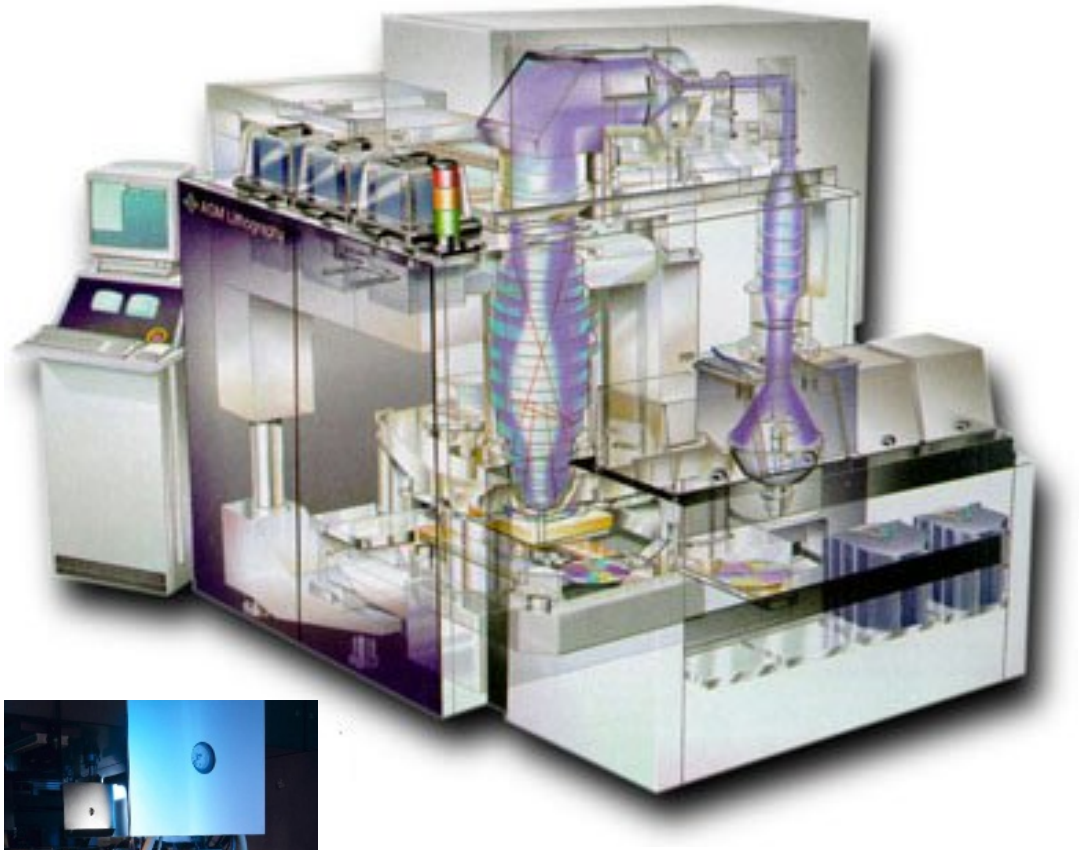

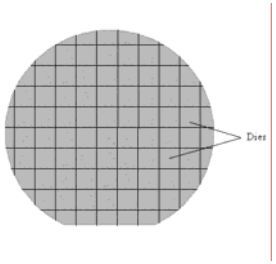
Dies

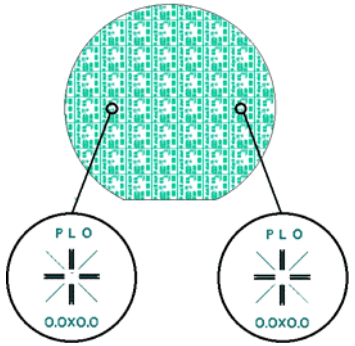
PLO
0.0X0.0
PLO
0.0X0.0

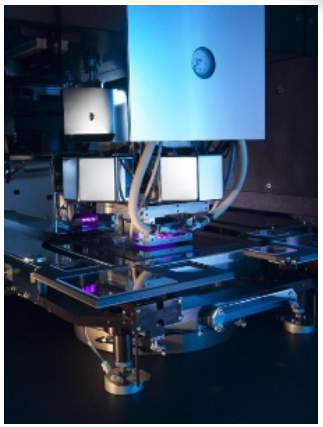

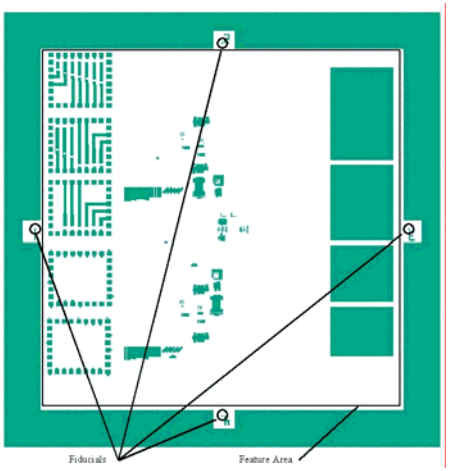
Fiducials
Feature Area

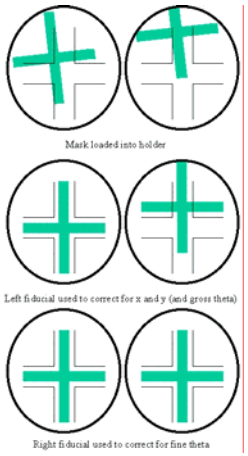
Mark loaded into holder
Left fiducial used to correct for x and y (and gross theta)
Right fiducial used to correct for fine theta

Dicing and Bonding

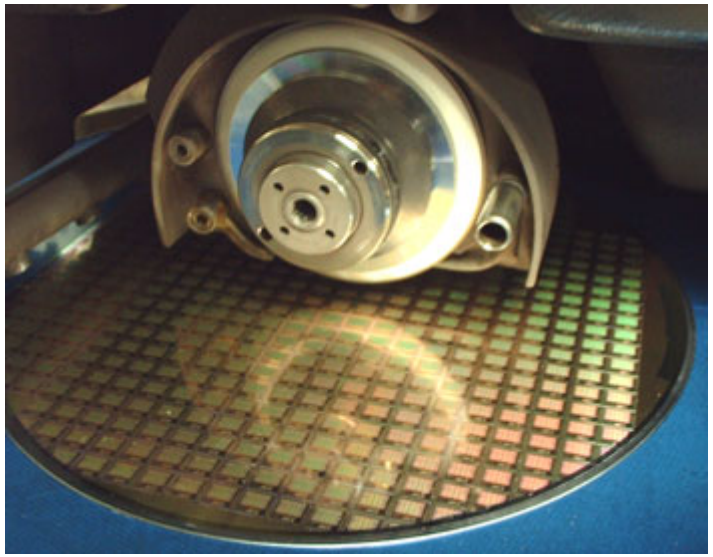

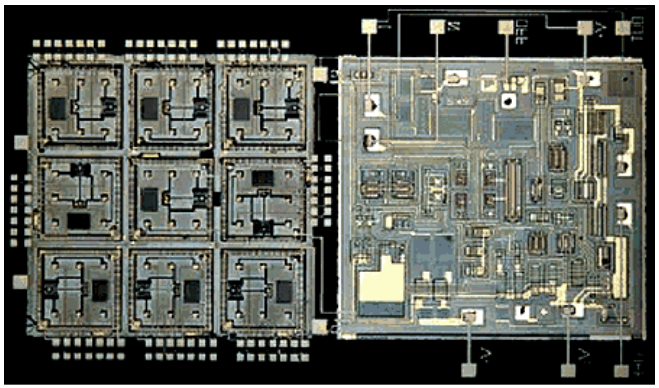

3. High-performance MEMS devices have been cost-effectively integrated with other electronic devices like amplifiers by MicroAssembly Technologies, using the company's hybrid two-chip packaging process.

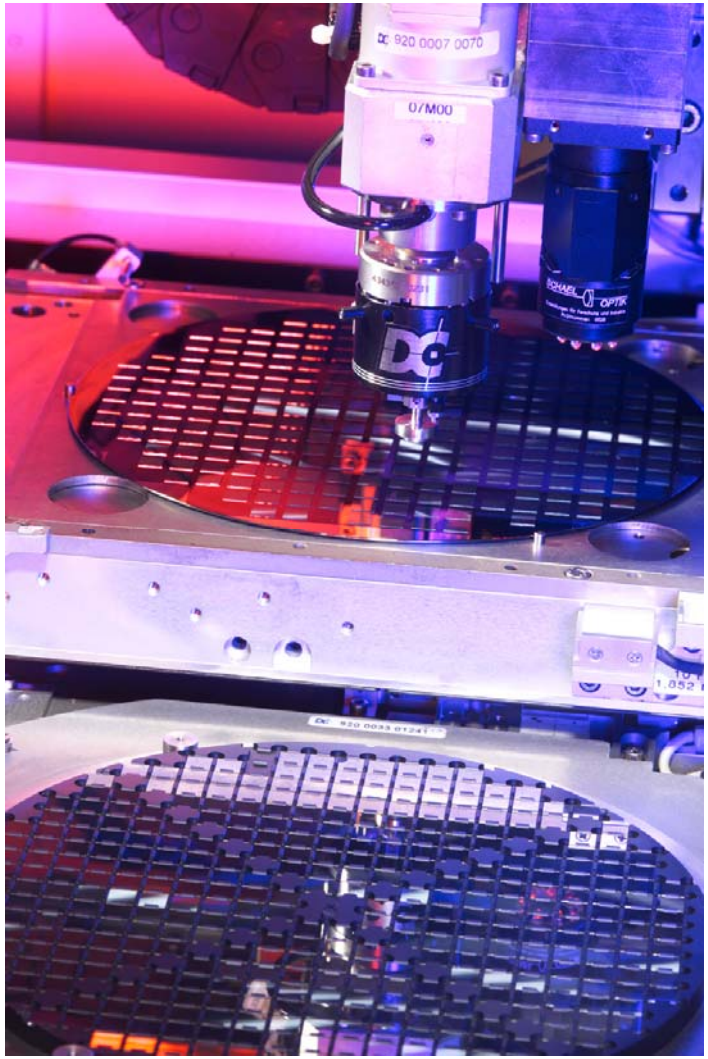

E-beam Projection

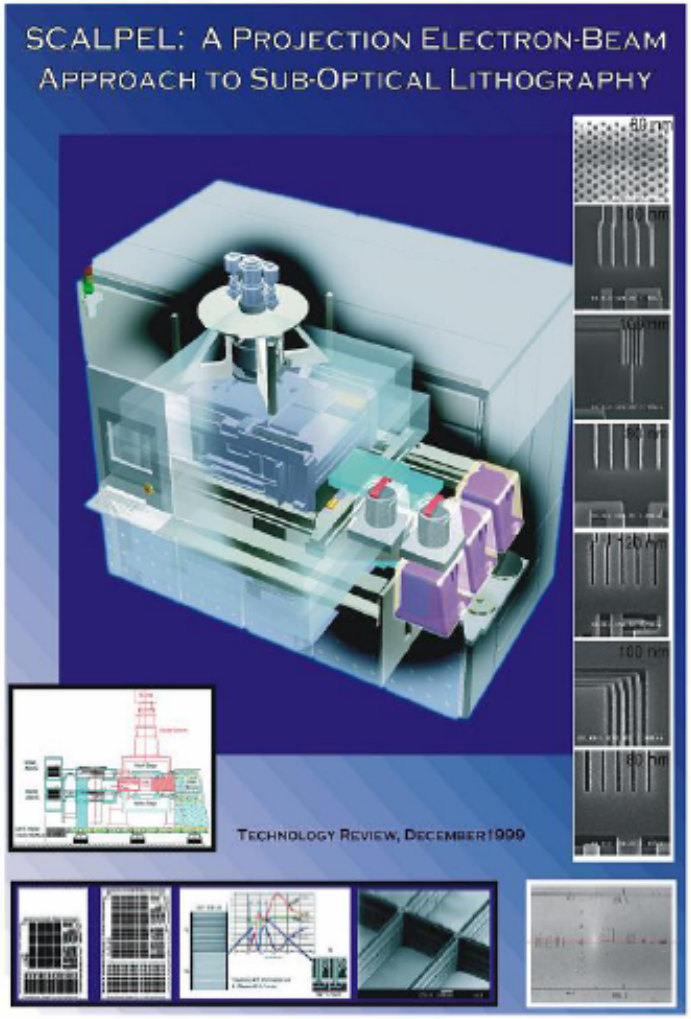

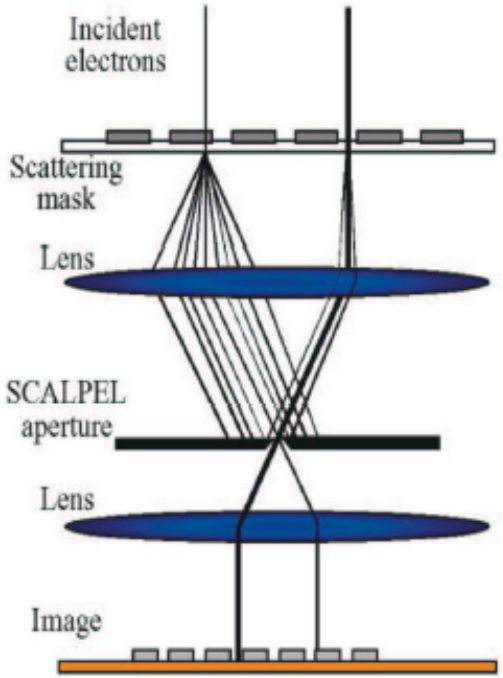

Bell Lab (1999)
There 'was' a consortium including Applied Materials, Inc. and ASM Lithography Holding N.V.; Lucent Technologies Inc.; Motorola, Semiconductor Products Sector; Samsung Electronics Co., Ltd.; and Texas Instruments Incorporated (TI).

Imprint Lithography with 25-Nanometer Resolution

Stephen Y. Chou; Peter R. Krauss; Preston J. Renstrom

Science, New Series, Volume 272, Issue 5258 (Apr. 5, 1996), 85-87.

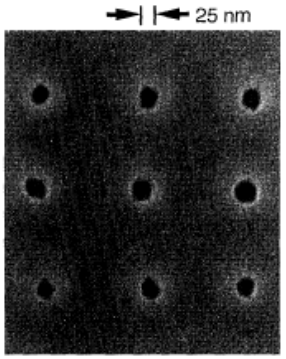

Fig. 2. SEM micrograph of a top view of holes 25 nm in diameter with a period of 120 nm, formed by compression molding into a PMMA film.

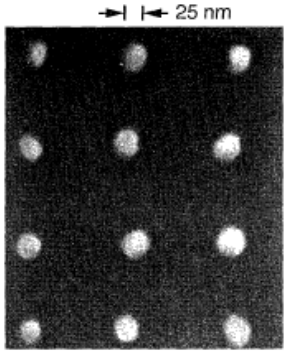

Fig. 5. SEM micrograph of the substrate in Fig. 2, after deposition of metal and a lift-off process. The diameter of the metal dots is 25 nm, the same as that of the original holes created in the PMMA.

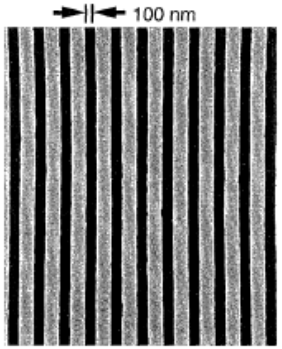

Fig. 3. SEM micrograph of a top view of trenches 100 nm wide with a period of 250 nm, formed by compression molding into a PMMA film.

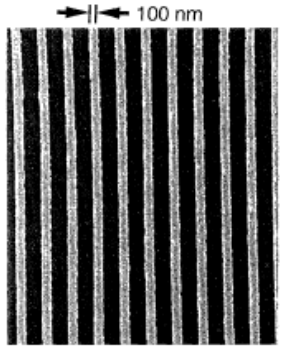

Fig. 6. SEM micrograph of the substrate in Fig. 3, after deposition of metal and a lift-off process. The metal linewidth is 100 nm, the same as the width of the original PMMA trenches.

Nanoimprint Lithography

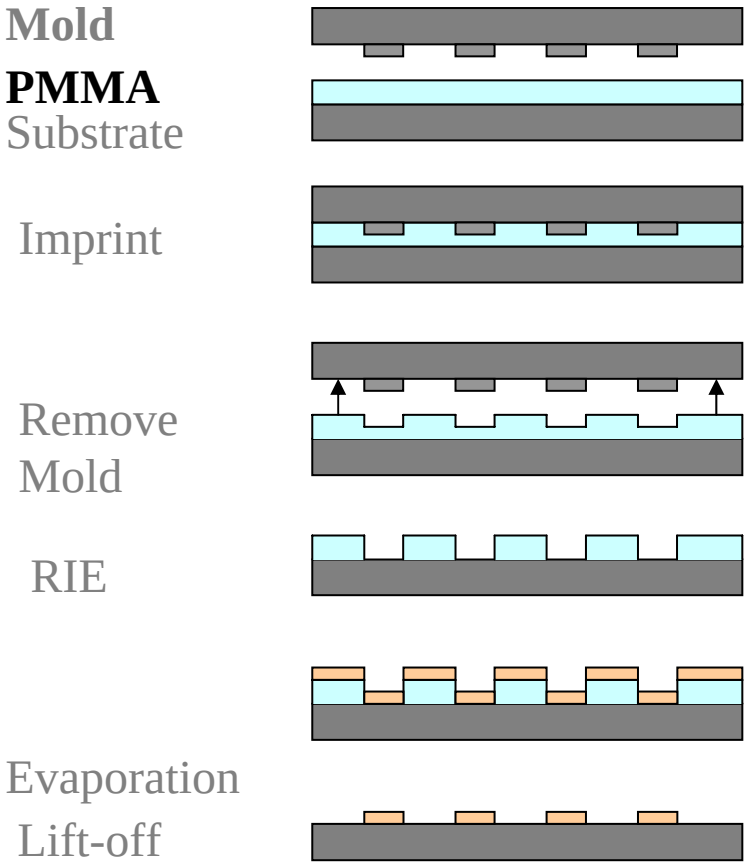

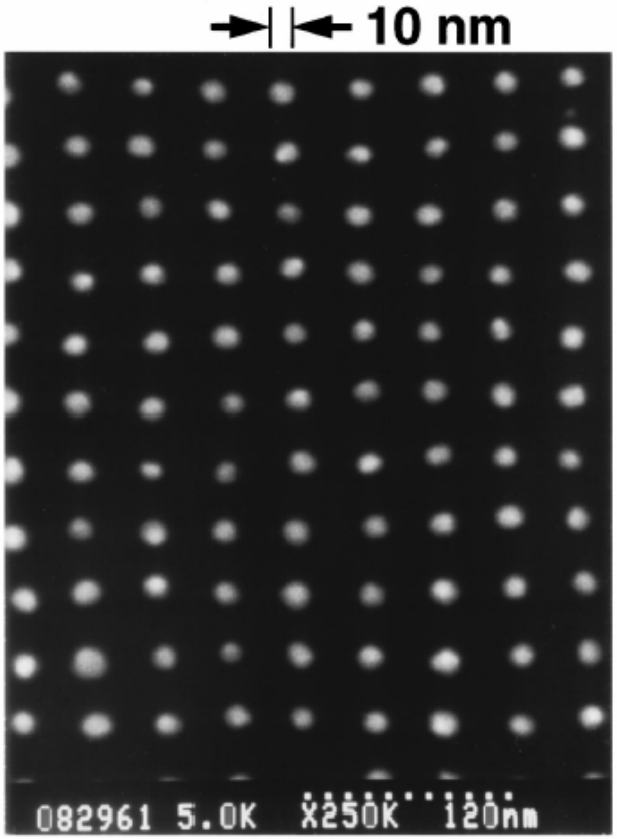

Ultrafast and direct imprint of nanostructures in silicon

NATURE | VOL 417 | 20 JUNE 2002 |

Stephen Y. Chou*, Chris Keimel & Jian Gu

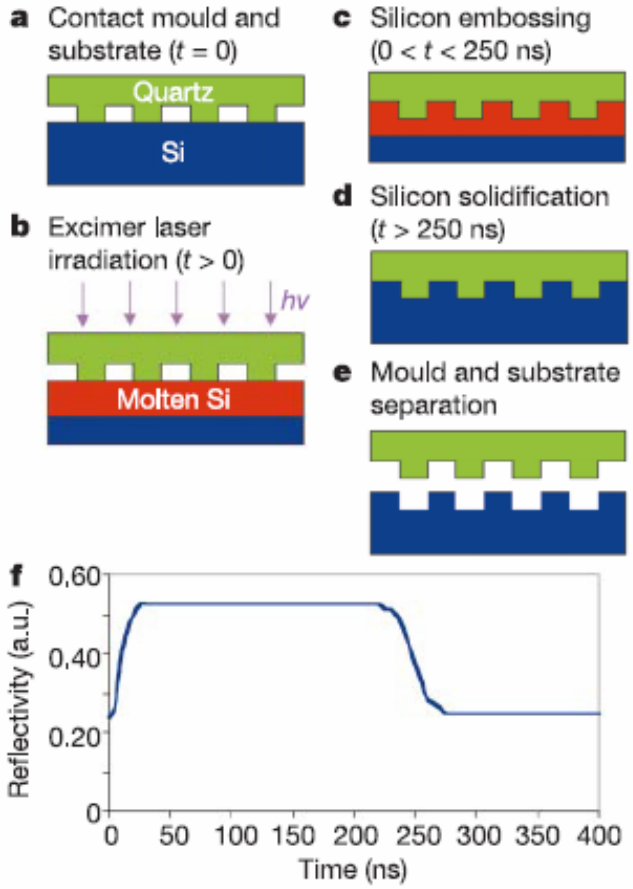

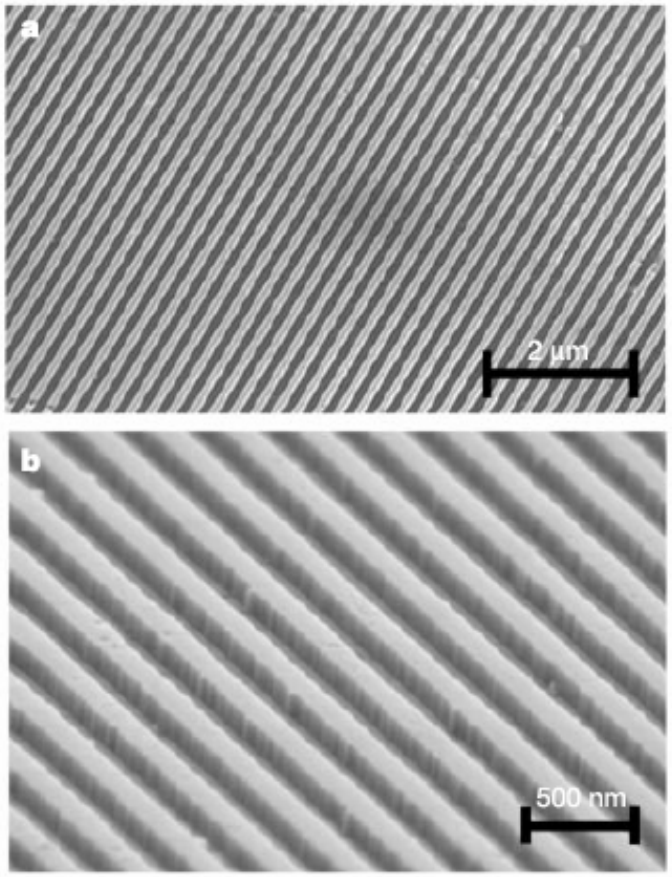

Step and Flash Imprint Lithography

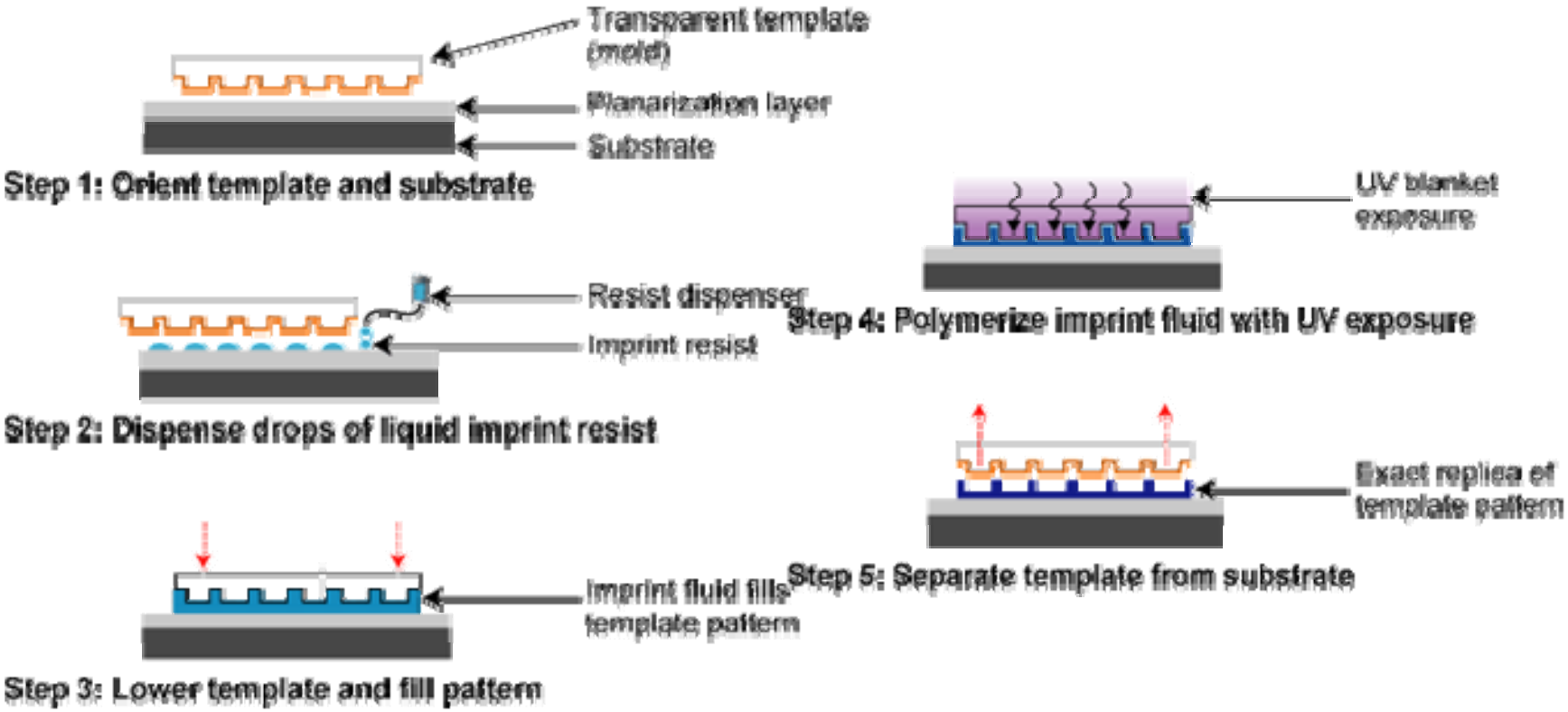

Nanoimprintors

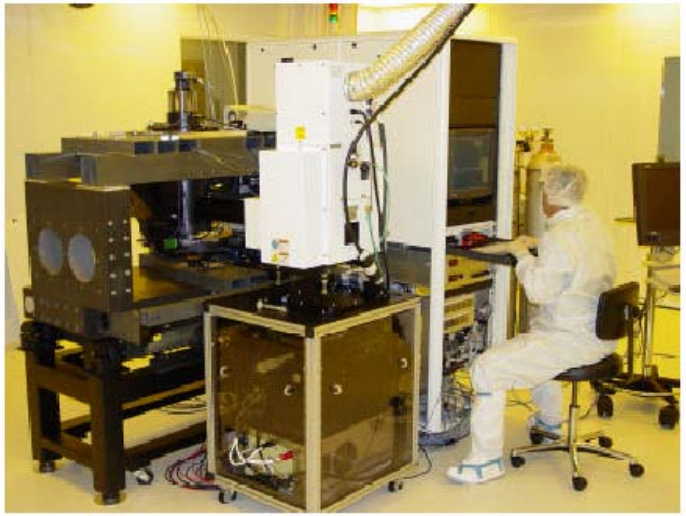

NX-2000, Nanoimprintor, Nanonex

IMPRIO 100

Molecular Imprints, Inc.™

- Resolution: Sub-50 nanometers, imprint template (mold) limited.
- Alignment: < 500 nm, 3σ (X, Y, and Rotation).
- Flexibility: Handles up to 8 inch wafers, including fragile substrates.
- Field size: 25 x 25 mm full active print area, 100 μm street width.

Imprinting Result

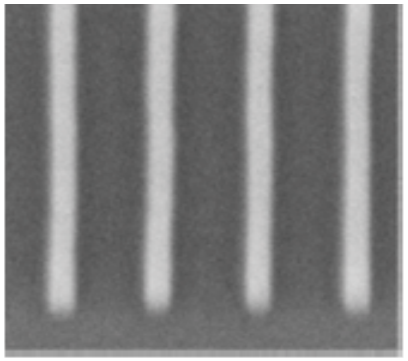

Imprinted 20 nm isolated lines

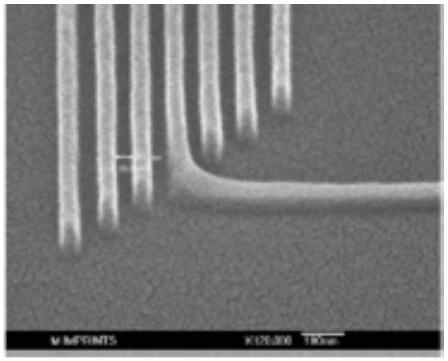

Imprinted 30 nm dense lines

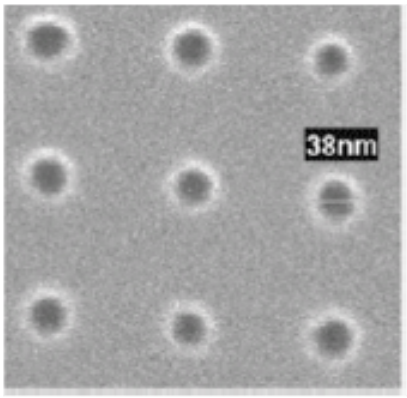

Imprinted sub-40 nm contacts

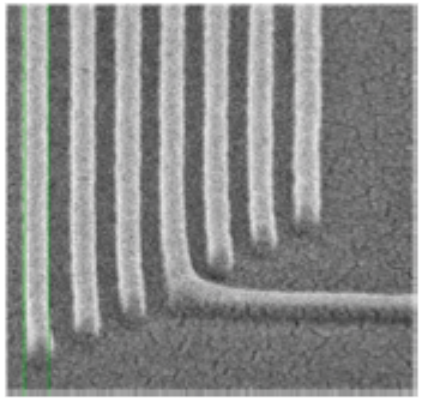

Imprinted 50 nm dense lines

Soft Lithography

Annu. Rev. Mater. Sci. 1998. 28:153–84

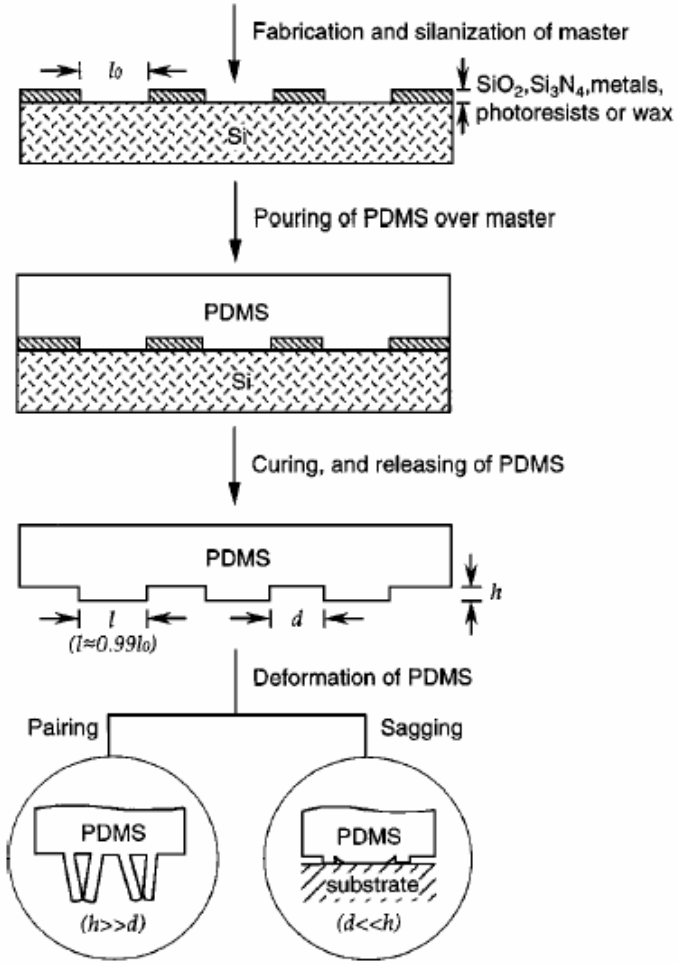

Soft Lithography

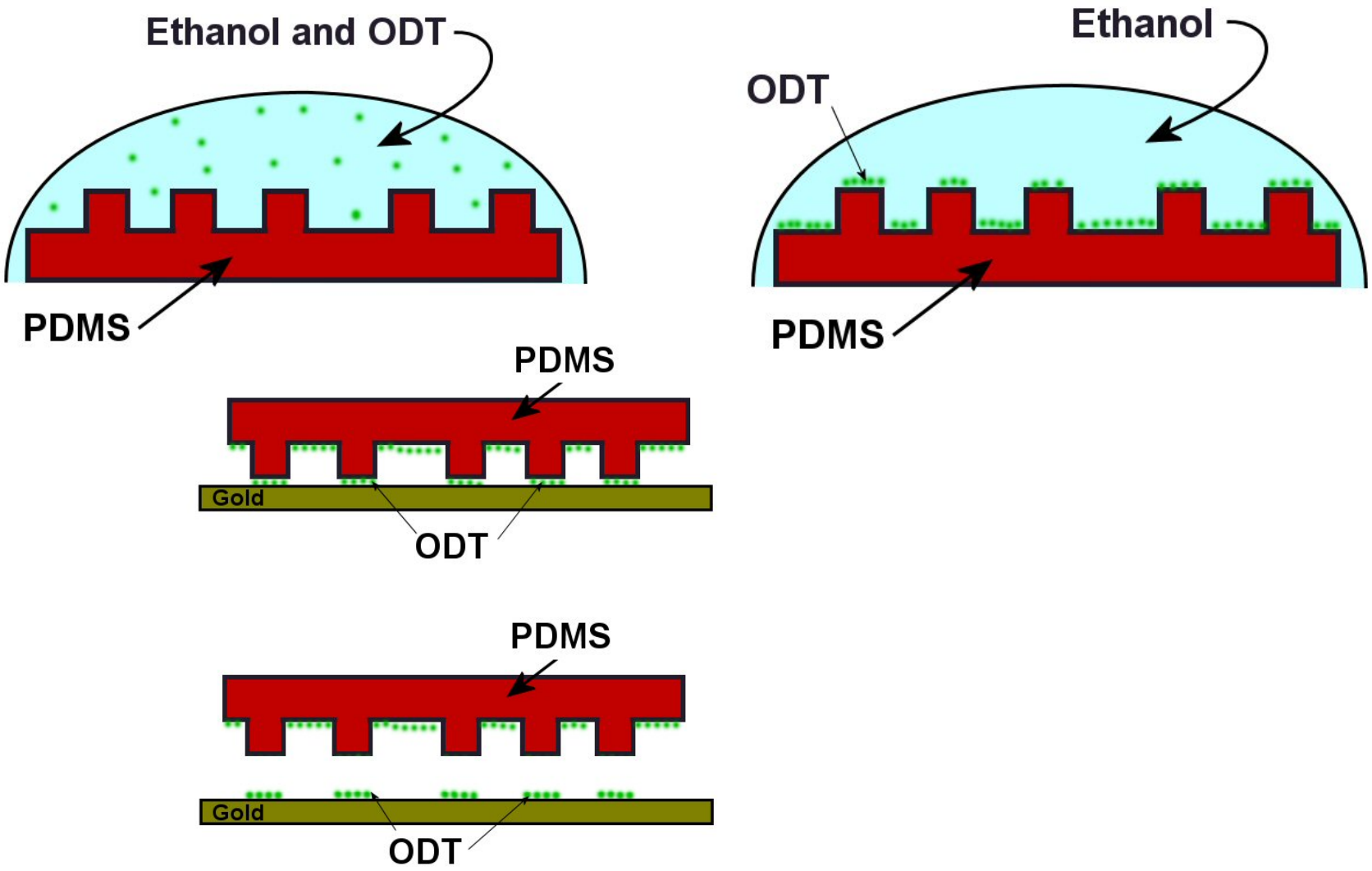

Table 1 Comparison between photolithography and soft lithography

	Photolithography	Soft lithography
Definition of patterns	Rigid photomask (patterned Cr supported on a quartz plate)	Elastomeric stamp or mold (a PDMS block patterned with relief features)
Materials that can be patterned directly	Photoresists (polymers with photo-sensitive additives)	Photoresists[a,e]
	SAMs on Au and SiO_2	SAMs on Au, Ag, Cu, GaAs, Al, Pd, and SiO_2[a] Unsensitized polymers[b–e] (epoxy, PU, PMMA, ABS, CA, PS, PE, PVC) Precursor polymers[c,d] (to carbons and ceramics) Polymer beads[d] Conducting polymers[d] Colloidal materials[a,d] Sol-gel materials[c,d] Organic and inorganic salts[d] Biological macromolecules[d]
Surfaces and structures that can be patterned	Planar surfaces 2-D structures	Both planar and nonplanar Both 2-D and 3-D structures
Current limits to resolution	~250 nm (projection) ~100 nm (laboratory)	~30 nm[a,b], ~60 nm[e], ~1 μm[d,e] (laboratory)
Minimum feature size	~100 nm (?)	10 (?) - 100 nm

[a–e]Made by (a) μCP, (b) REM, (c) μTM, (d) MIMIC, (e) SAMIM. PU:polyurethane; PMMA: poly(methyl methacrylate); ABS: poly(acrylonitrile-butadiene-styrene); CA: cellulose acetate; PS: polystyrene; PE: polyethylene; and PVC: poly(vinyl chloride)

Micro-contact Printing

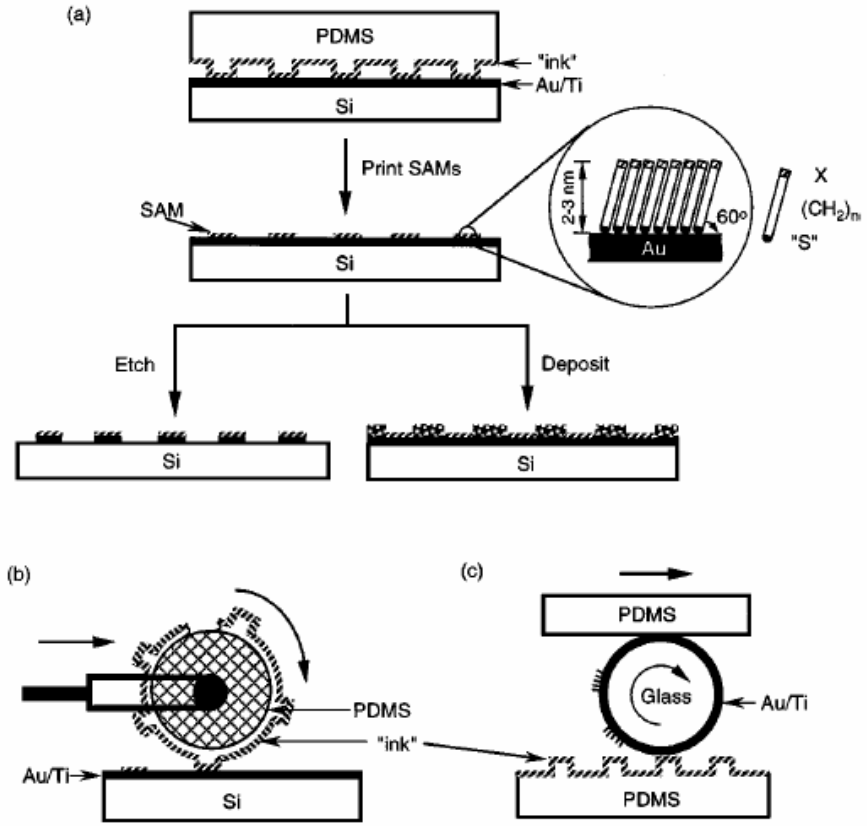

Figure 2 Schematic procedures for μCP of hexadecanethiol (HDT) on the surface of gold: (*a*) printing on a planar surface with a planar stamp (21), (*b*) printing on a planar surface over large areas with a rolling stamp (128), and (*c*) printing on a nonplanar surface with a planar stamp (174).

Micro-contact Printing

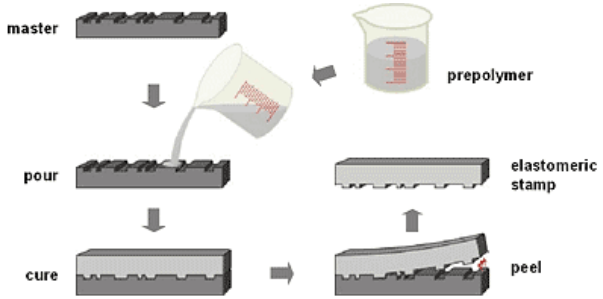

Fig.2 The stamp replication process: A master with a negative of the desired pattern is cast with a pre-polymer. After curing the polymer, the elastomeric stamp is peeled off the master and ready for microcontact printing.

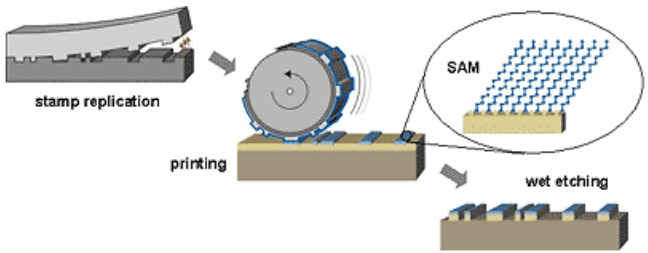

Fig.1 The microcontact printing (μCP) process: An elastomeric stamp is replicated from a master. After inking of the stamp with a suitable ink, it is fixated on a printing machine with help of which it is brought into conformal contact with a substrate. There the ink forms a self-assembled monolayer (SAM) which can be used as a resist in a subsequent wet etching step.

Micro-contact Printing

http://mrsec.wisc.edu/Edetc/nanolab/print/text.html

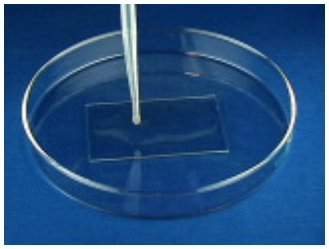

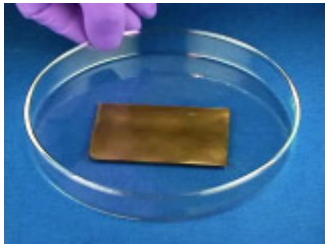

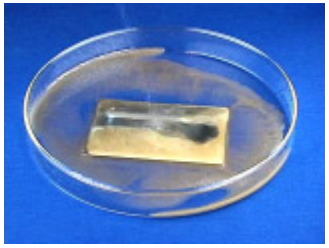

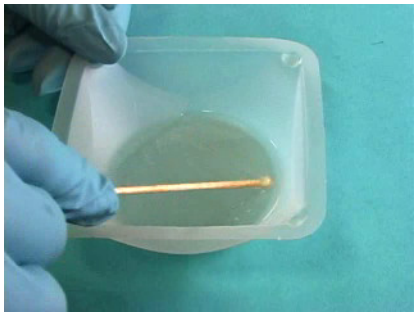

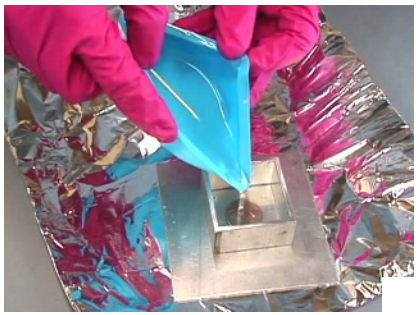

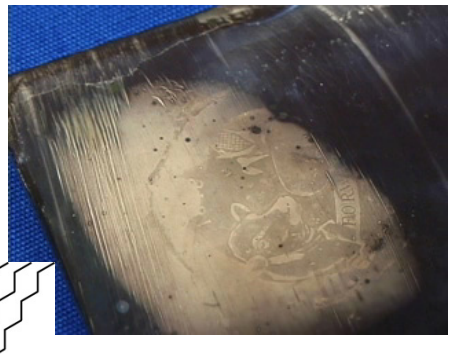

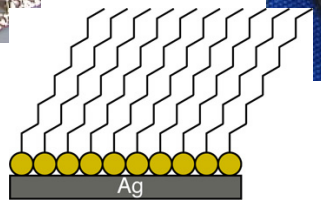

Micro-contact Printing

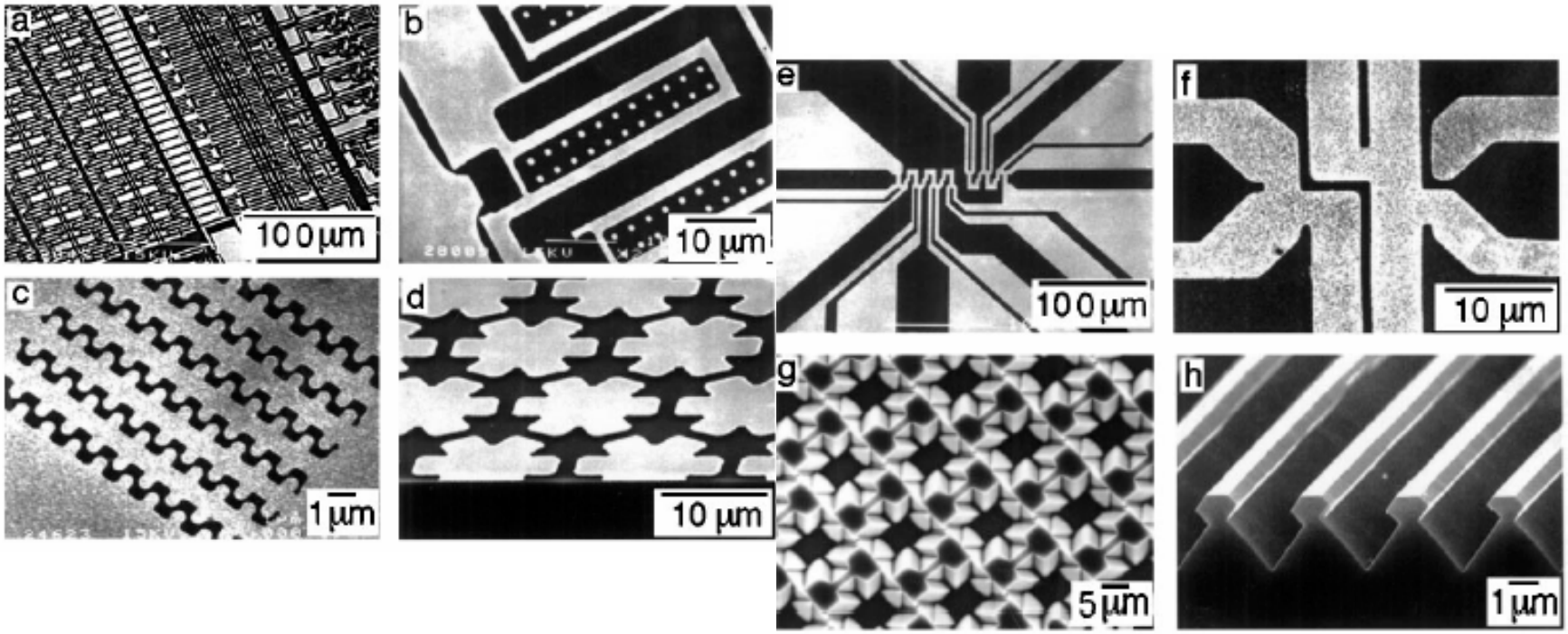

Self-Assemble Monolayer (SAM)

Chem. Rev. **2005**, *105*, 1103–1169

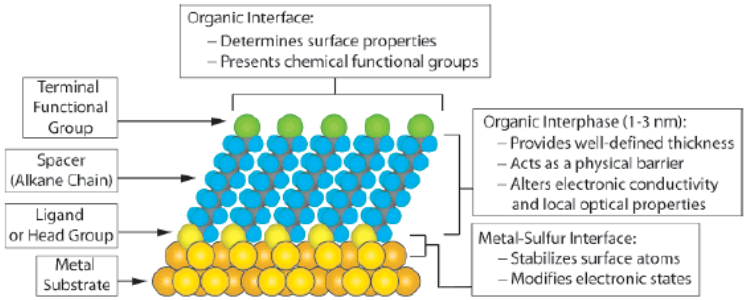

Ligand	Substrates	Morphology of Substrate: Thin Films or Bulk Material	Morphology of Substrate: Nanoparticles or Other Nanostructures
ROH	Fe_xO_y		35
	Si-H	36	
	Si	37	
RCOO-/RCOOH	α-Al_2O_3	38,39	
	Fe_xO_y		40
	Ni		41,42
	Ti/TiO_2	43	
RCOO–OOCR	Si(111):H	44	
	Si(100):H		
Ene-diol	Fe_2O_3		45
RNH_2	FeS_2	46	
	Mica	47	
	Stainless Steel 316L	48	
	$YBa_2Cu_3O_{7-\delta}$	49	
	CdSe		50
RC≡N	Ag	51	
	Au		
R-N≡N$^+$(BF_4^-)	GaAs(100)	52	
	Pd	52	
	Si(111):H	52	
RSH	Ag	26	53,54
	$Ag_{90}Ni_{10}$	55	
	AgS		56
	Au	26	57
	AuAg		58
	AuCu		58
	Au_xPd_{1-x}		58
	CdTe		59
	CdSe		60
	CdS		61,62
	Cu	26	58
	FePt		63-66
	GaAs	67	
	Ge	68	
	Hg	69-71	
	HgTe		72
	InP	73	
	Ir		74
	Ni	75	
	PbS		76-78
	Pd	30	74,79
	PdAg		58
	Pt	32	80
	Ru		81
	Stainless Steel 316L	48	
	$YBa_2Cu_3O_{7-\delta}$	82	
	Zn	83	
	ZnSe	84	
	ZnS		85
RSAc	Au	86	
R–S	Au		87
RSR'	Au	88	

Ligand	Substrates	Morphology of Substrate: Thin Films or Bulk Material	Morphology of Substrate: Nanoparticles or Other Nanostructures
RSSR'	Ag	89	90
	Au	20	90-92
	CdS		61
	Pd	30	
	Au	93	
RCSSH	Au	94	
	CdSe		95
$RS_2O_3^-Na^+$	Au	96	98
	Cu	97	
RSeH	Ag	99	
	Au	100,101	
	CdS		60
	CdSe		102
RSeSeR'	Au	101	
R_3P	Au		103
	FeS_2	46	
	CdS		104
	CdSe		104
	CdTe		104
$R_3P=O$	Co		105,106
	CdS		104
	CdSe		104
	CdTe		104
$RPO_3^{2-}/RP(O)(OH)_2$	Al	107	
	Al-OH	108	
	$Ca_{10}(PO_4,CO_3)_6(OH)_2$	109	
	GaAs	110	
	GaN	110	
	Indium tin oxide (ITO)	111	
	Mica	112	
	TiO_2	113,114	
	ZrO_2	114,115	
	CdSe		116-118
	CdTe		118,119
RPO_4^{2-}	Al_2O_3	120	
	Nb_2O_5	120	
	Ta_2O_3	121	
	TiO_2	120,122	
RN≡C	Pt	123	124
$RHC=CH_2$	Si	37	
RC≡CH	Si(111):H	125	
$RSiX_3$ X = H, Cl, OCH_2CH_3	HfO_2	126	
	ITO	127	
	PtO	128	
	TiO_2	113,126,129	
	ZrO_2	126,129	

S-Au 25-30 Kcal/mole
Si-O 190 kcal/mole

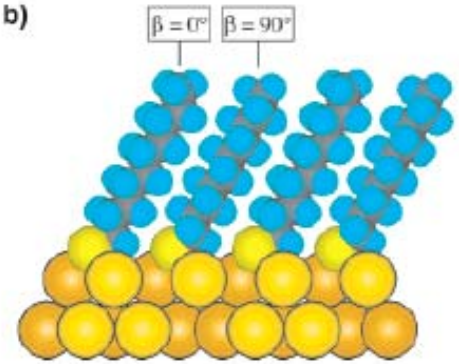

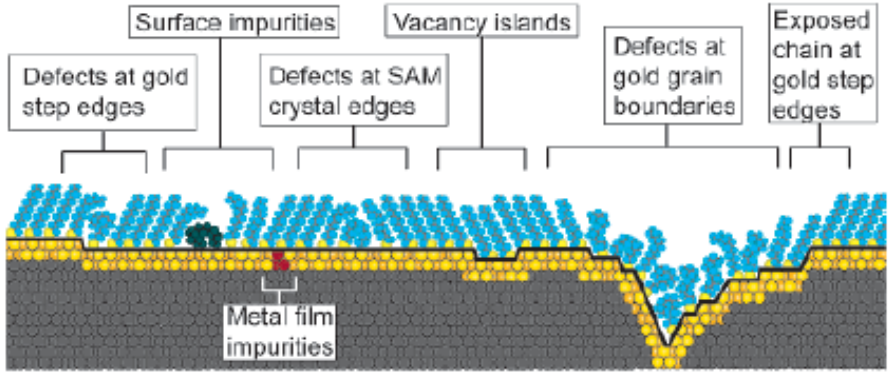

Figure 7. Schematic illustration of some of the intrinsic and extrinsic defects found in SAMs formed on polycrystalline substrates. The dark line at the metal−sulfur interface is a visual guide for the reader and indicates the changing topography of the substrate itself.

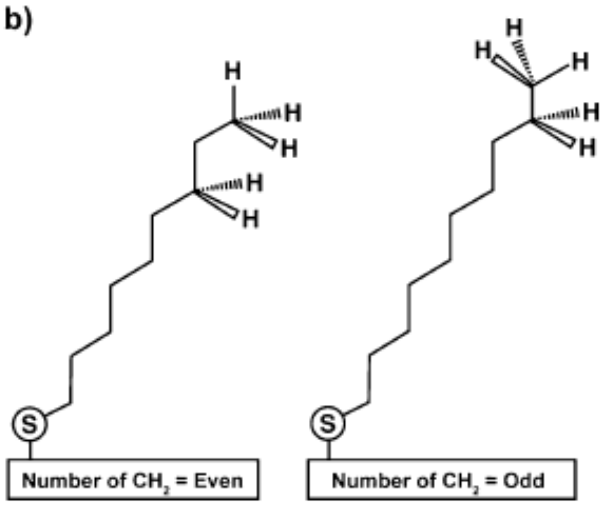

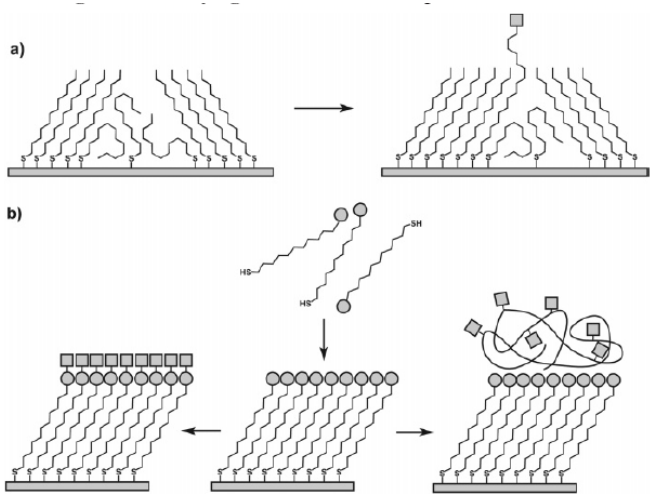

[c] (a) Insertion of a functional adsorbate at a defect site in a preformed SAM. (b) Transformation of a SAM with exposed functional groups (circles) by either chemical reaction or adsorption of another material.

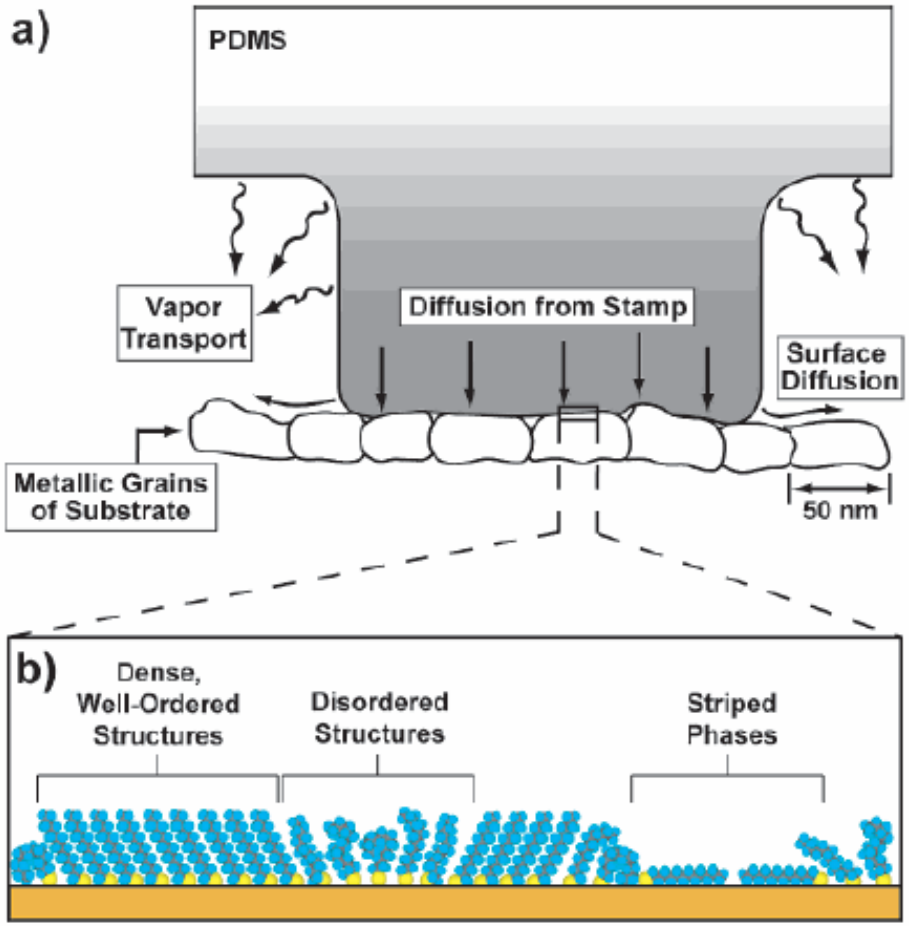

Figure 12. (a) Schematic illustration depicting the application of a PDMS stamp containing thiols to a polycrystalline metal film. The primary mechanisms of mass transport from the stamp to the surface are shown. The grayscale gradient approximates the concentration of thiols adsorbed in the stamp itself. (b) Magnified schematic view that illustrates the variety of structural arrangements found in SAMs prepared by μCP when the stamp is wetted with a 1−10 mM solution and applied to the substrate for 1−10 s.

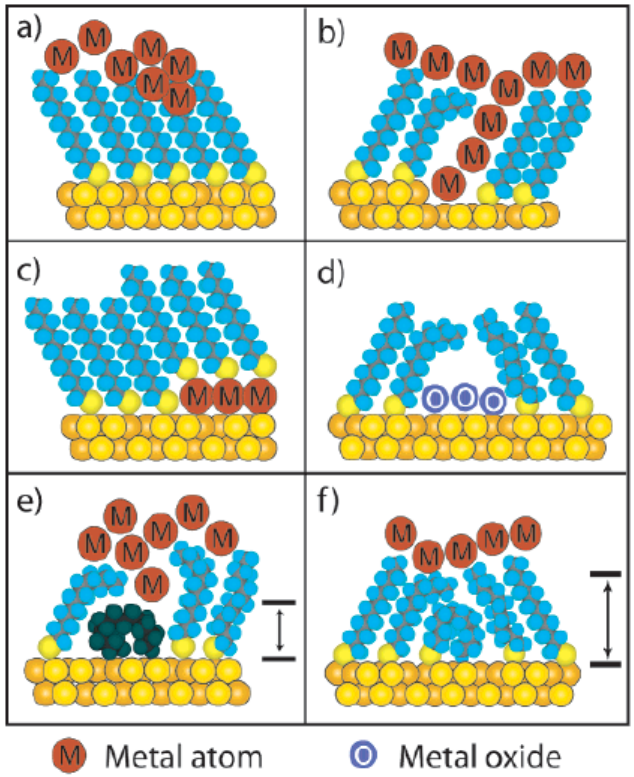

Figure 17. Schematic illustration of the types of defects in SAMs that can influence the rate of electron transfer in two-terminal (or three-terminal) devices. (a) Chemical reaction with the organic component of SAMs during evaporation of metal films. (b) Formation of metallic filaments during evaporation or operation of the device. (c) Deposition of adlayers of metal on the surface of the substrate supporting the SAM. (d) Formation of oxide impurities on the surface. (e) Organic (or organometallic) impurities in the SAM. (f) Thin regions in the SAM resulting from conformational and structural defects. In e and f the dimension normal to the surface that is denoted by the black arrows indicates the approximate shortest distance between the two metal surfaces; note that these distances are less than the nominal thickness of the ordered SAM.

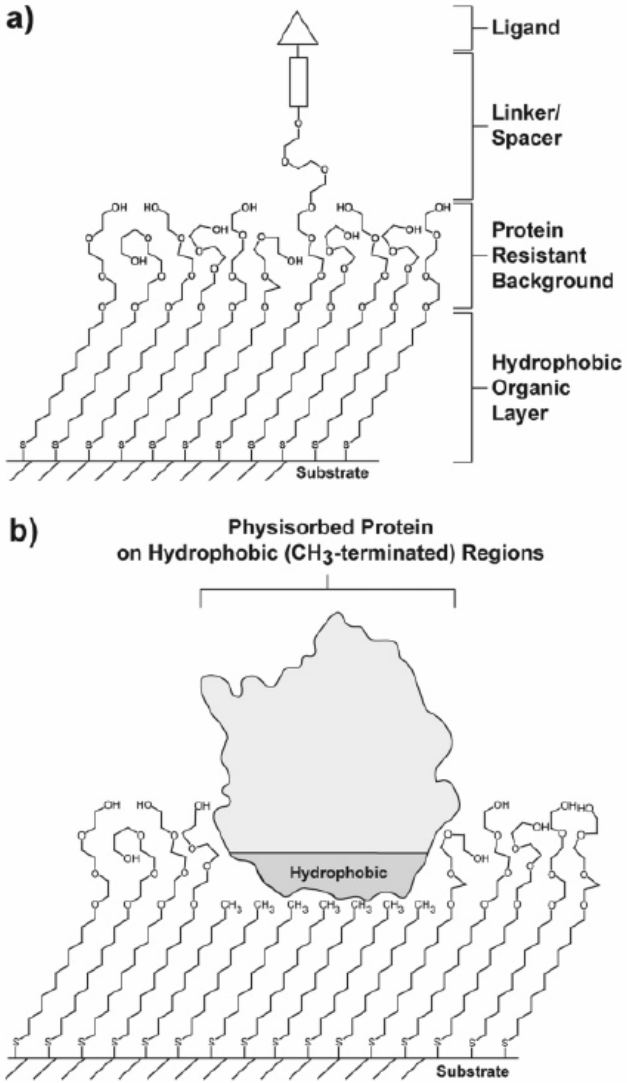

Figure 21. Schematic illustrations of (a) a mixed SAM and (b) a patterned SAM. Both types are used for applications in biology and biochemistry.

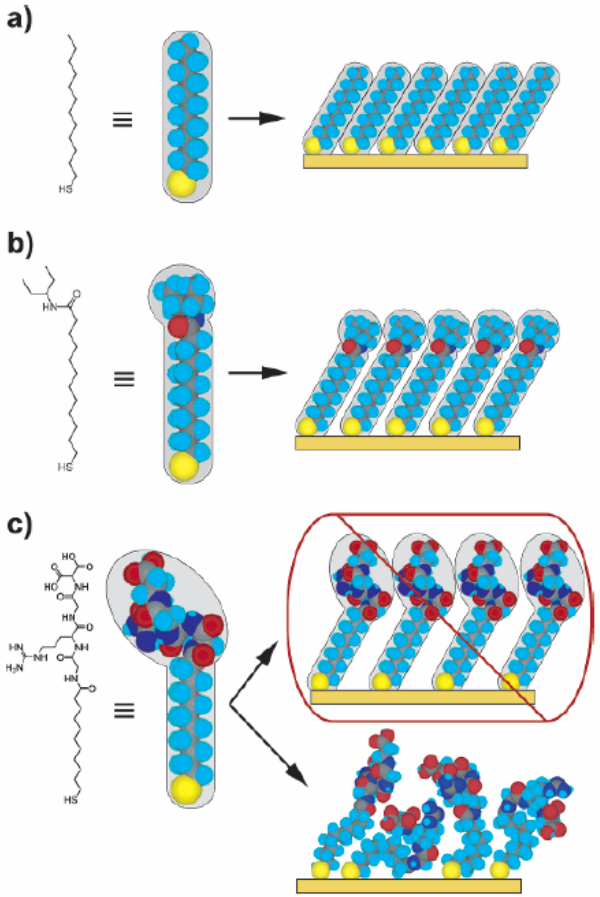

Figure 22. Schematic diagram illustrating the effects that large terminal groups have on the packing density and organization of SAMs. (a) Small terminal groups such as $-CH_3$, $-CN$, etc., do not distort the secondary organization of the organic layer and have no effect on the sulfur arrangement. (b) Slightly larger groups (like the branched amide shown here) begin to distort the organization of the organic layer, but the strongly favorable energetics of metal−sulfur binding drive a highly dense arrangement of adsorbates. (c) Large terminal groups (peptides, proteins, antibodies) sterically are unable to adopt a secondary organization similar to that for alkanethiols with small terminal groups. The resulting structures probably are more disordered and less dense than those formed with the types of molecules in a and b.

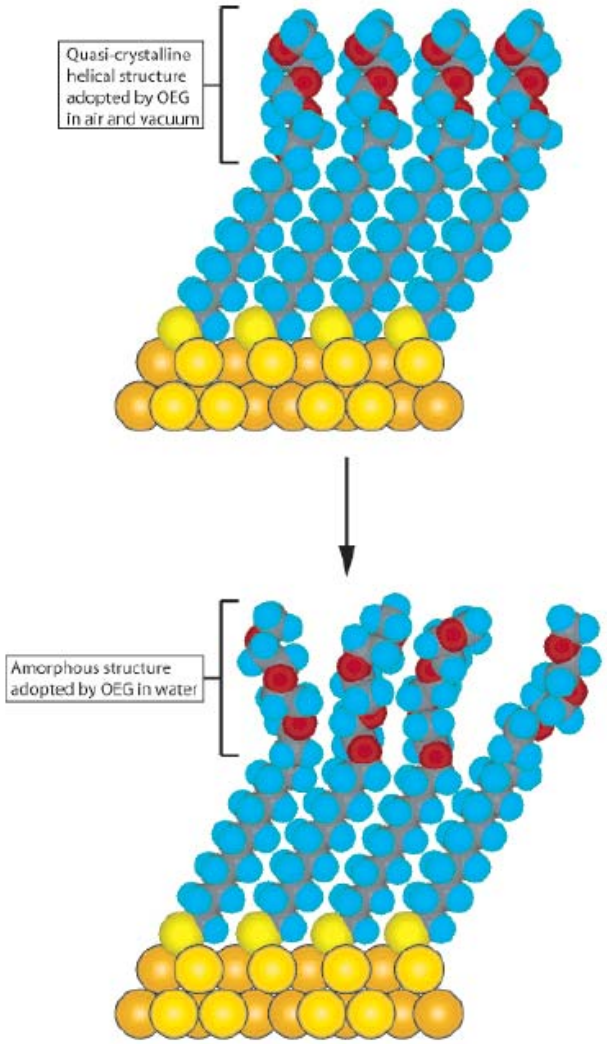

Figure 23. Schematic illustration of the order−disorder transition evidenced by SAMs of alkanethiolates terminated with triethylene glycol. The EG_3 group loses conformational ordering upon solvation in water.

Control of crystal nucleation by patterned self-assembled monolayers

NATURE | VOL 398 | 8 APRIL 1999

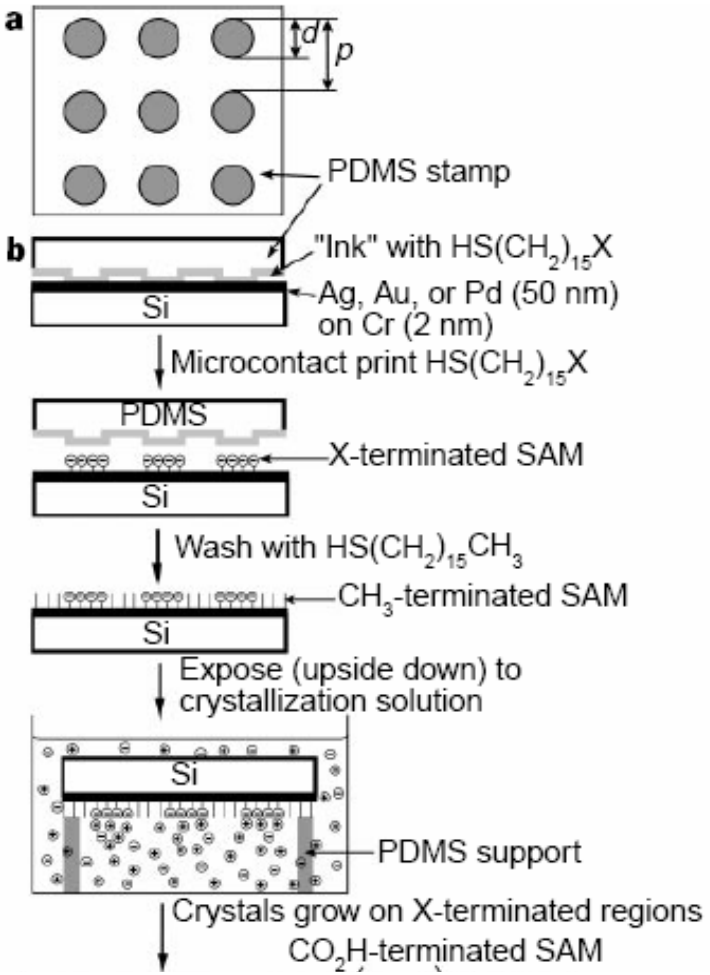

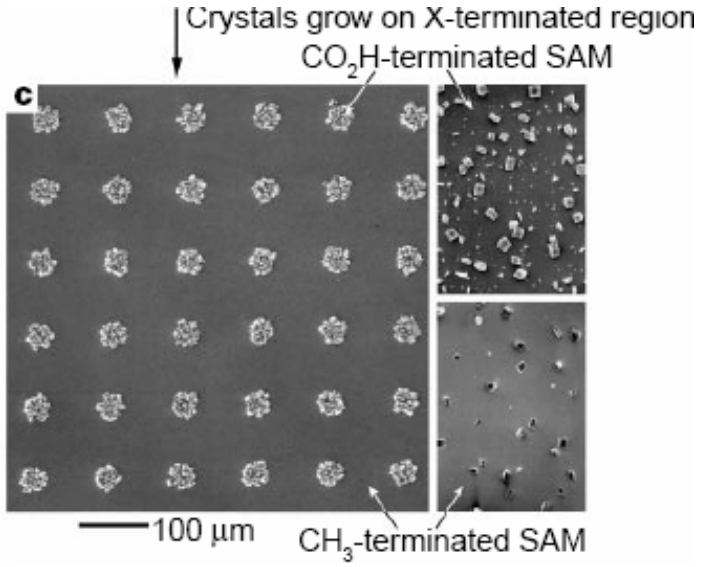

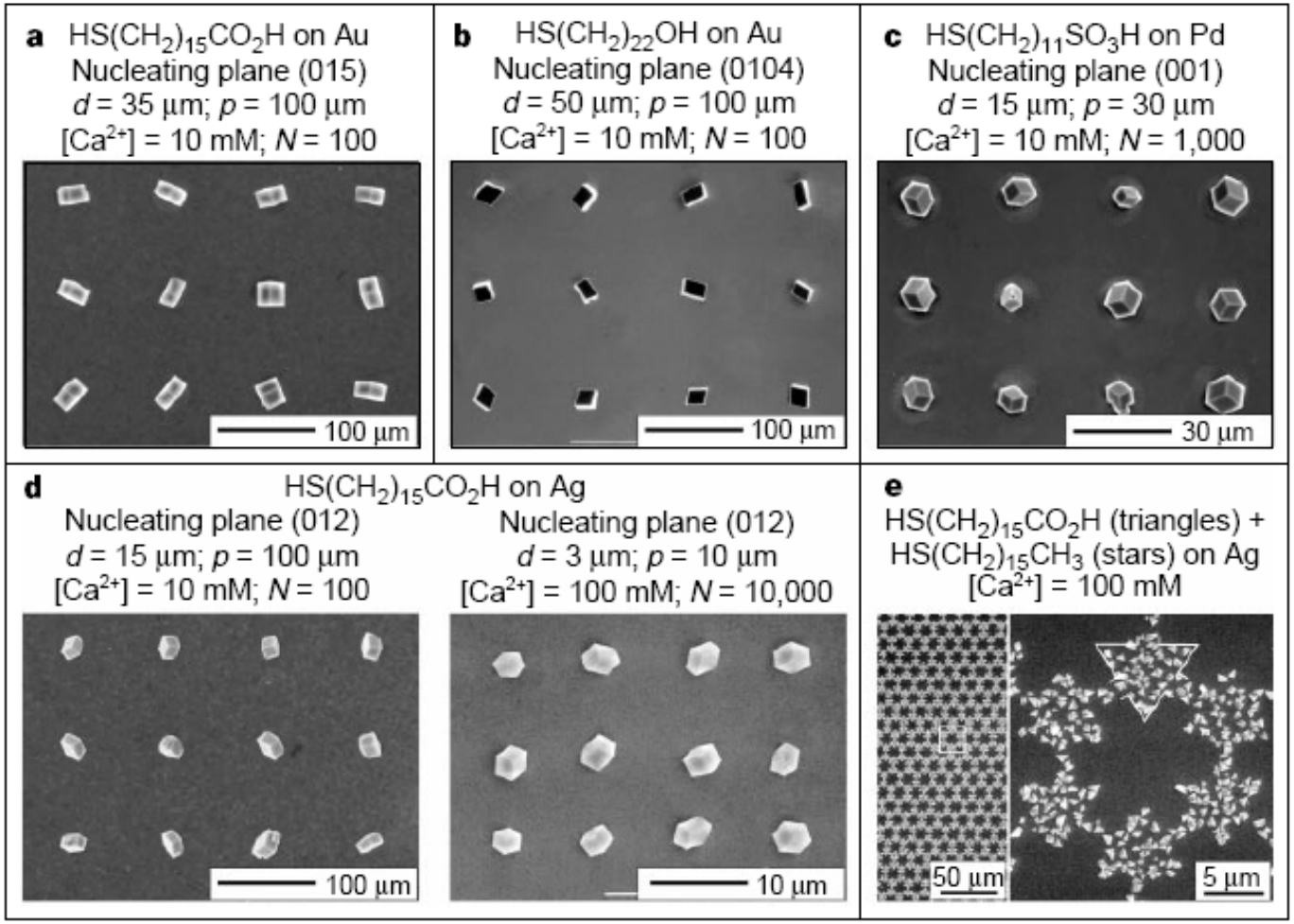
a
HS(CH2)15CO2H on Au
Nucleating plane (015)
d = 35 μm; p = 100 μm
[Ca2+] = 10 mM; N = 100
100 μm
b
HS(CH2)22OH on Au
Nucleating plane (0104)
d = 50 μm; p = 100 μm
[Ca2+] = 10 mM; N = 100
100 μm
c
HS(CH2)11SO3H on Pd
Nucleating plane (001)
d = 15 μm; p = 30 μm
[Ca2+] = 10 mM; N = 1,000
30 μm
d
HS(CH2)15CO2H on Ag
Nucleating plane (012)
d = 15 μm; p = 100 μm
[Ca2+] = 10 mM; N = 100
100 μm
Nucleating plane (012)
d = 3 μm; p = 10 μm
[Ca2+] = 100 mM; N = 10,000
10 μm
e
HS(CH2)15CO2H (triangles) +
HS(CH2)15CH3 (stars) on Ag
[Ca2+] = 100 mM
50 μm
5 μm

Patterning of organic single crystals

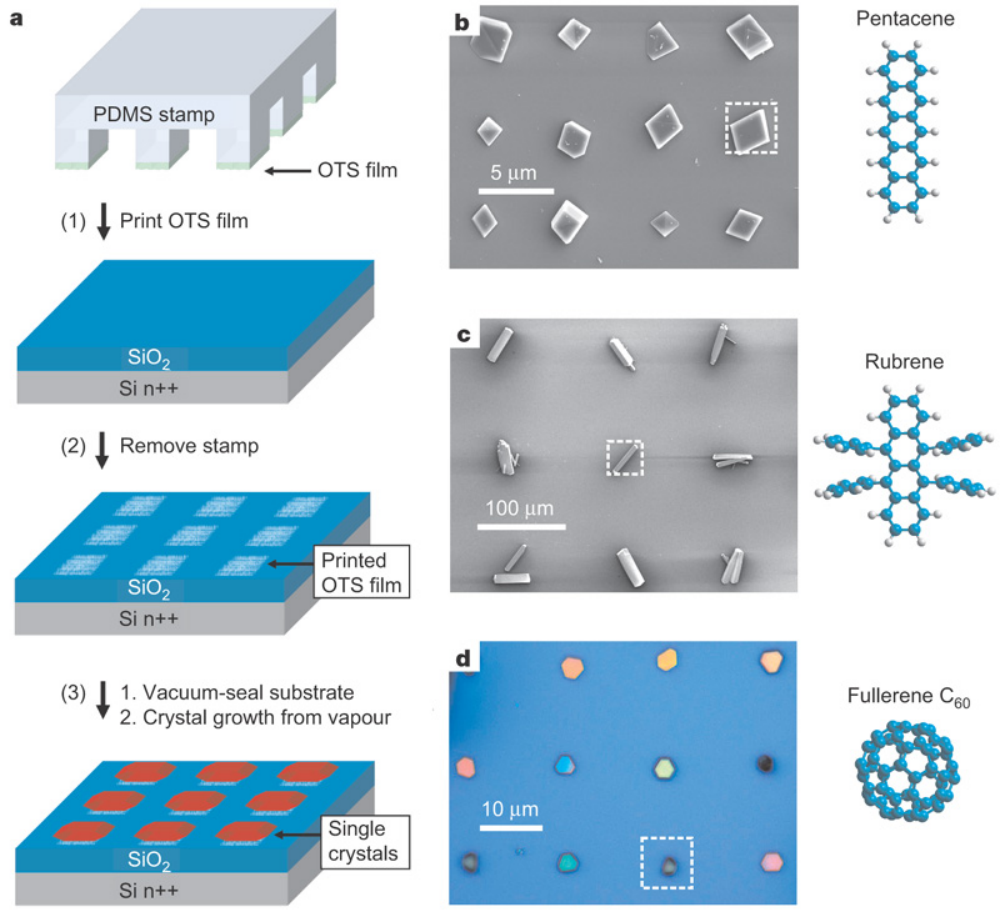

Nature 444, 913-917(14 December 2006)

Large On-Off Ratios and Negative Differential Resistance in a Molecular Electronic Device

J. Chen,[1] M. A. Reed,[1]* A. M. Rawlett,[2] J. M. Tour[2]*

19 NOVEMBER 1999 VOL 286 SCIENCE

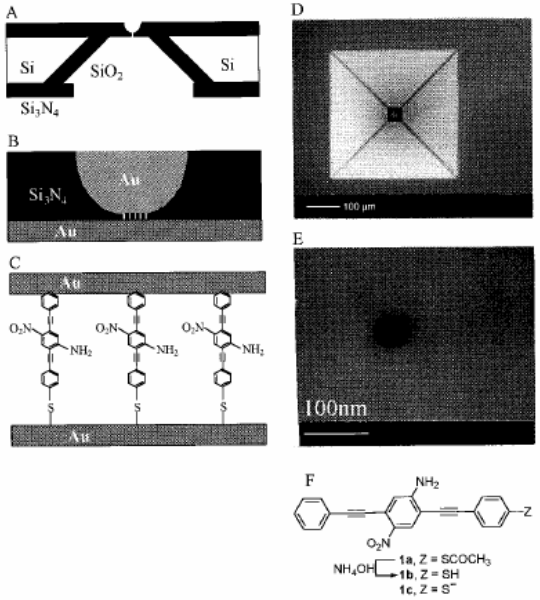

Fig. 1. Schematics of device fabrication. **(A)** Cross section of a silicon wafer with a nanopore etched through a suspended silicon nitride membrane. **(B)** Au-SAM-Au junction in the pore area. **(C)** Blowup of (B) with **1c** sandwiched in the junction. **(D)** Scanning electron micrograph (SEM) of pyramid Si structure after unisotropic Si etching [that is, the bottom view of (A)]. **(E)** SEM of an etched nanopore through the silicon nitride membrane. **(F)** The active molecular compound **1c** and its precursors the free thiol **1b** and the thiol-protected system **1a**.

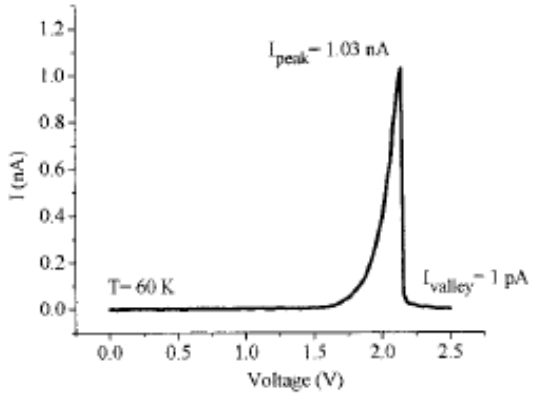

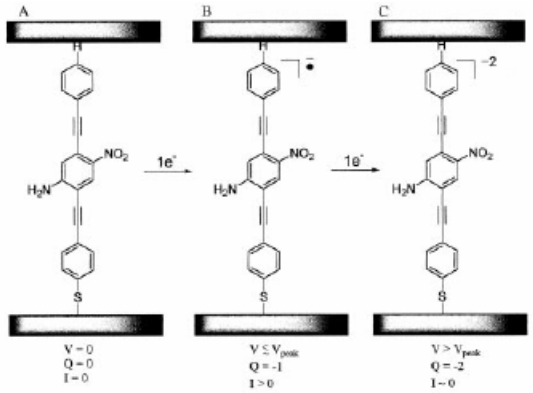

Fig. 4. Potential mechanism for the NDR effect. As voltage is applied, the molecules in the SAM **(A)** undergo a one-electron reduction to form the radical anion **(B)** that provides a conductive state. Further increase of the voltage causes another one-electron reduction to form the dianion insulating state **(C)**. Q is the charge.

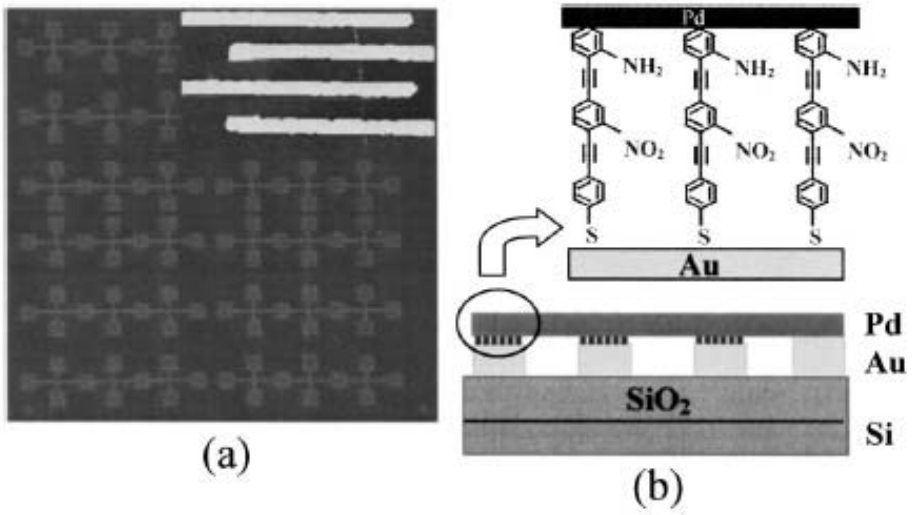

FIG. 1. (a) Optical micrograph of the nanoelectrode array. Inset: AFM image of four Au nanoelectrodes with a Pd nanowire lying across. (b) Schematic diagram of the Pd/molecular wires/Au junctions on a Si/SiO_2 substrate.

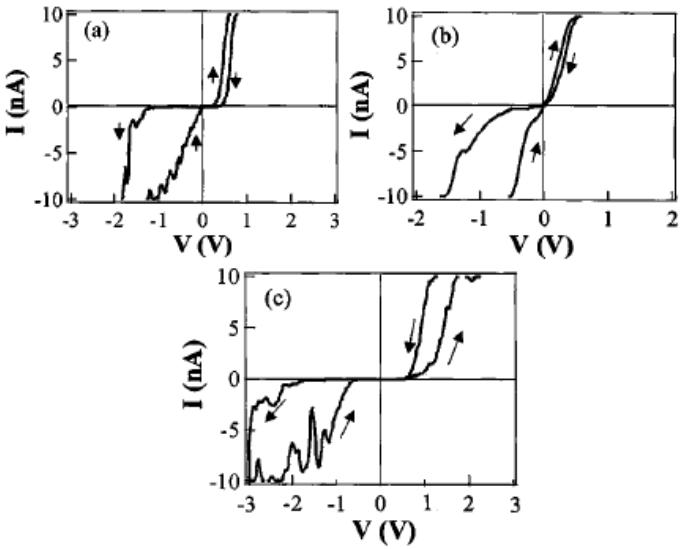

FIG. 3. Typical $I-V$ curves of molecular devices. (a), (b), and (c) correspond to molecules **a**, **b**, and **c** shown in Fig. 2, respectively.

Geometric Control of Cell Life and Death

SCIENCE • VOL. 276 • 30 MAY 1997

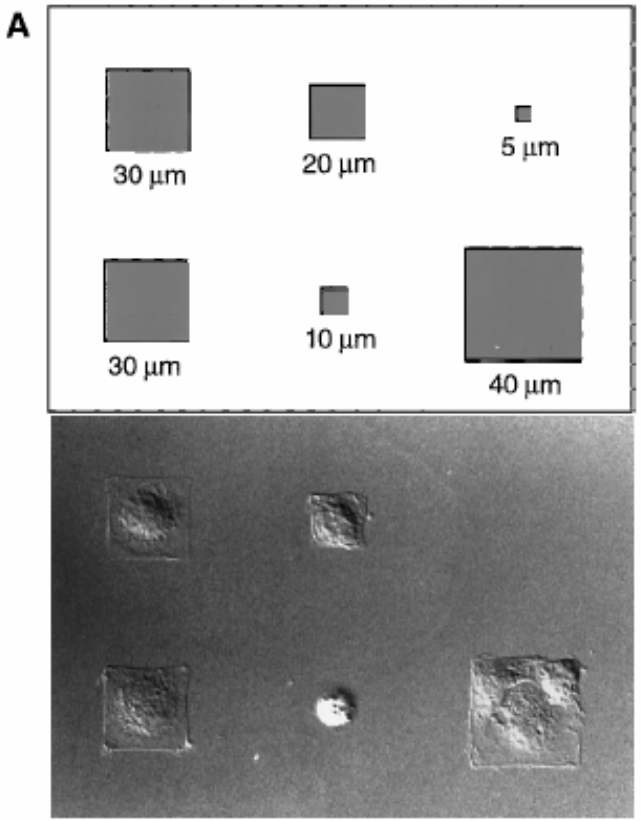

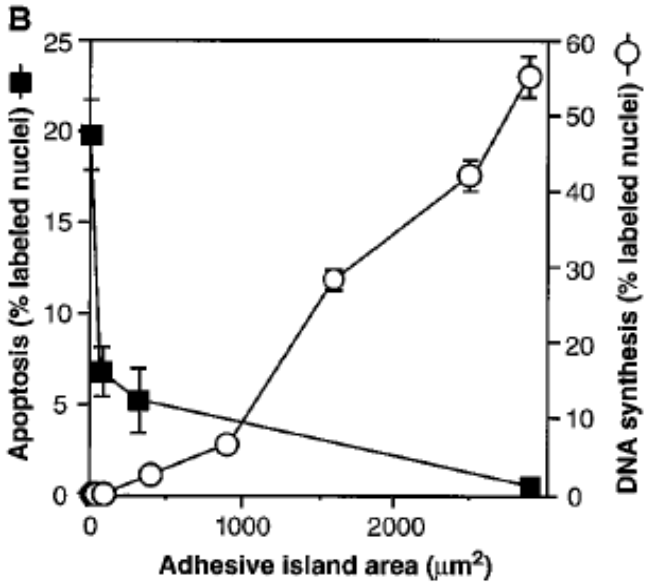

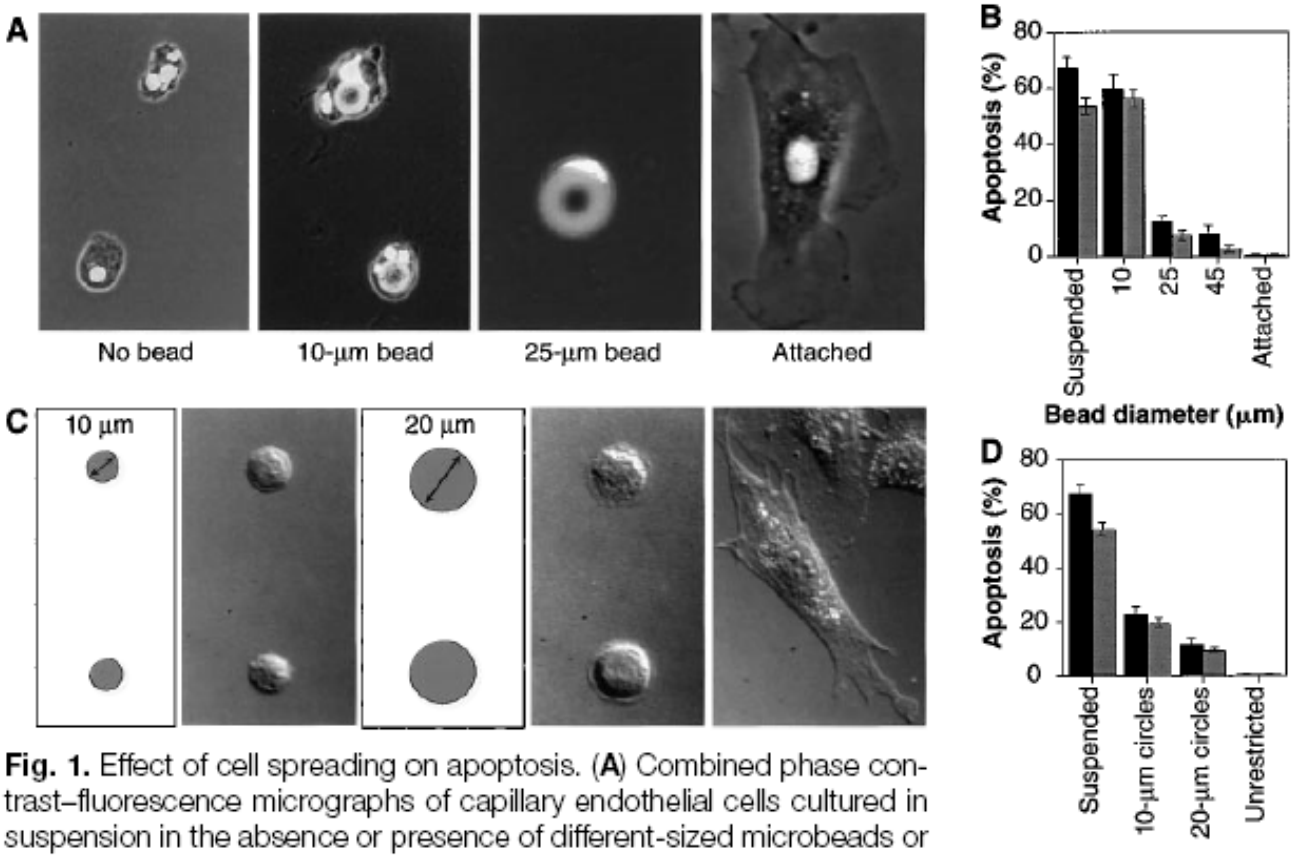

Fig. 1. Effect of cell spreading on apoptosis. (**A**) Combined phase contrast–fluorescence micrographs of capillary endothelial cells cultured in suspension in the absence or presence of different-sized microbeads or attached to a planar culture dish coated with FN for 24 hours (*28*). In the highly spread cell on the 25-μm bead, only the flattened 4′,6′-diamidino-2-phenylindole (DAPI)–stained nucleus is clearly visible. (**B**) Apoptosis in cells attached to different-sized beads, in suspension, or attached to a dish. The apoptotic index was quantitated by measuring the percentage of cells exhibiting positive TUNEL staining (black bars) (Boehringer Mannheim), which detects DNA fragmentation; similar results were obtained by analyzing changes in nuclear condensation and fragmentation in cells stained with DAPI at 24 hours (gray bars). Apoptotic indices were determined only within single cells bound to single beads. Error bars indicate SEM. (**C**) Differential interference-contrast micrographs of cells plated on substrates micropatterned with 10- or 20-μm-diameter circles coated with FN (left), by a microcontact printing method (*29*) or on a similarly coated unpatterned substrate (right). (**D**) Apoptotic index of cells attached to different-sized adhesive islands coated with a constant density of FN for 24 hours; similar results were obtained with human and bovine capillary endothelial cells (*28*). Bars same as in (B).

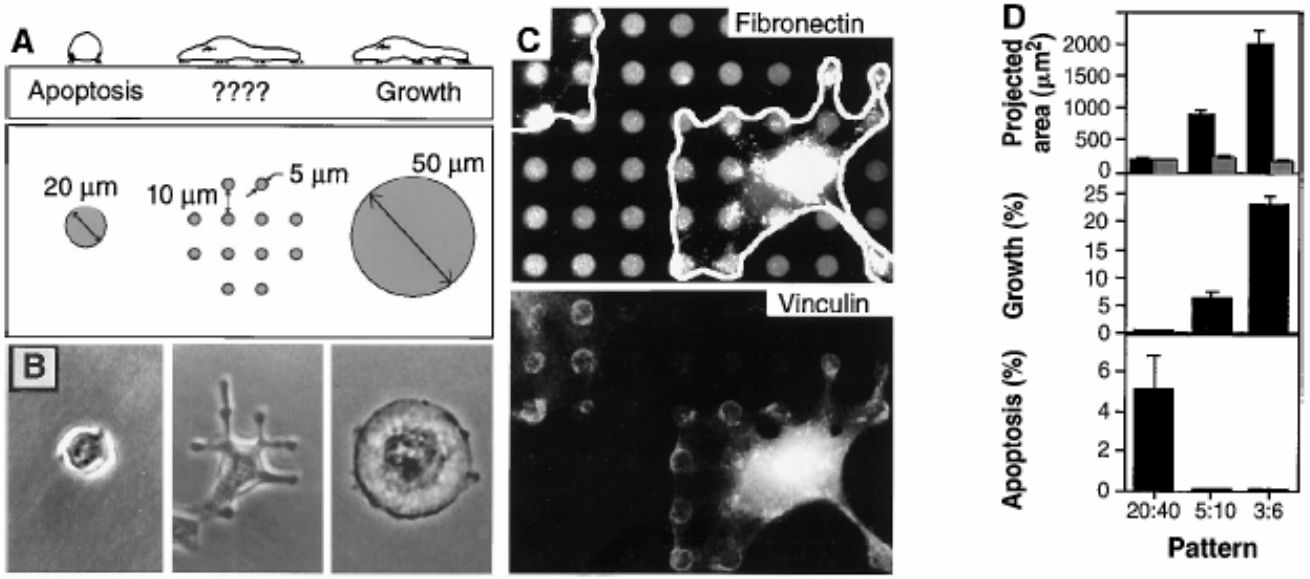

Fig. 3. Cell-ECM contact area versus cell spreading as a regulator of cell fate. (**A**) Diagram of substrates used to vary cell shape independently of the cell-ECM contact area. Substrates were patterned with small, closely spaced circular islands (center) so that cell spreading could be promoted as in cells on larger, single round islands, but the ECM contact area would be low as in cells on the small islands. (**B**) Phase-contrast micrographs of cells spread on single 20- or 50-μm-diameter circles or multiple 5-μm circles patterned as shown in (A). (**C**) Immunofluorescence micrographs of cells on a micropatterned substrate stained for FN (top) and vinculin (bottom). White outline indicates cell borders; note circular rings of vinculin staining, which coincide precisely with edges of the FN-coated adhesive islands. (**D**) Plots of projected cell area (black bars) and total ECM contact area (gray bars) per cell (top), growth index (middle), and apoptotic index (bottom) when cells were cultured on single 20-μm circles or on multiple circles 5 or 3 μm in diameter separated by 40, 10, and 6 μm, respectively.

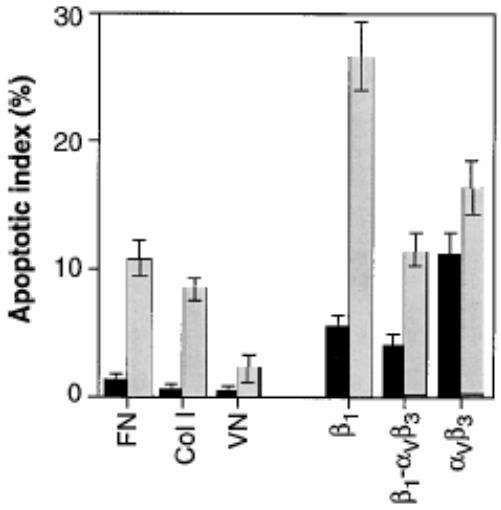

Fig. 4. Role of different integrin ligands in cell shape–regulated apoptosis. Apoptotic indices (percentage positive TUNEL staining) for cells cultured for 24 hours on unpatterned substrates (black bars) or on 20-μm circles (gray bars) coated with FN, type I collagen (Col I), vitronectin (VN), anti-β_1, anti-$\alpha_V\beta_3$, or antibodies to both integrin β_1 and integrin $\alpha_V\beta_3$ (*29*).

hexadecanethiol [$HS(CH_2)_{15}CH_3$] was printed onto gold-coated substrates with a flexible stamp containing a relief of the desired pattern. The substrate was immersed immediately in 2 mM tri(ethylene glycol)-terminated alkanethiol [$HS(CH_2)_{11}(OCH_2CH_2)_3OH$ in ethanol], which coated the remaining bare regions of gold. When these substrates were immersed in a solution of FN, vitronectin, or type I collagen (50 μg/ml in phos-

Electrochemical Desorption of Self-Assembled Monolayers Noninvasively Releases Patterned Cells from Geometrical Confinements

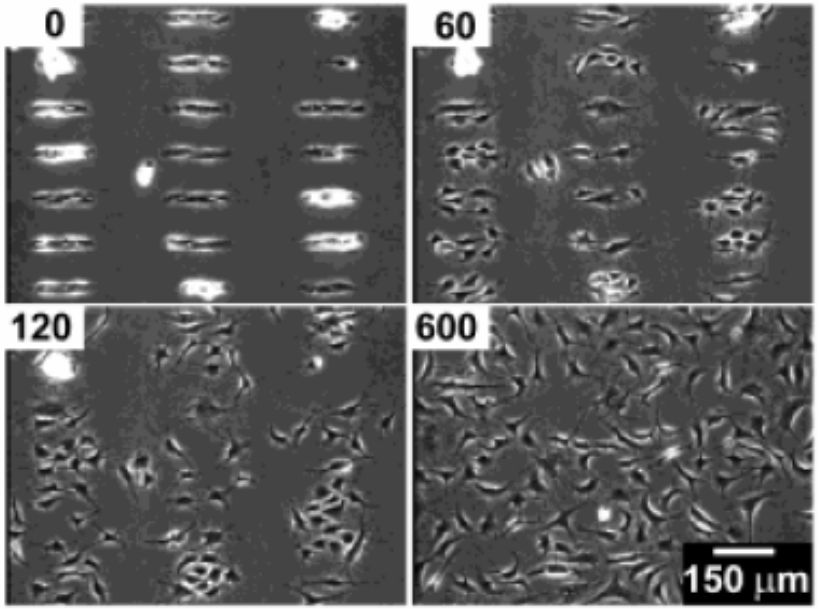

Figure 1. BCE cells were allowed to attach to a surface patterned with $C_{11}EG_3$ and C_{18}. Application of a cathodic voltage pulse (−1.2 V for 30 s in this case) released the cells from the microislands. The numbers indicate the time elapsed (in minutes) after the voltage pulse.

■ **J. AM. CHEM. SOC. 2003**, *125*, 2366−2367

Directing cell migration with asymmetric micropatterns

http://www.pnas.org/cgi/reprint/102/4/9

PNAS | January 25, 2005 | vol. 102 | no. 4 | 975

Xingyu Jiang*, Derek A. Bruzewicz*, Amy P. Wong*, Matthieu Piel†, and George M. Whitesides*‡

*Department of Chemistry and Chemical Biology, Harvard University, 12 Oxford Street, Cambridge, MA 02138; and †Department of Molecular and Cellu Biology, Harvard University, 16 Divinity Avenue, Cambridge, MA 02138

Contributed by George M. Whitesides, December 2, 2004

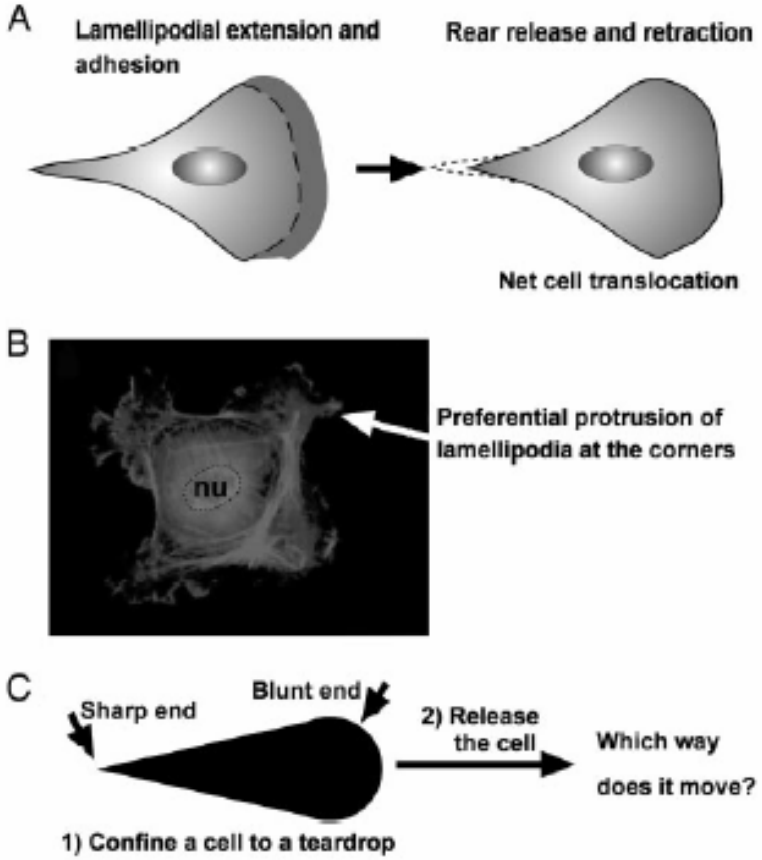

Fig. 1. A problem on cell motility. (*A*) A cartoon illustration of the migration of a typical mammalian cell on a flat surface. This teardrop shape is found in many types of cells. (*B*) Cells confined to squares preferentially extend their lamellipodia from the corners. nu, nucleus. (*C*) If a cell is confined to a shape of teardrop, will the cell preferentially extend its lamellipodia from the sharp end or from the blunt end? If released from confinement, in which direction will it likely move?

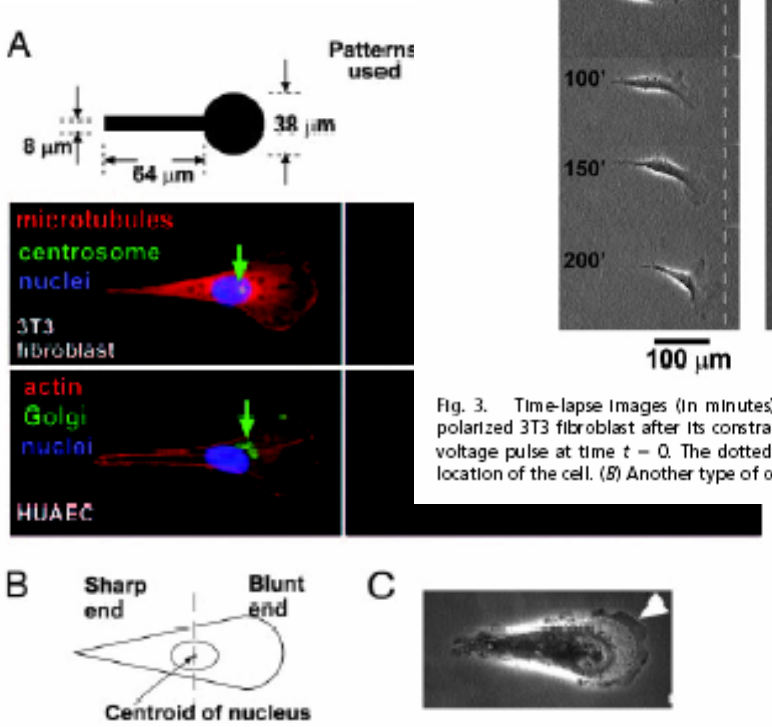

Fig. 2. Asymmetric patterns polarize immobilized cells. (*A*) The Golgi and the centrosome are located closer to the half of a cell with the blunt end. We used phallodin, antigolgin, DAPI, antitubulin, and antipericentrin to identify actin (red), the Golgi (green), the nucleus (blue), microtubules (red), and the centrosome (green), respectively. The green arrows indicate the location of centrosomes in 3T3 cells and Golgi in human umbilical artery endothelial cells (HUAEC). (*B*) We divided the cell into a half with the sharp end and a half with the blunt end by a vertical line drawn at the centroid of the nucleus; >80% ($n = 30$) of the centrosomes and Golgi were localized in the region of the wide end. (*C*) The lamellipodia of immobilized 3T3 cells tended to extend more from the blunt end as well (arrowhead). The dotted line indicates the edges of the adhesive pattern.

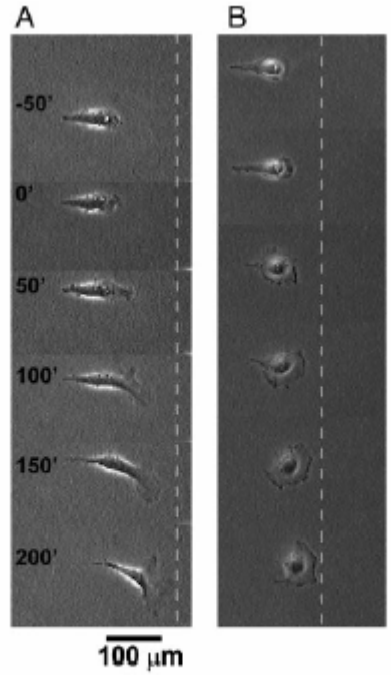

Fig. 3. Time-lapse images (in minutes) show the motility of an initially polarized 3T3 fibroblast after its constraint is released. (*A*) We applied the voltage pulse at time $t = 0$. The dotted line serves as a reference for the location of the cell. (*B*) Another type of cell, COS-7, shows similar behavior.

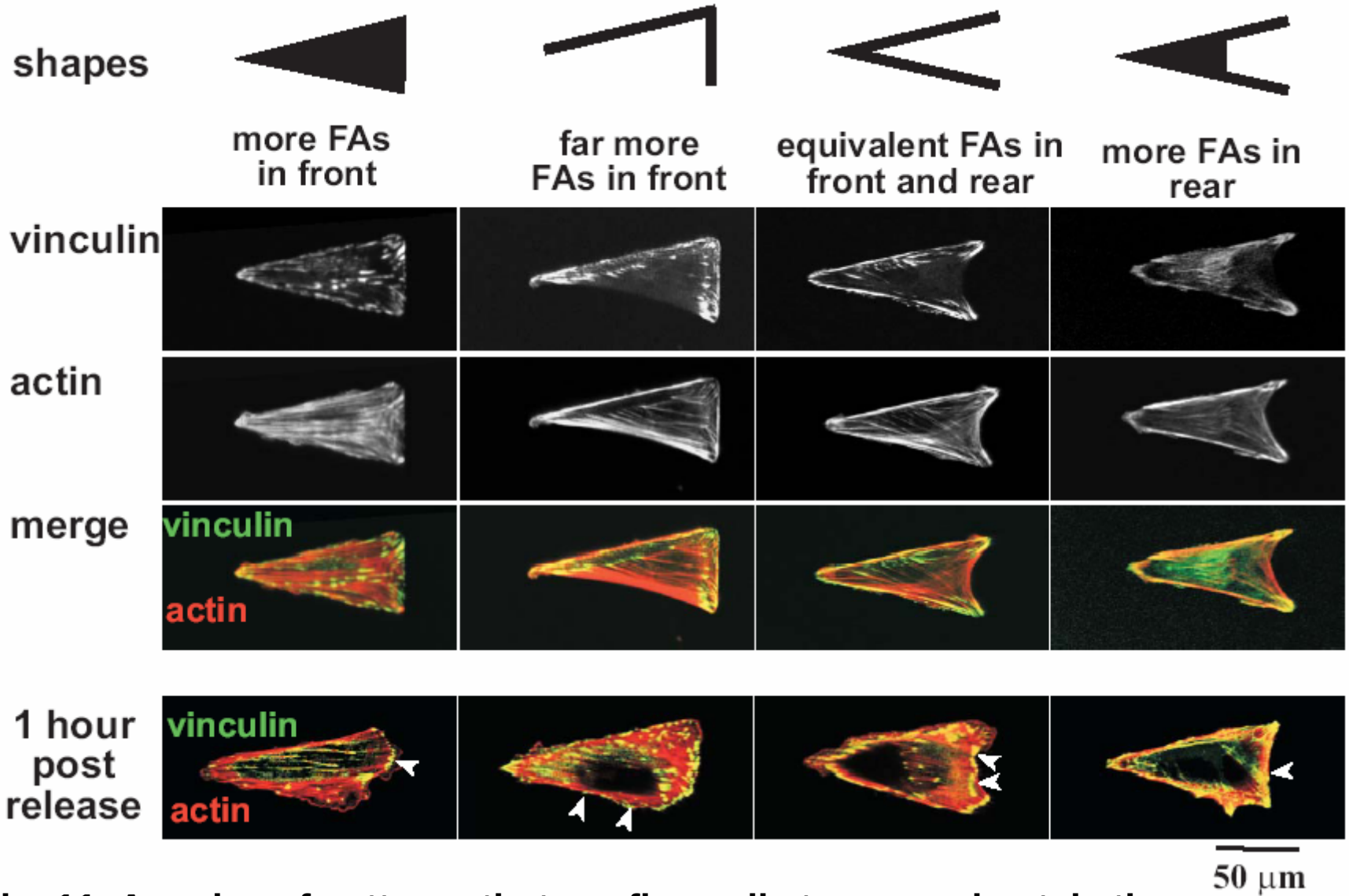

Fig. 11. A series of patterns that confine cells to approximately the same projected geometry (visualized by the actin cytoskeleton) but distribute the focal adhesions (FAs; visualized by immunostaining for vinculin) differently. The bottom row shows that new focal adhesions formed 1 h after release in areas that were inert to attachment of cells prior to release (arrowheads).

Soft-Lithography

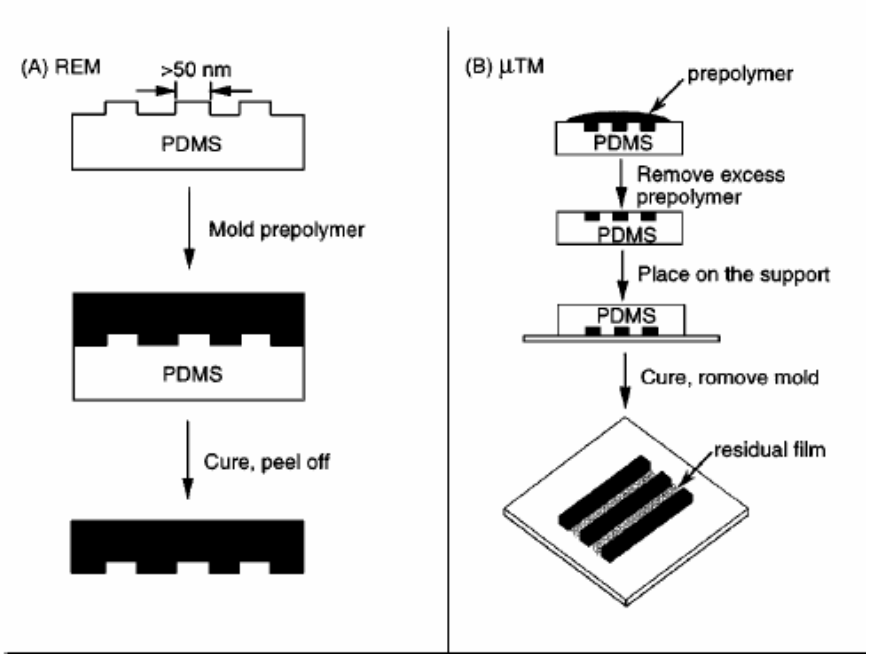

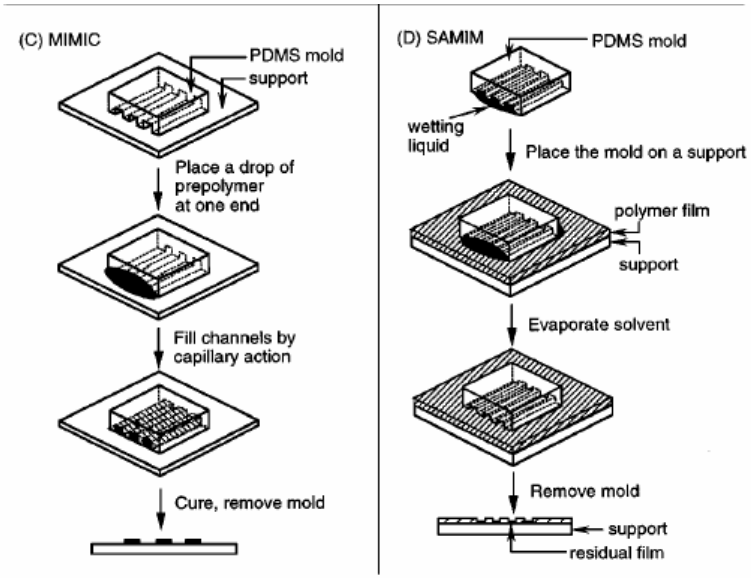

Figure 5 Schematic illustration of procedures for (*a*) replica molding (REM), (*b*) microtransfer molding (μTM), (*c*) micromolding in capillaries (MIMIC), and (*d*) solvent-assisted micromolding (SAMIM).

Electrophoresis 2002, 23, 3461–3473

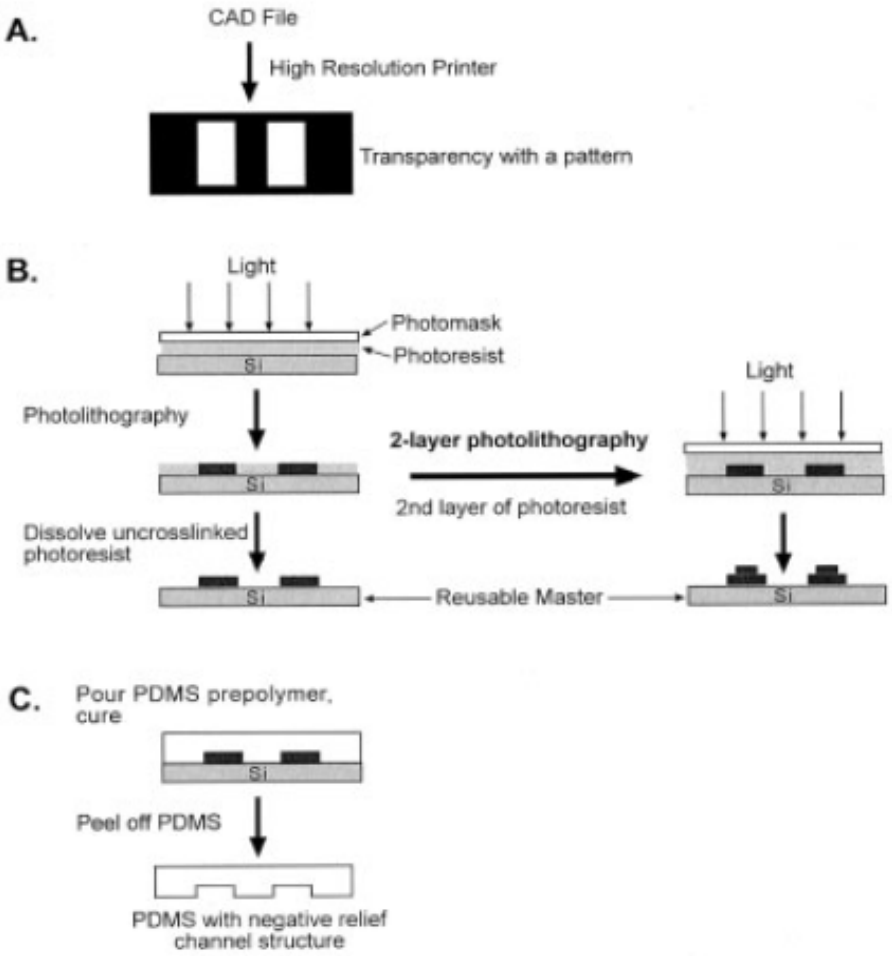

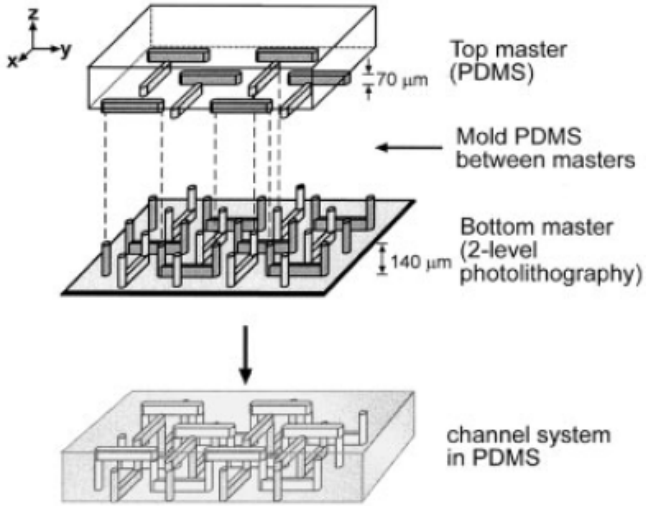

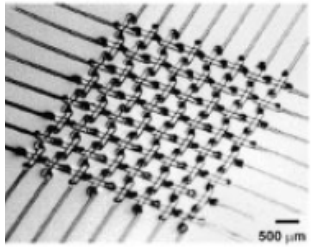

D.

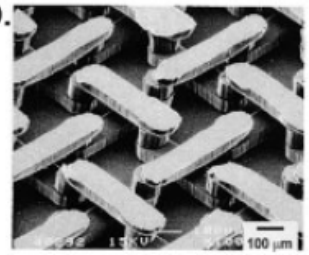

Replication Result

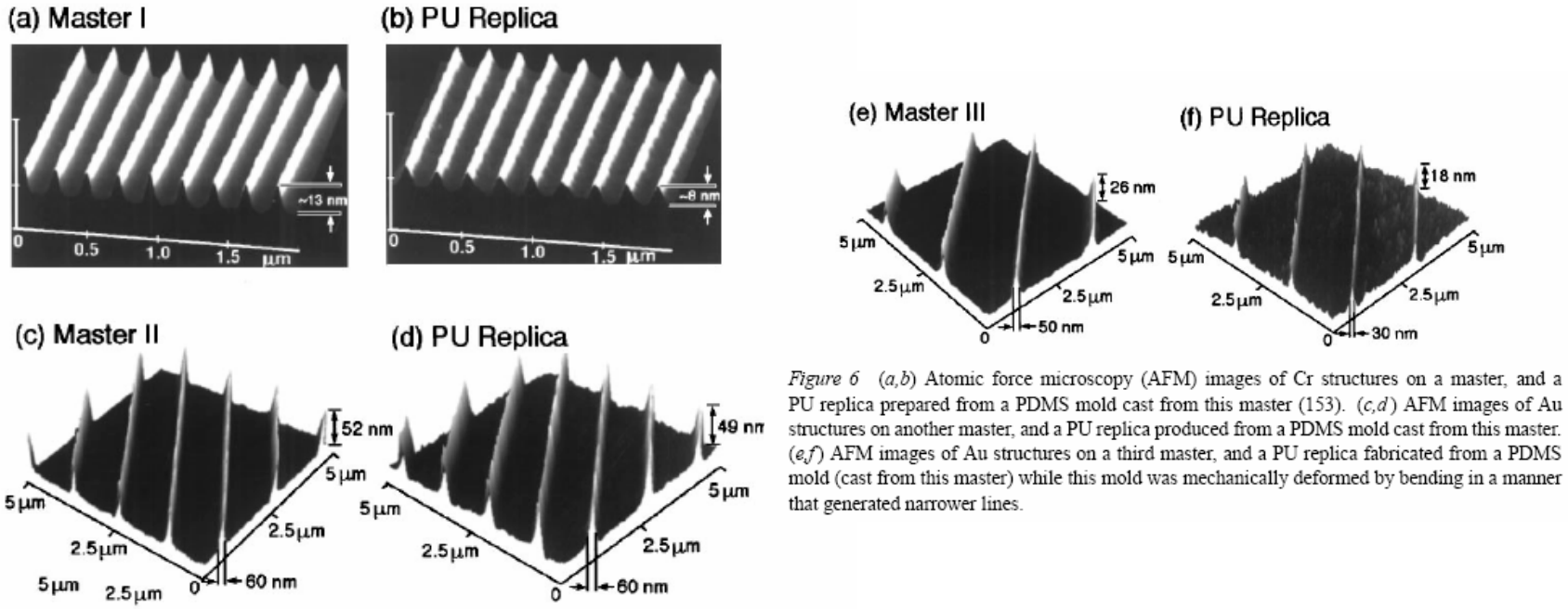

Figure 6 (*a,b*) Atomic force microscopy (AFM) images of Cr structures on a master, and a PU replica prepared from a PDMS mold cast from this master (153). (*c,d*) AFM images of Au structures on another master, and a PU replica produced from a PDMS mold cast from this master. (*e,f*) AFM images of Au structures on a third master, and a PU replica fabricated from a PDMS mold (cast from this master) while this mold was mechanically deformed by bending in a manner that generated narrower lines.

3D Patterning

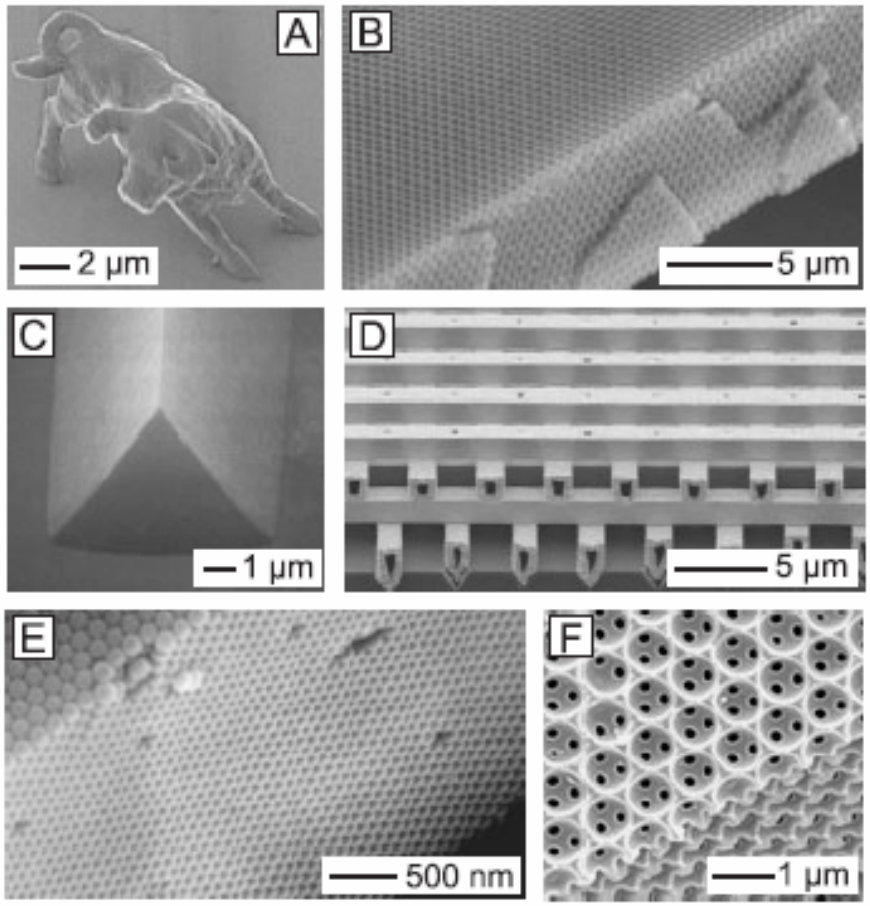

Interference

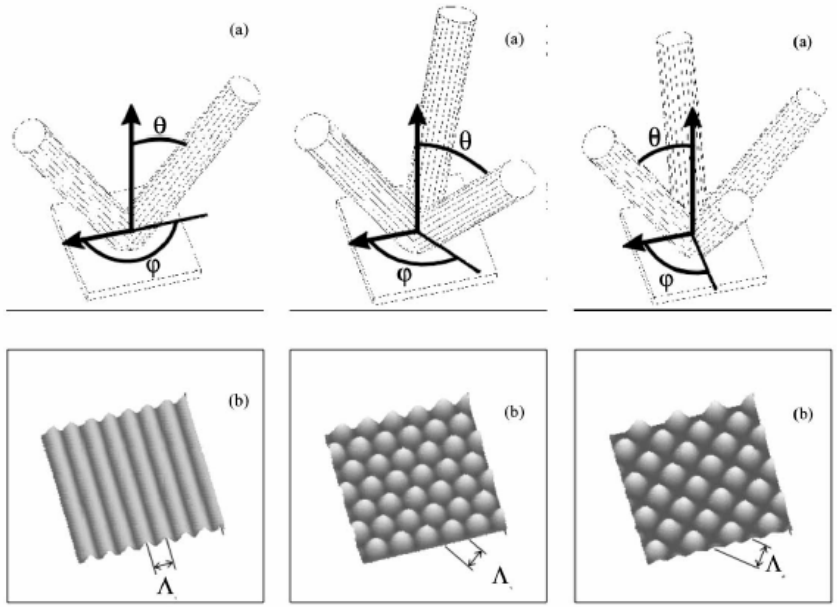

Fig. 1. The orientation of the two (left column), three (middle column) and four (right column) incident beams: (a) and the resulting interference patterns (b).

1. Two beams

$$I_2' = I_1 + I_2 + 2\cos(k(R_2 - R_1))$$

2. Three beams

$$I_3' = I_1 + I_2 + I_3 + 2[\cos(k(R_2 - R_1)) + \cos(k(R_3 - R_1)) + \cos(k(R_3 - R_2))]$$

3. Four beams

$$I_4' = I_1 + I_2 + I_3 + I_4 + 2[\cos(k(R_2 - R_1)) + \cos(k(R_3 - R_1)) + \cos(k(R_3 - R_2)) + \cos(k(R_4 - R_1)) + \cos(k(R_4 - R_2)) + \cos(k(R_4 - R_3))]$$

Interference

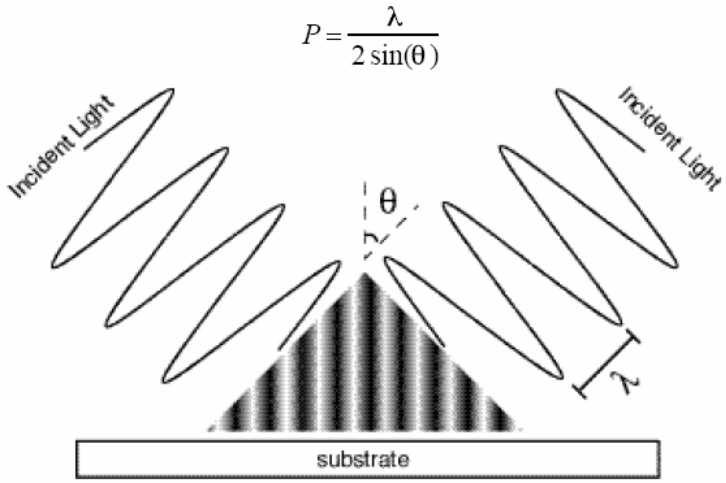

Figure 2.1: *Two-beam interference forms a standing wave.*

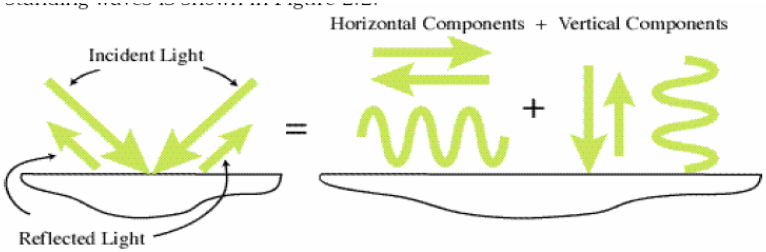

Figure 2.2: *The horizontal and vertical components combine separately to create the desired horizontal standing wave and the undesired vertical standing wave*

Interference Lithography

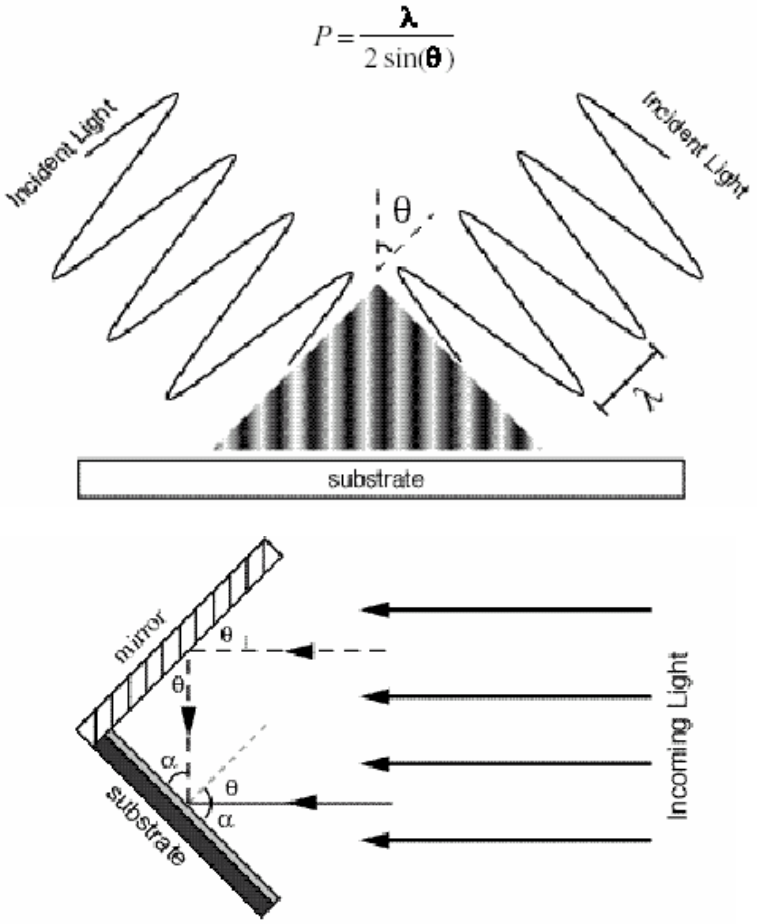

Figure 3.2) Basic Lloyd's mirror configuration

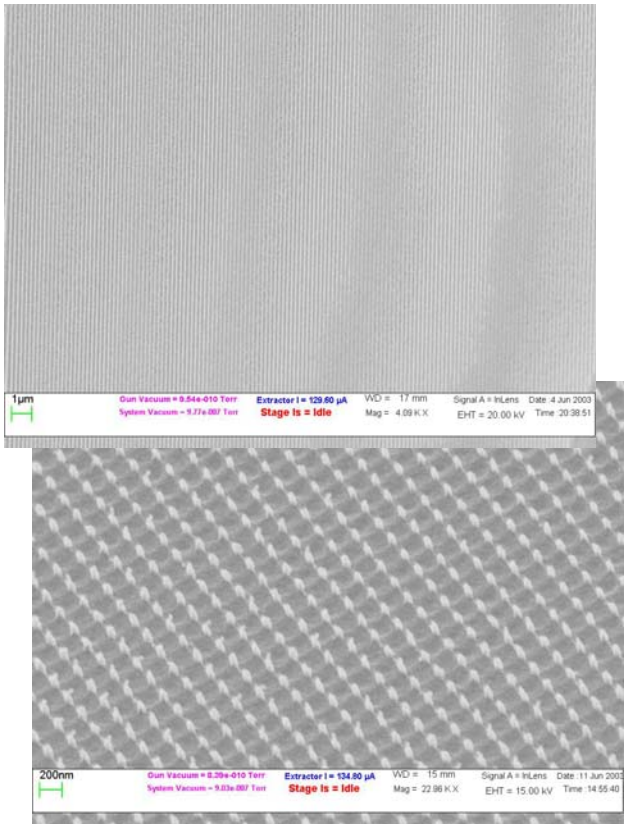

Holographic

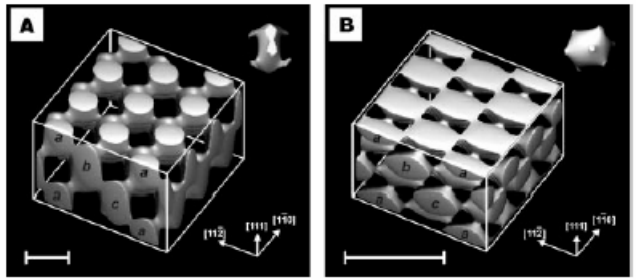

Figure 1 Calculated constant-intensity surfaces in four-beam laser interference patterns designed to produce photonic crystals for the visible spectrum from photoresist. The primitive basis (contents of a Wigner-Seitz unit cell) is shown inset in each case. **A**, f.c.c. pattern with lattice constant 922 nm, used to produce the structures shown in Fig. 3a–d and 4. The close-packed layers of the f.c.c. lattice are indicated on one side of the cube. **B**, f.c.c. pattern with lattice constant 397 nm. Scale bars, 500 nm.

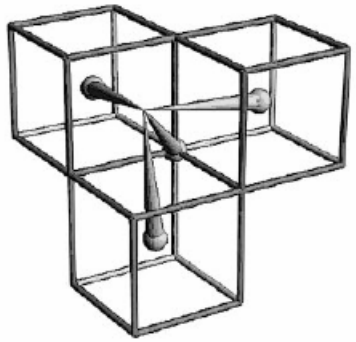

Figure 2 Beam geometry for an f.c.c. interference pattern. The wavevectors of the four laser beams are drawn as cones originating from lattice points in a b.c.c reciprocal lattice. The differences between the central beam wavevector $\mathbf{k}_0$, which originates from the common point of the three cubes shown, and the three wavevectors $\mathbf{k}_{1-3}$ originating from body-centre lattice points, are the primitive set of reciprocal lattice vectors $2\pi/d\langle\bar{1}11\rangle$.

Holographic

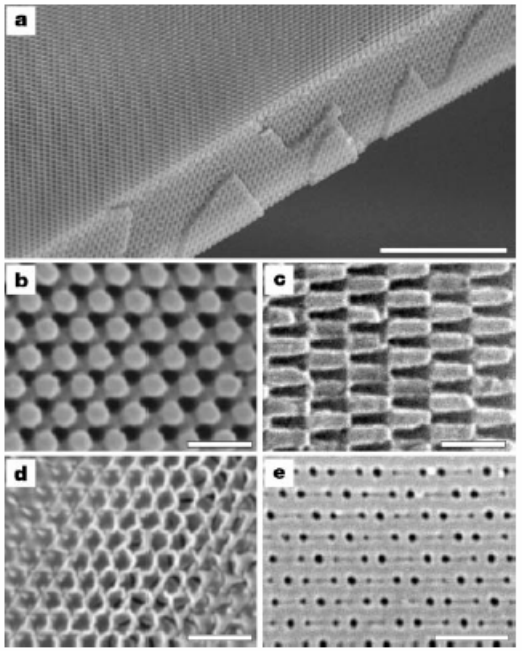

Figure 3 SEM images of photonic crystals generated by holographic lithography. **a**, Polymeric photonic crystal generated by exposure of a 10-μm film of photoresist to the interference pattern shown in Fig. 1A. The top surface is a (111) plane; the film has been fractured along the (11$\bar{1}$) cleavage planes. Scale bar, 10 μm. **b**, Close-up of a (111) surface. Scale bar, 1 μm. **c**, Close-up of a (11$\bar{1}$) surface. Scale bar, 1 μm. **d**, Inverse replica in titania made by using the polymeric structure as a template. The surface is slightly tilted from the (111) plane. Scale bar, 1 μm. **e**, ($\bar{1}$02) surface of a b.c.c. polymeric photonic crystal. Scale bar, 1 μm.

Gold Surface Modification

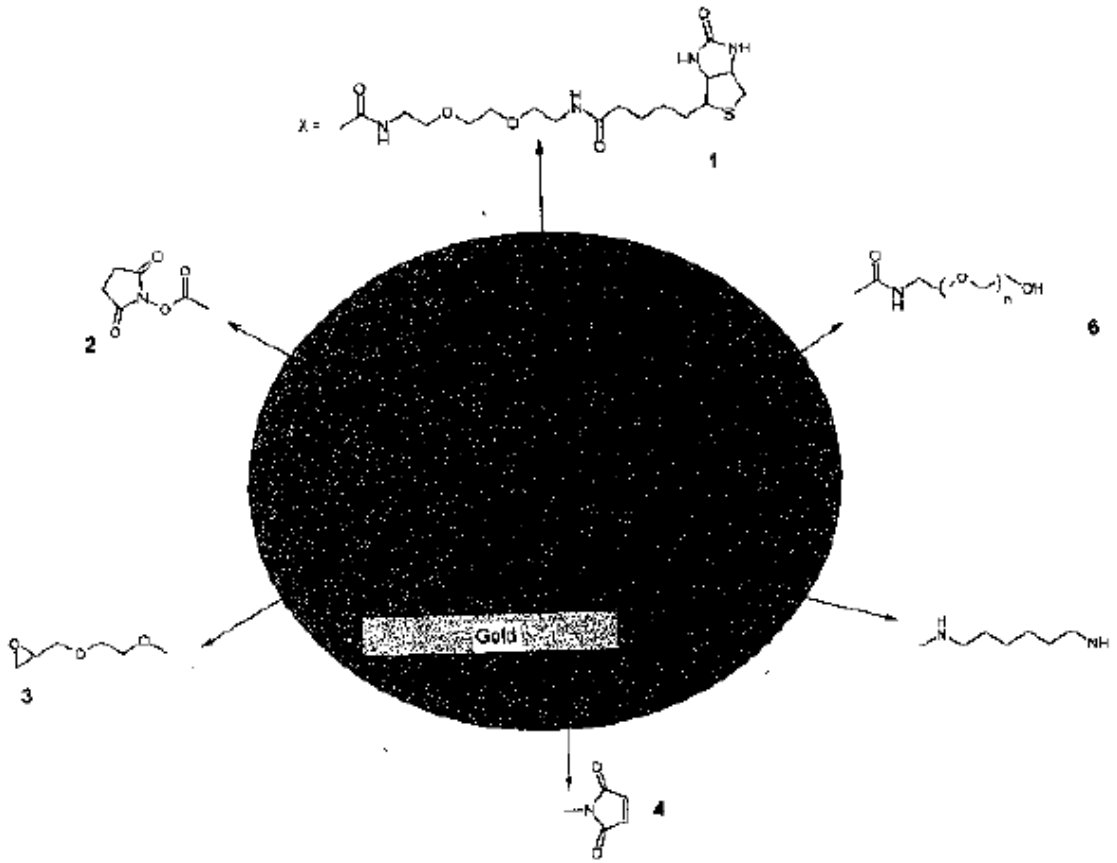

Scheme 2.3 Schematic respresentation of long-chain alkanethiol monolayers (e.g. 16 mercapto-hexadecanoic acid) on gold with different terminal functional groups.

1, biotin; 2, NHS-ester (NHS, N-hydroxysuccin-imide); 3, epoxy-ethylene glycol;
4, maleimide; 5, diaminohexane; 6 oligo (ethylene glycol).

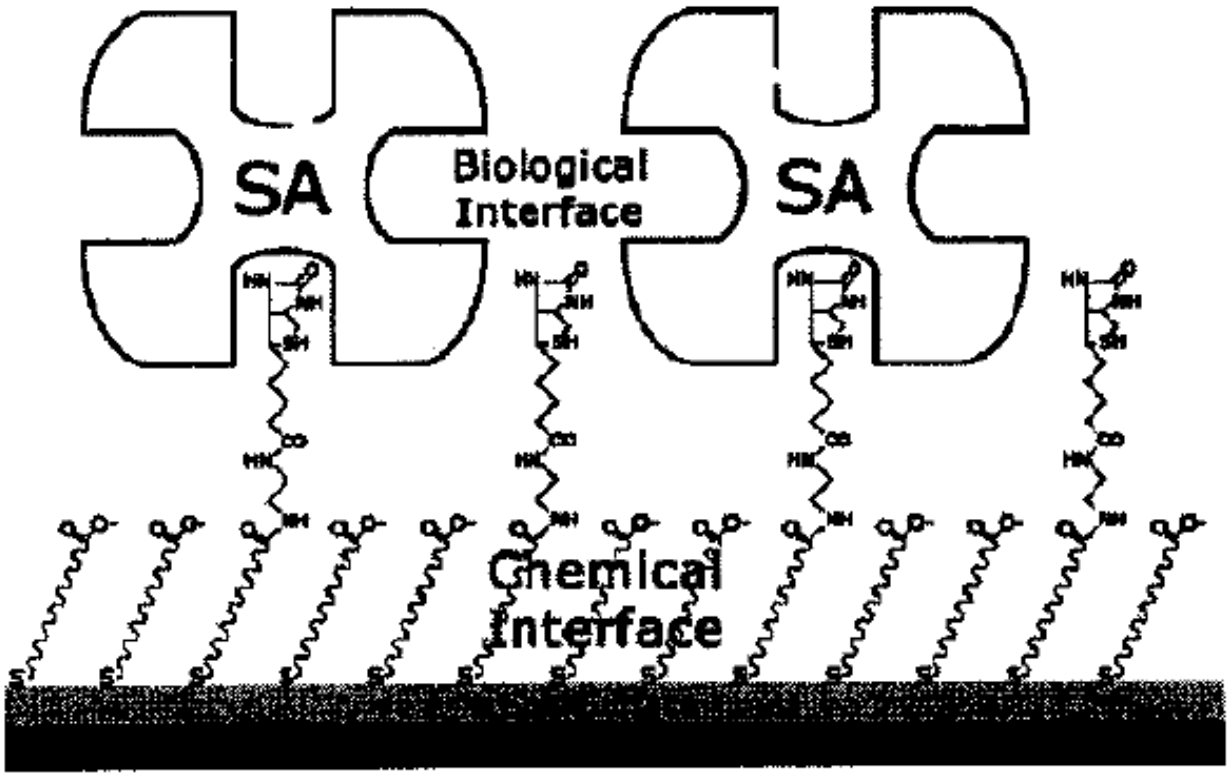

Figure 2.3 Schematic respresentation of a steptavidin sensor surface assembled on a reaction-controlled biotinylated SAM [28].

Biotin

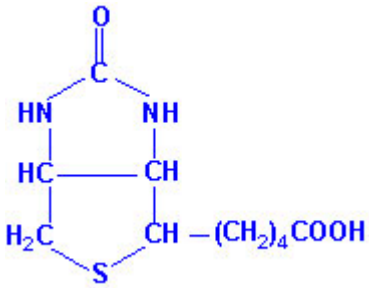

Avidin has a very strong affinity for biotin with a KD (dissociation constant) of approximately 10^{-15} M^{-1}

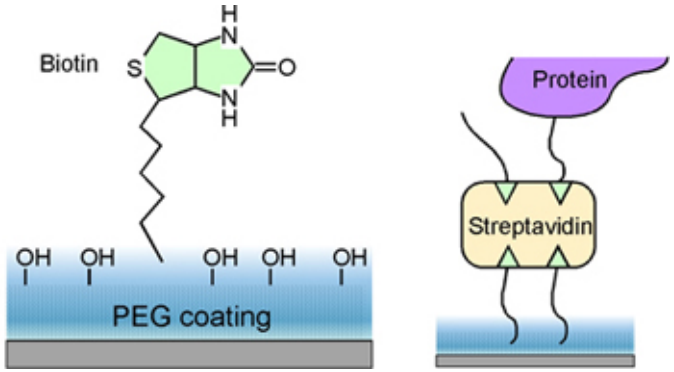

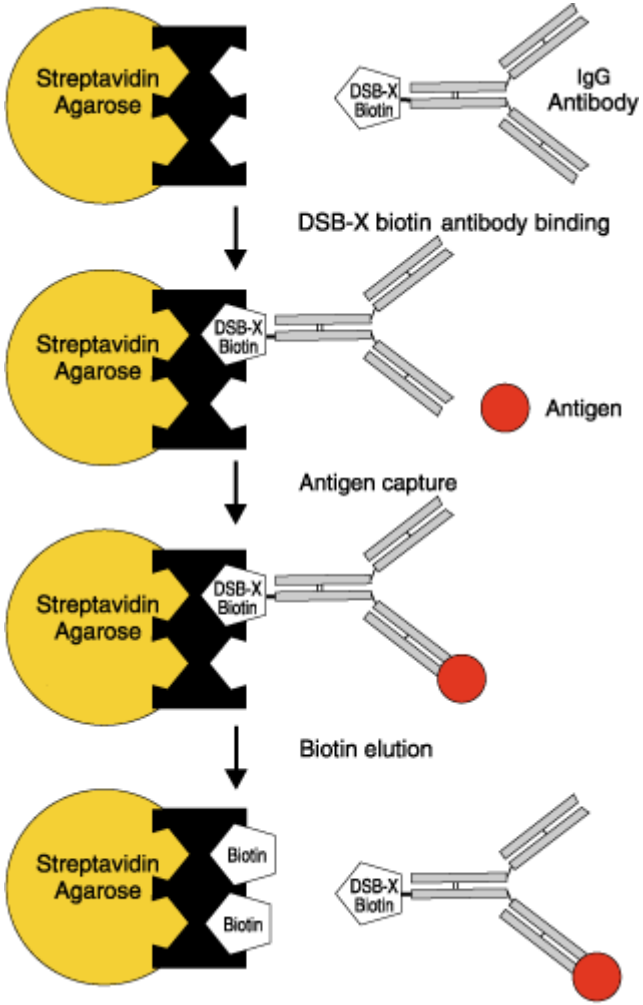
Streptavidin Agarose
DSB-X Biotin
IgG Antibody
DSB-X biotin antibody binding
Antigen
Antigen capture
Biotin elution
Biotin
Biotin

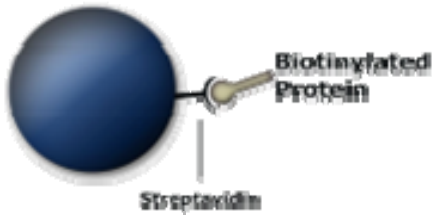
Biotinylated Protein
Streptavidin

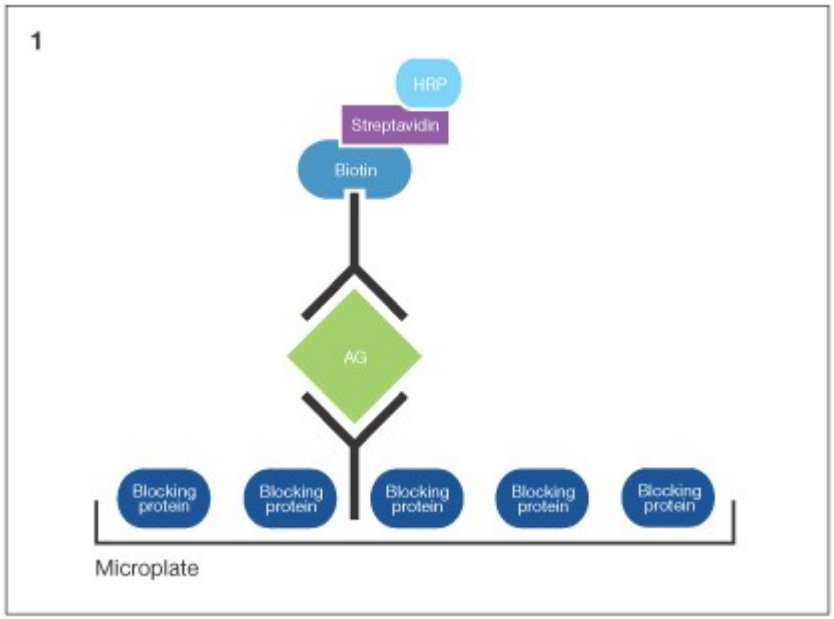
1
HRP
Streptavidin
Biotin
AG
Blocking protein
Blocking protein
Blocking protein
Blocking protein
Blocking protein
Microplate

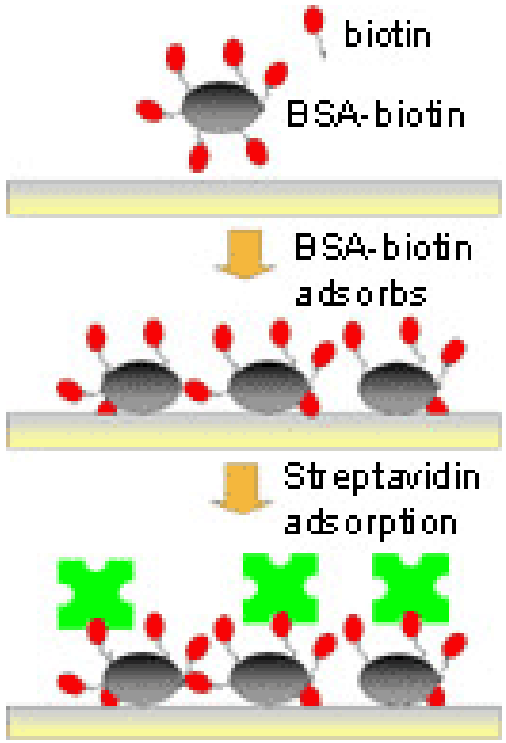
biotin
BSA-biotin
BSA-biotin adsorbs
Streptavidin adsorption

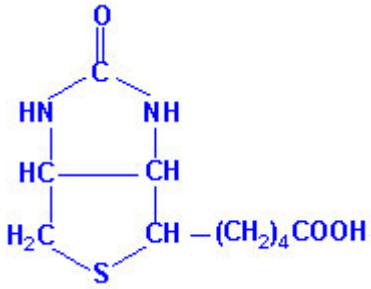

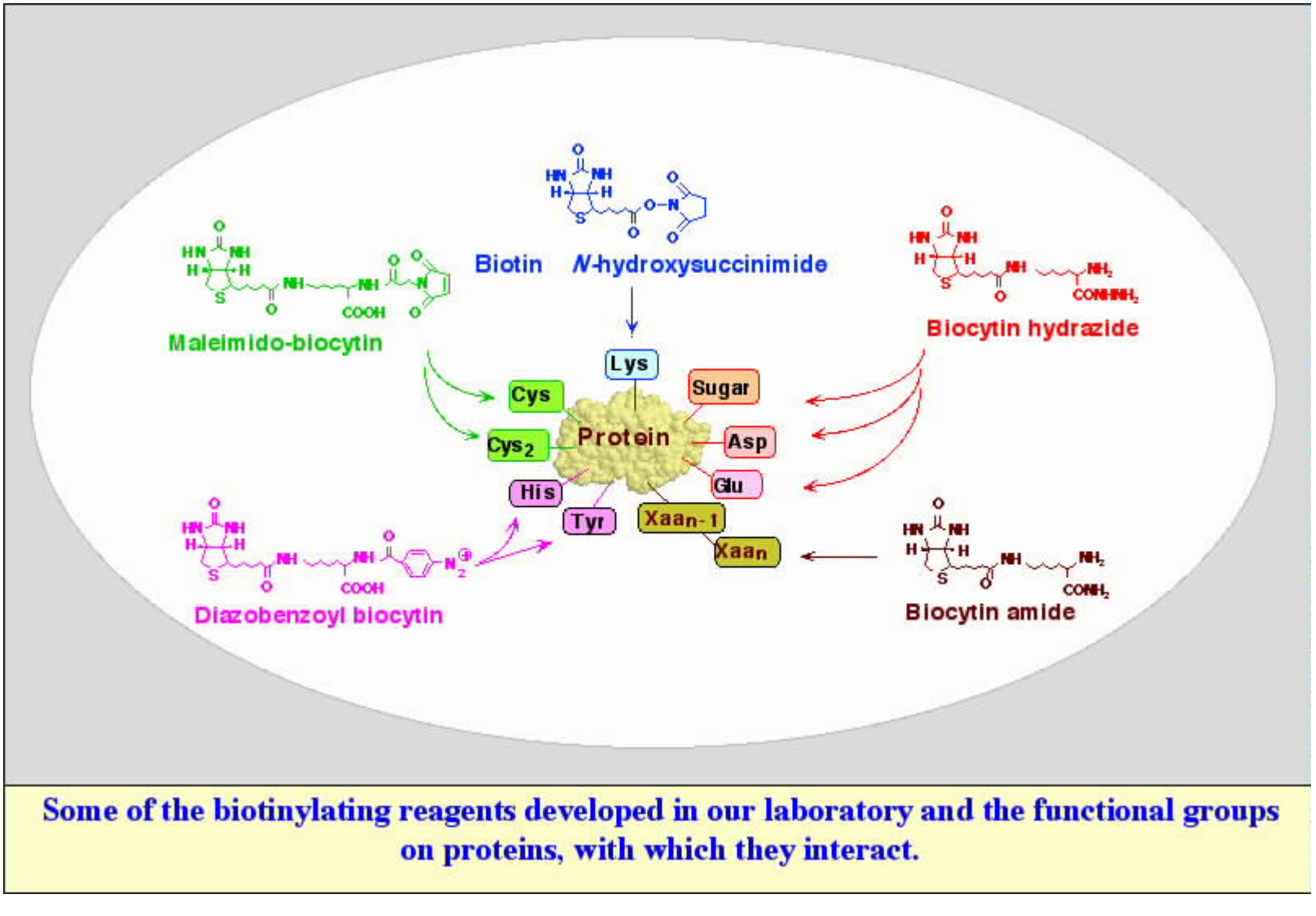

Some of the biotinylating reagents developed in our laboratory and the functional groups on proteins, with which they interact.

Protein Labeling

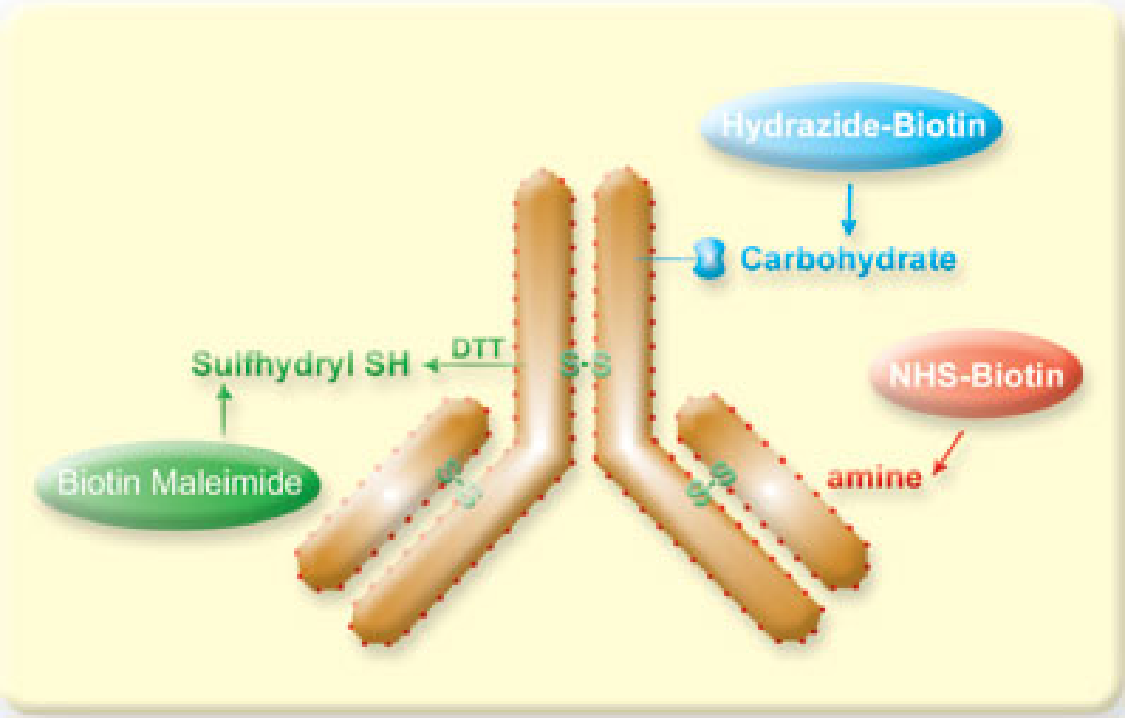

Amine Reactive Labeling

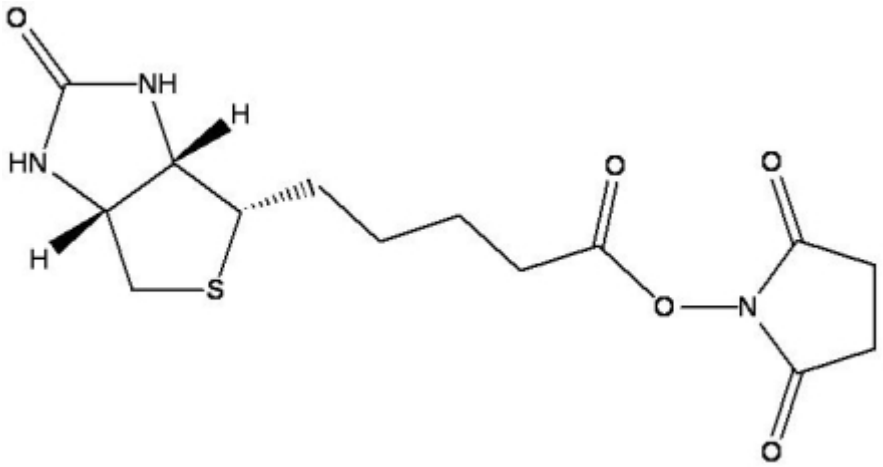

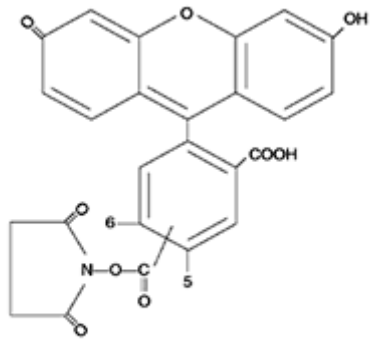

NHS-Fluorescein
MW 473.4

Sulfhydryl Labeling

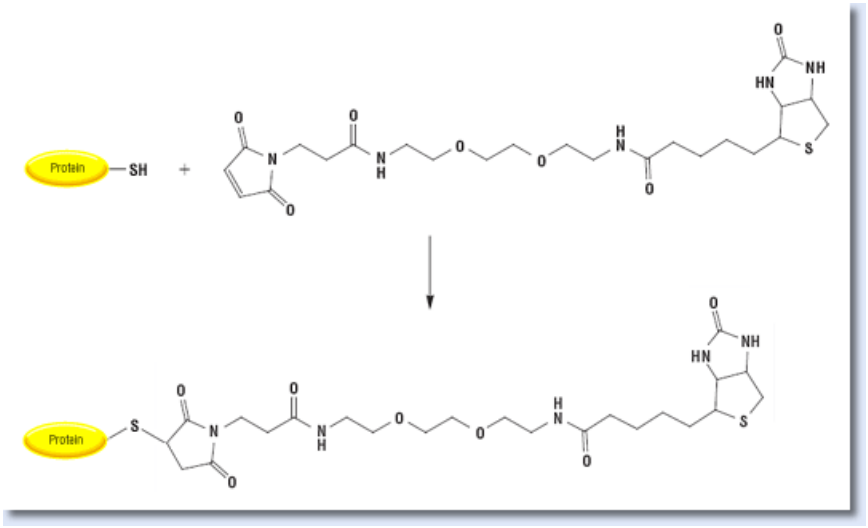

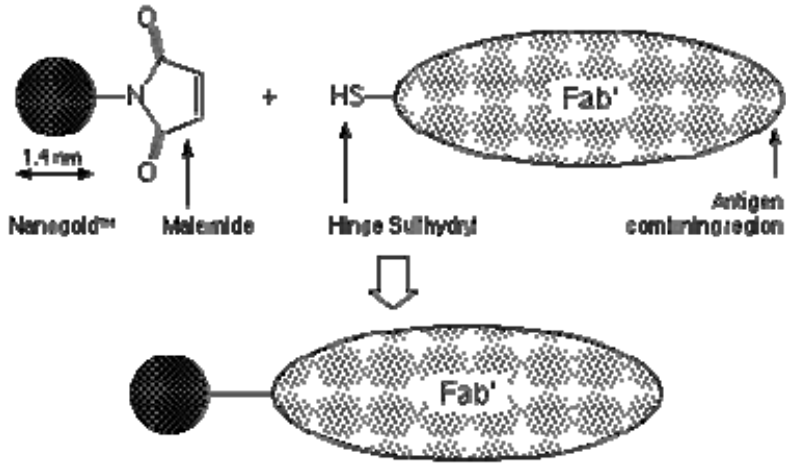

Biotin modification

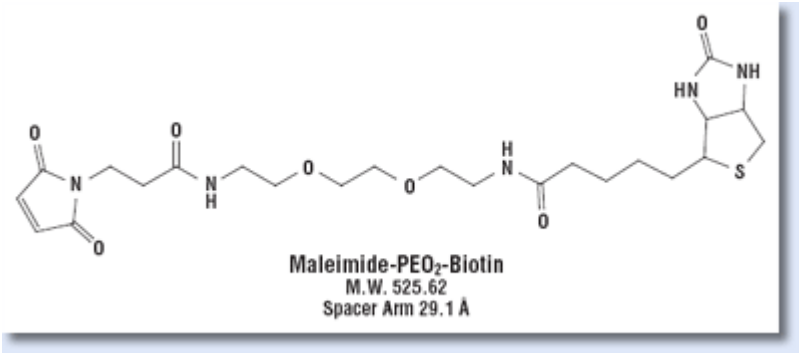

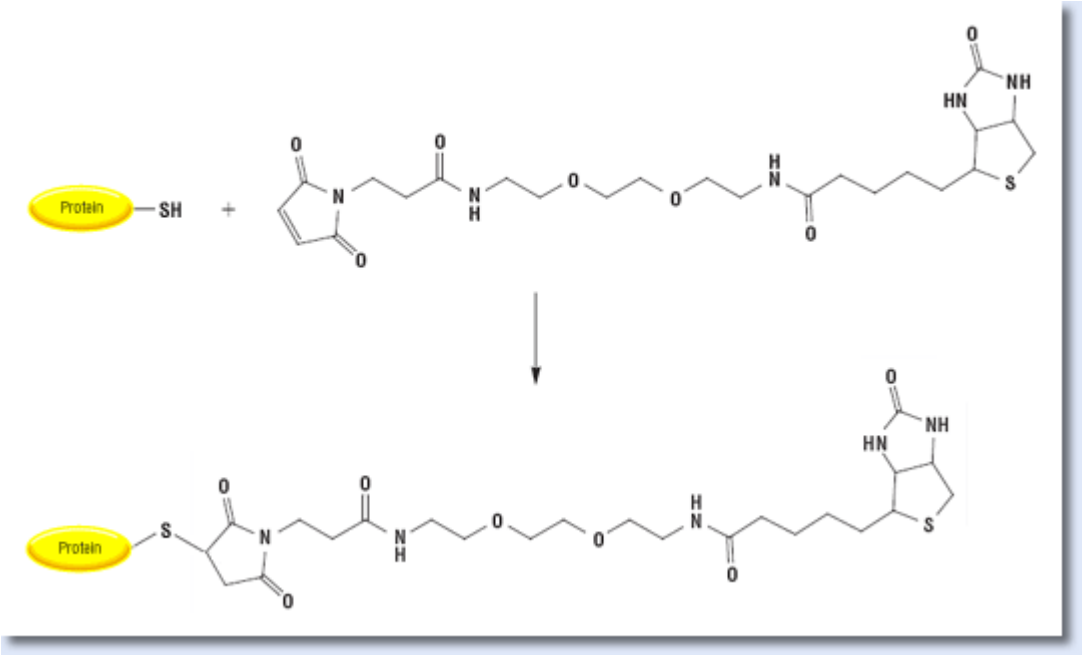

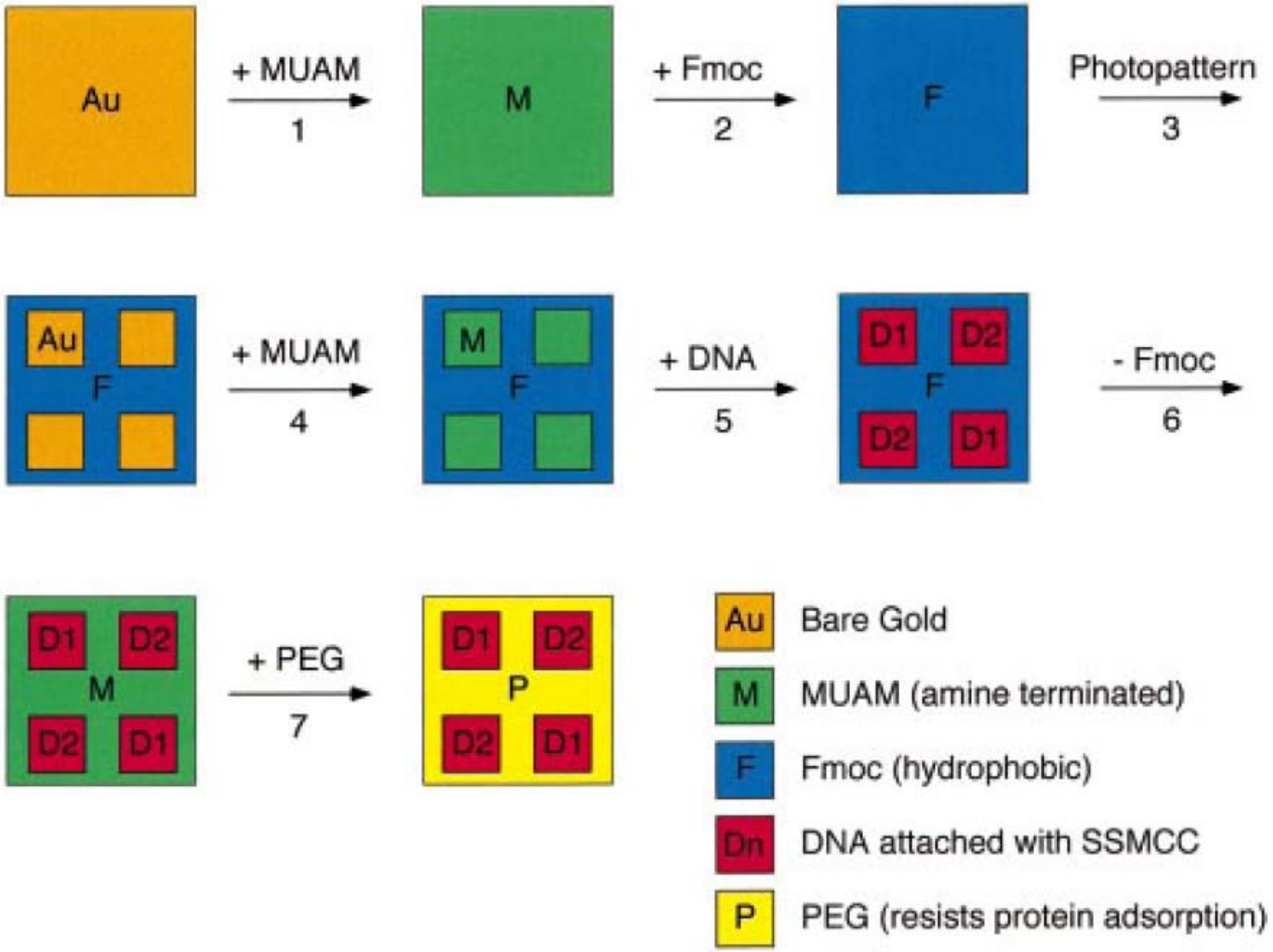

Figure 1. Fabrication scheme for the construction of multi-element DNA arrays. A clean gold surface is reacted with the amine-terminated alkanethiol MUAM, and subsequently reacted with Fmoc-NHS to create a hydrophobic surface. This surface is then exposed to UV radiation through a quartz mask and rinsed with solvent to remove the MUAM+Fmoc from specific areas of the surface, leaving bare gold pads. These bare gold areas on the sample surface are filled in with MUAM, resulting in an array of MUAM pads surrounded by a hydrophobic Fmoc background. Solutions of DNA are then delivered by pipet onto the specific array locations and are covalently bound to the surface via the bifunctional linker SSMCC. In the final two steps, the Fmoc-terminal groups on the array background are removed and replaced by PEG groups which prohibit the nonspecific binding of analyte proteins to the background.

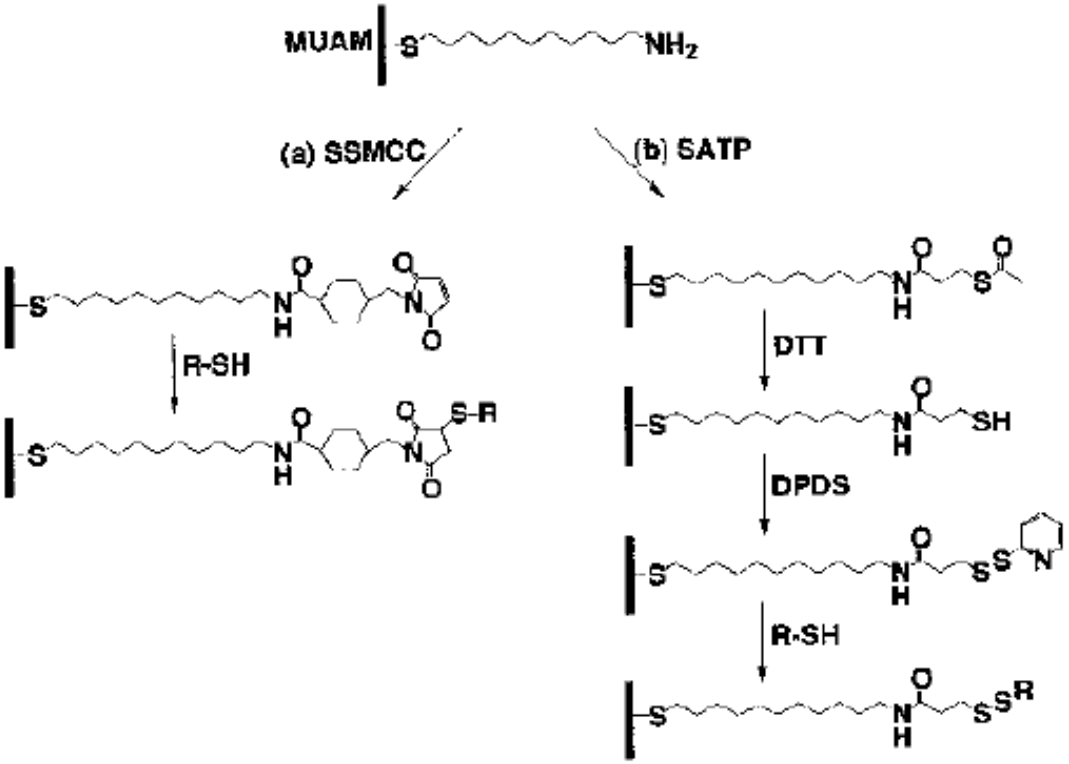

Figure 5.3 Surface attachment chemistry for the immobilization of thiol-modified DNA and cysteine-containing peptides: (a) The linker SSMCC is reacted with a well-packed self-assembled monolayer of 11-mercaptoundecylamine (MUAM) to create a maleimide-modified surface. The maleimide surface is then used to covalently attach thiol-modified DNA or cysteine-containing peptides. (b) In the second approach, SATP is reacted with MUAM to create a protected thiol surface. Upon deprotection with a basic solution containing DTT, the free sulfhydryl is reacted with dipyridyl disulfide to create a pyridyl disulfide surface. Thiol–disulfide exchange reactions are used to couple thiol-containing biomolecules to the surface.

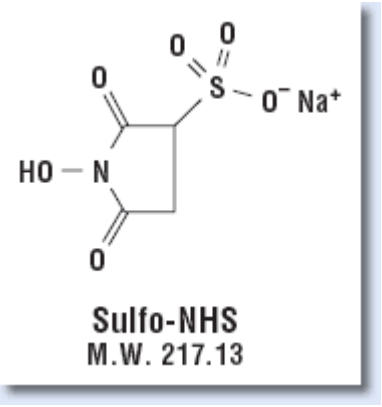

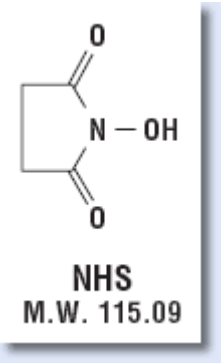

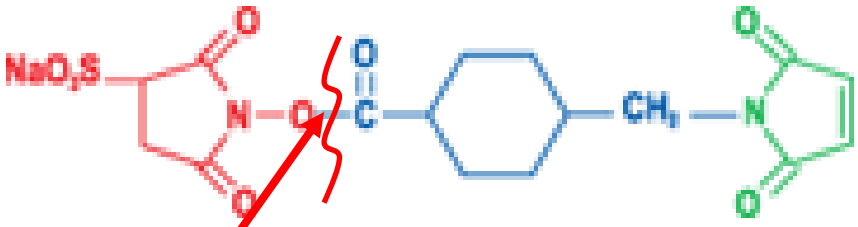

SulfoSuccinimidyl-4-(N-Maleimidomethyl)Cyclohexane-1-Carboxylate
SSMCC

The most popular NH_2- and SH- crosslinker

N-hydroxysuccinimide

NH_2 => amide

$R_1NH_2 + NHS\text{-}R_2 = >R_1NHC{=}OR_2$

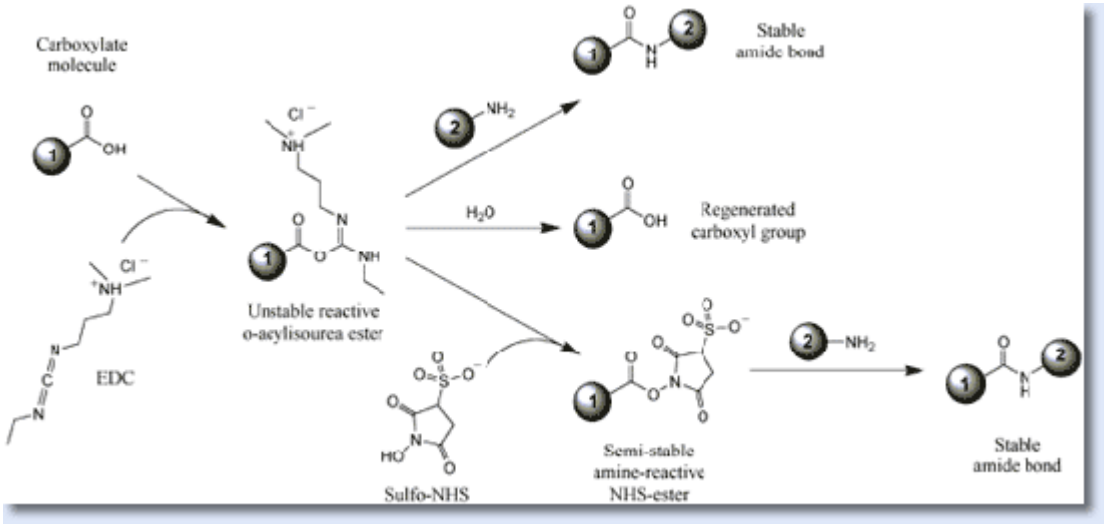

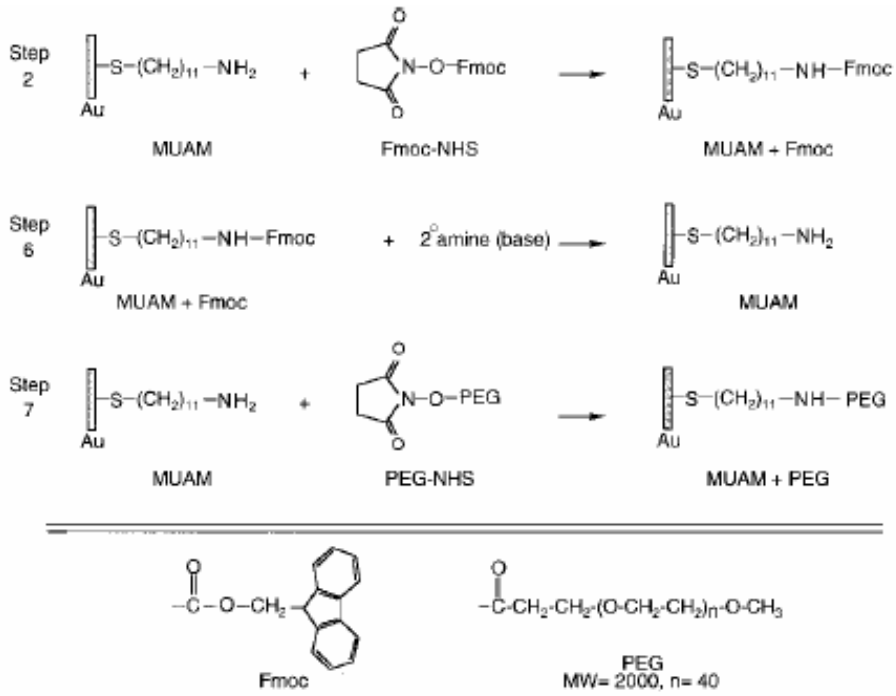

Figure 2. Surface reaction scheme showing the steps involved in the reversible modification of the array background. (Step 2) The starting amine-terminated alkanethiol surface (MUAM) is reacted with the Fmoc-NHS protecting group to form a carbamate linkage thus creating a hydrophobic Fmoc-terminated surface. (Step 6) After DNA immobilization (see Figure 3), the hydrophobic Fmoc group is removed from the surface with a basic secondary amine, resulting in the return of the original MUAM surface. (Step 7) In the final array fabrication step, the deprotected MUAM is reacted with PEG-NHS to form an amide bond that covalently attaches PEG to the array surface.

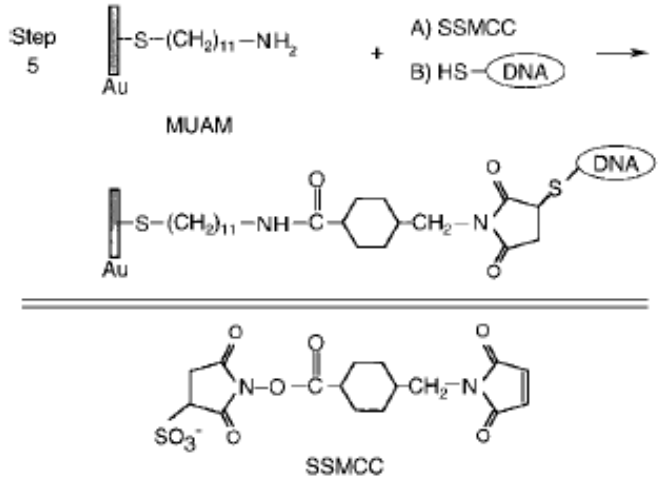

Figure 3. Surface reaction scheme showing the immobilization of thiol-terminated DNA to the array surface. In Step 5 of the DNA array fabrication, the heterobifunctional linker SSMCC is used to attach 5′-thiol modified oligonucleotide sequences to reactive pads of MUAM. This linker contains an NHSS ester functionality (reactive toward amines) and a maleimide functionality (reactive toward thiols). The surface is first exposed to a solution of the linker, whereby the NHSS ester end of the molecule reacts with the MUAM surface. Excess linker is rinsed away and the array surface is then spotted with 5′-thiol-modified DNA that reacts with the maleimide groups forming a covalent bond to the surface monolayer.

Surface Modification

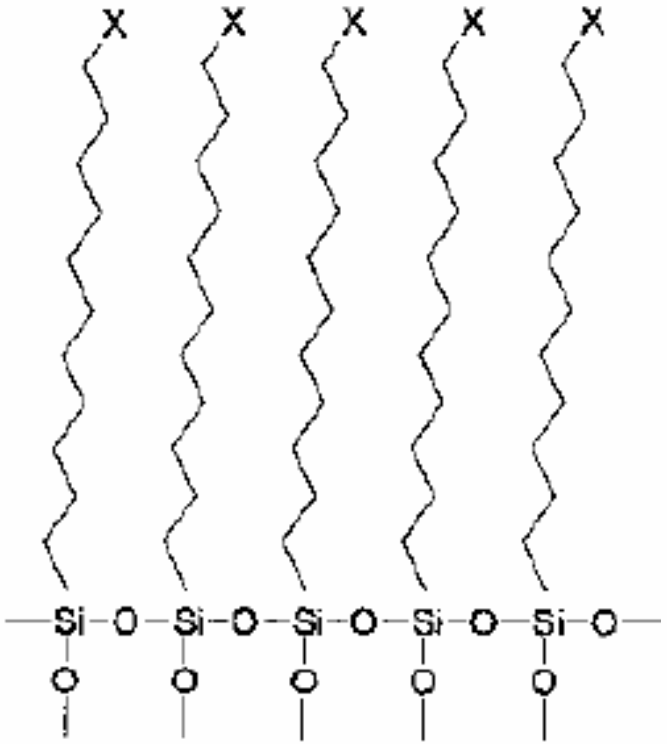

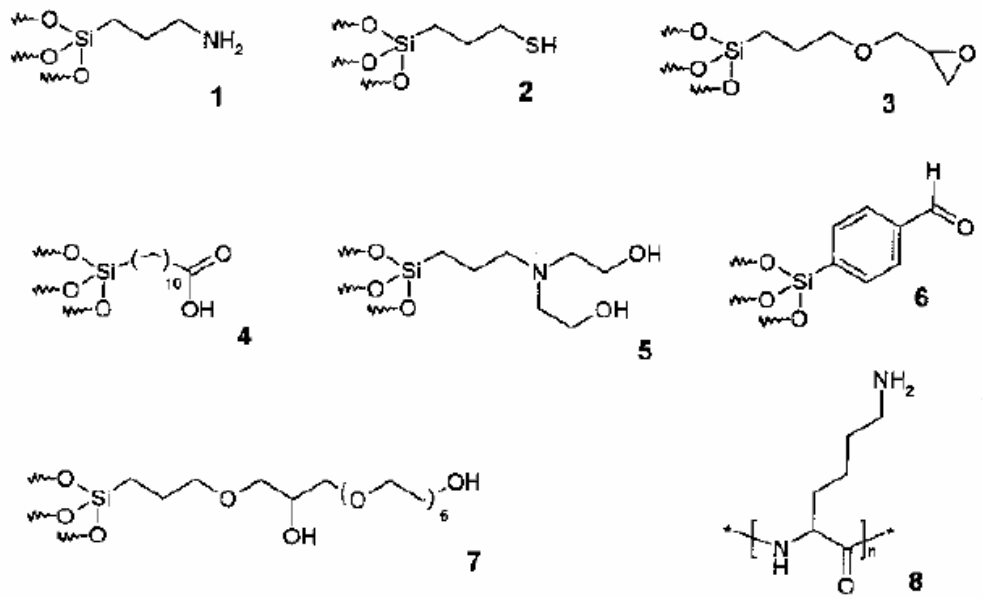

Scheme 2.2 Reagents for derivatization of glass surfaces. 1 APTES = aminopropyltriethoxysilane; **2** MPTS = 3-mercaptopropyltrimethoxysilane; **3** GPTS = glycidoxypropyltrimethoxysilane; **4** TETU = triethoxysilane undecanoic acid; **5** HE-APTS = bis(hydroxyethyl)aminopropyltriethoxysilane); **6** 4-trimethoxysilylbenzaldehyde; **7** GPTS/HEG = glycidoxypropyltrimethoxysilane-hexaethylene glycol; **8** poly(lysine).

Scheme 2.1 2D schematic description of a polysiloxane monolayer on a glass surface (X = terminal functional

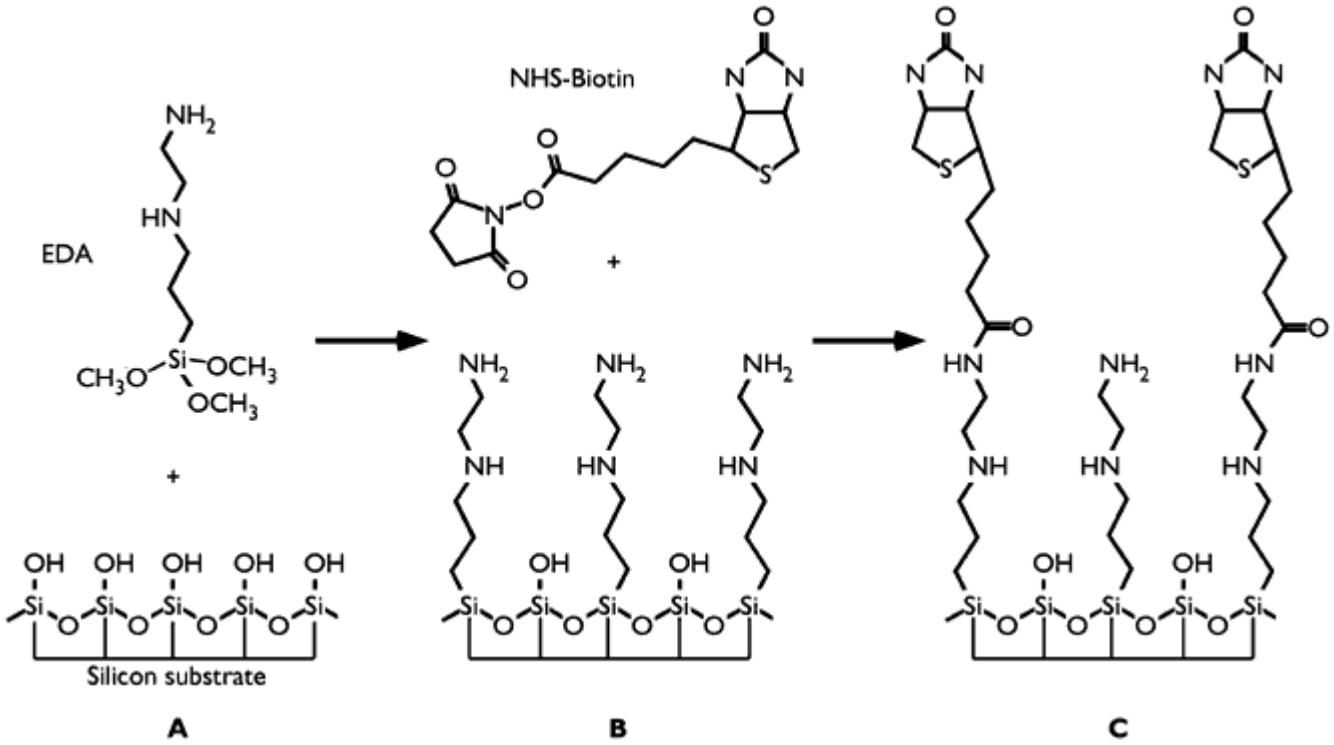
NHS-Biotin
EDA
Silicon substrate
A
B
C

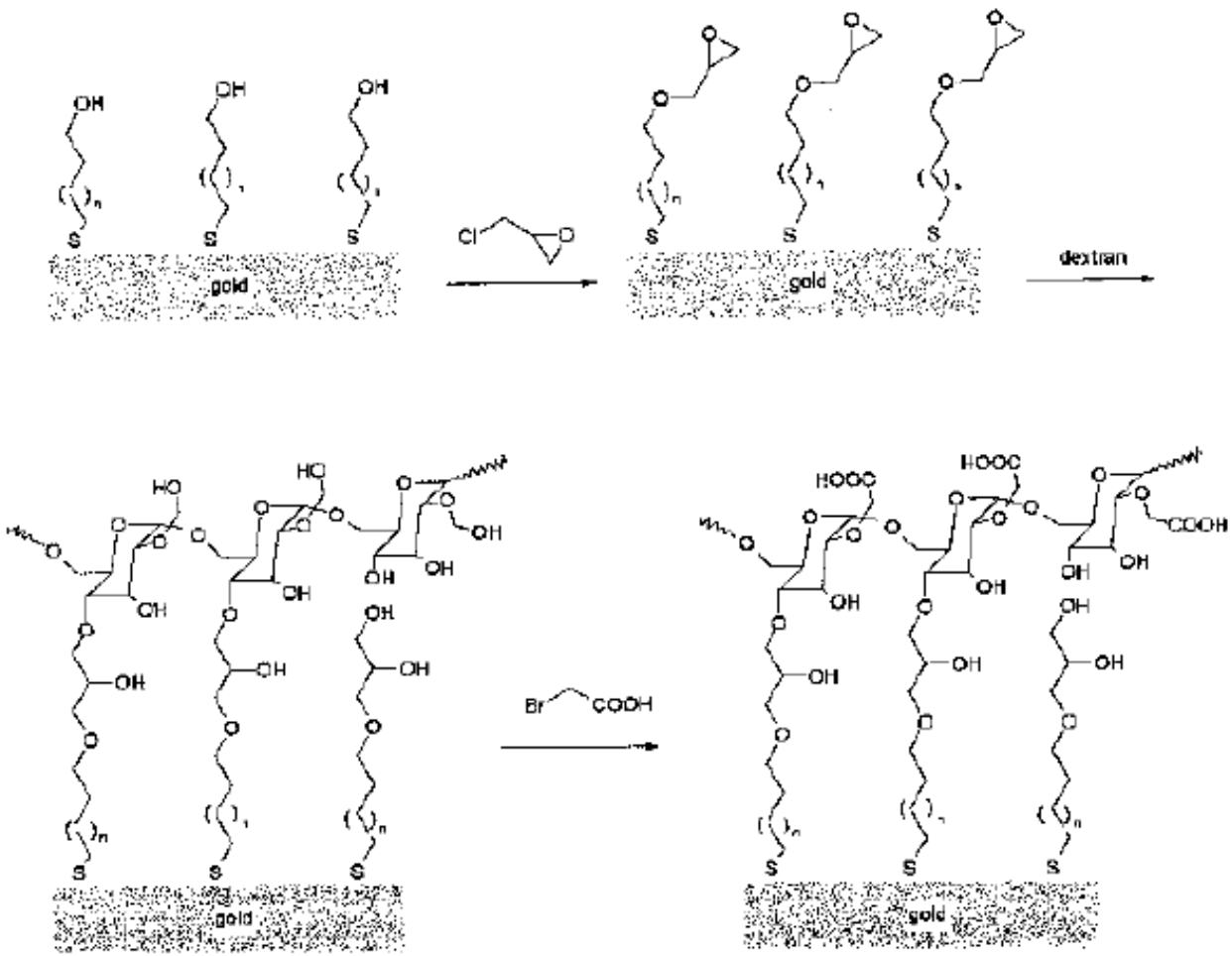

Scheme 2.4 Reaction schemes for preparing a hydrogel dextran matrix [41].

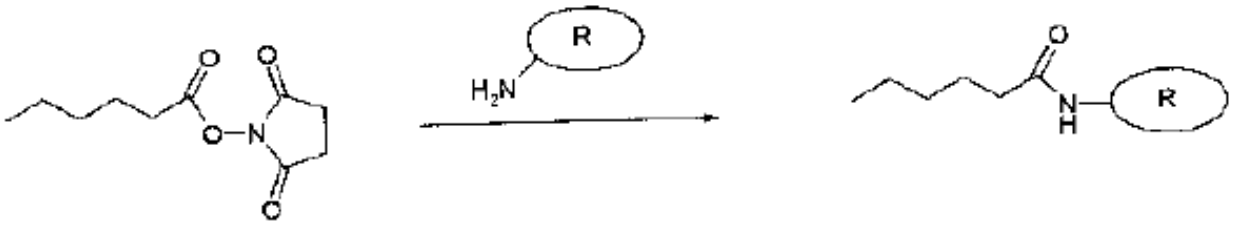

Scheme 2.6 Surface coupling reaction of NHS-esters with the amino residues of the side-chains of polypeptides (lysine units). R, protein.

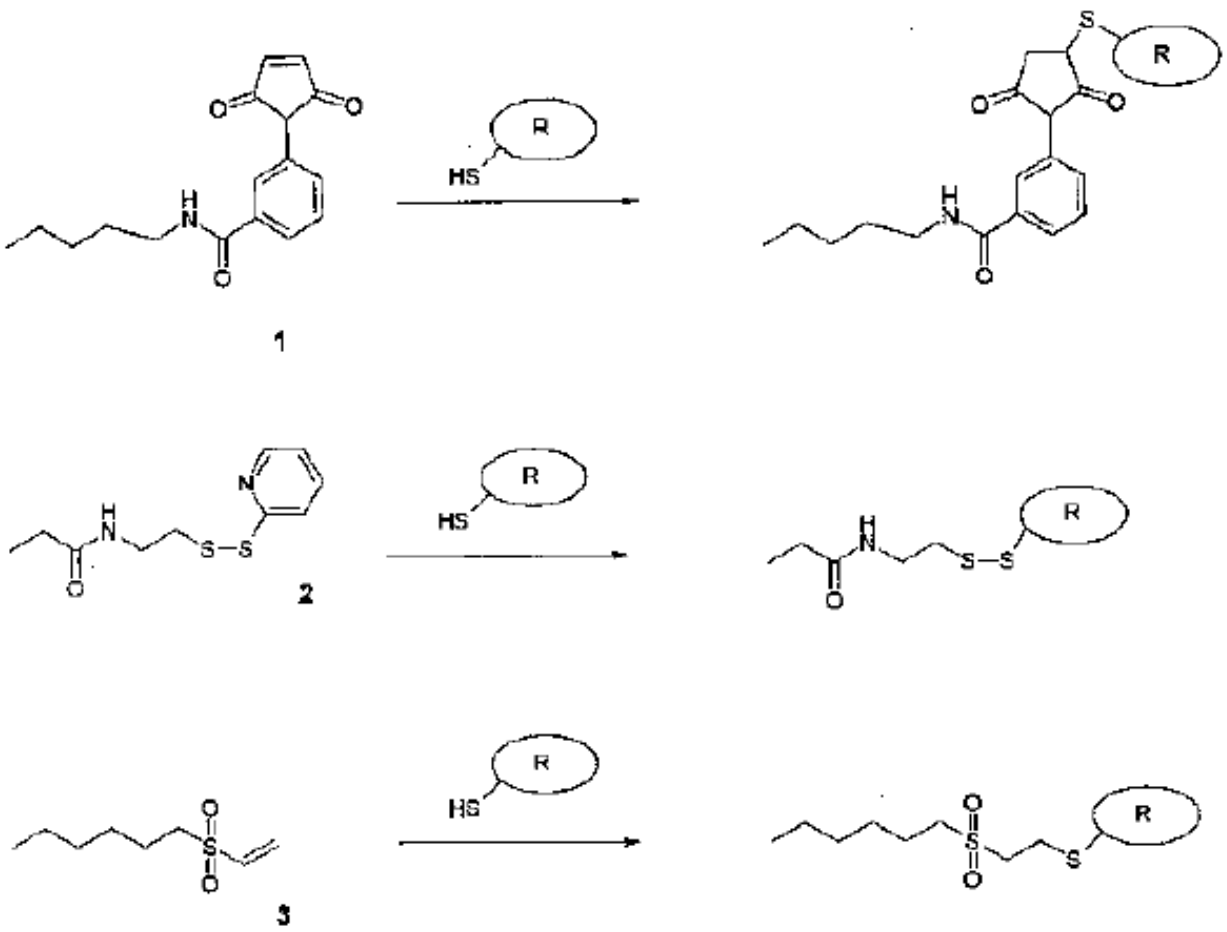

Scheme 2.7 Surface modifications for the attachment of thiol residues (which are present in the side chains) of polypeptides (cysteine units). R, protein, **1**, maleimide; **2**, disulfides; 3, vinyl sulfone.

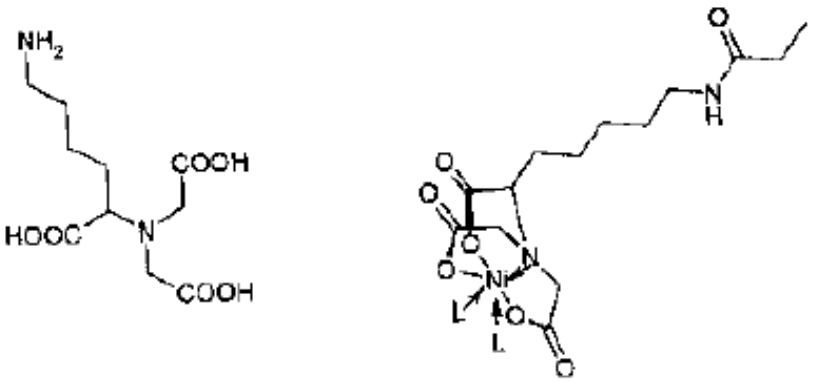

A B

Scheme 2.12 (A) Structure of N-(5-amino-1-carboxypentyl)iminodiacetic acid.
(B) The quadridentate nitrilotriacetic acid (NTA) ligand forms a complex with four binding sites on the nickel metal which is present in the center. The two remaining binding sites can be coordinated with histidine ligands (L).

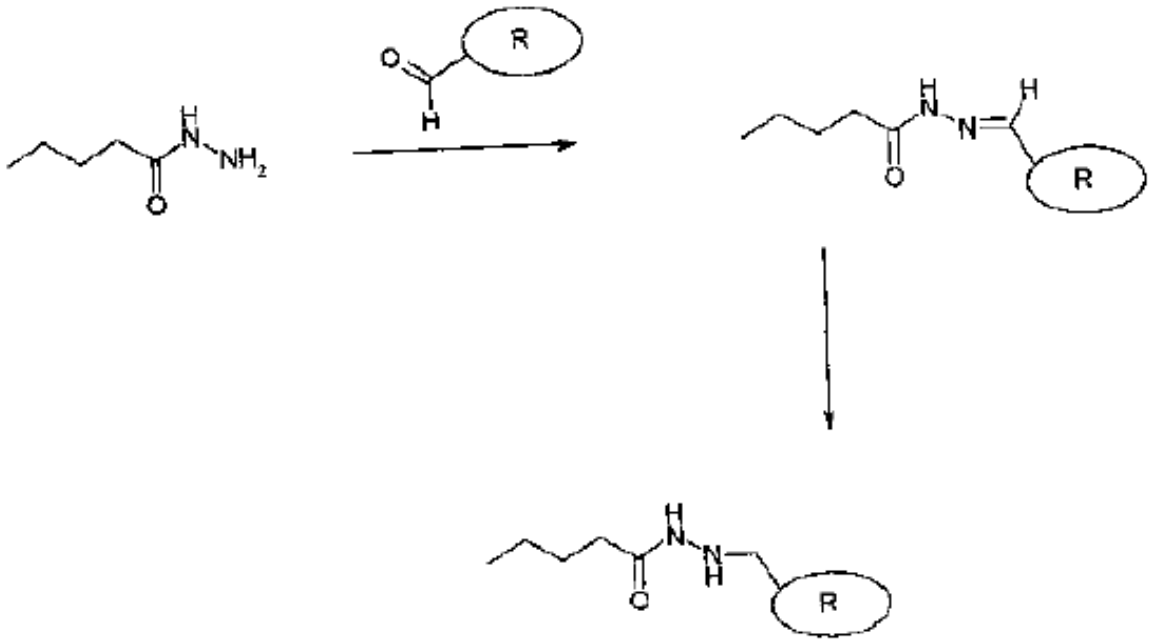

Scheme 2.13 Coupling of aldehyde residues of glycoproteins to hydrazide-terminated monolayers.

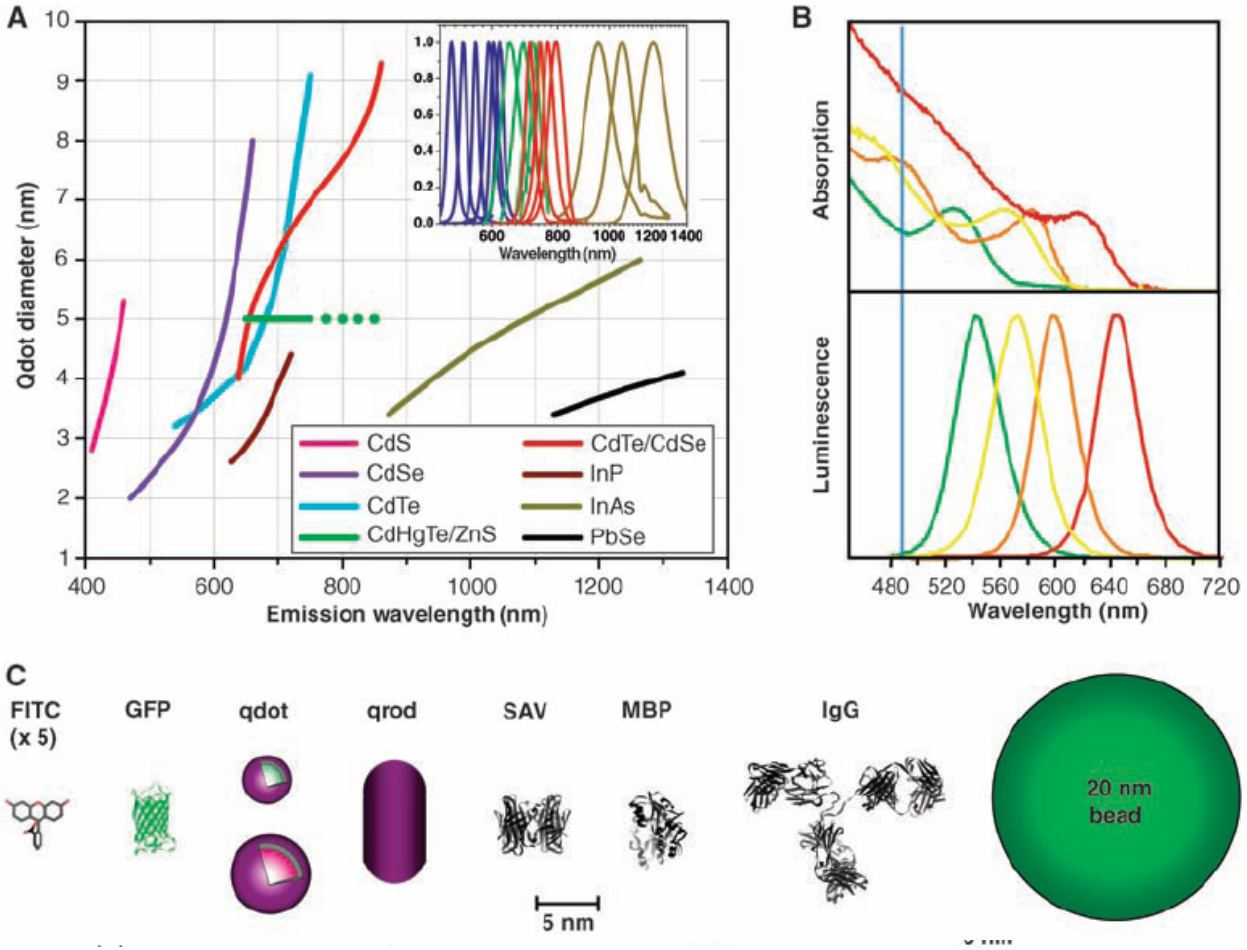

Fig. 1. (**A**) Emission maxima and sizes of quantum dots of different composition. Quantum dots can be synthesized from various types of semiconductor materials (II-VI: CdS, CdSe, CdTe…; III-V: InP, InAs…; IV-VI: PbSe…) characterized by different bulk band gap energies. The curves represent experimental data from the literature on the dependence of peak emission wavelength on qdot diameter. The range of emission wavelength is 400 to 1350 nm, with size varying from 2 to 9.5 nm (organic passivation/solubilization layer not included). All spectra are typically around 30 to 50 nm (full width at half maximum). Inset: Representative emission spectra for some materials. Data are from (*12*, *18*, *27*, *76*–*82*). Data for CdHgTe/ZnS have been extrapolated to the maximum emission wavelength obtained in our group. (**B**) Absorption (upper curves) and emission (lower curves) spectra of four CdSe/ZnS qdot samples. The blue vertical line indicates the 488-nm line of an argon-ion laser, which can be used to efficiently excite all four types of qdots simultaneously. [Adapted from (*28*)] (**C**) Size comparison of qdots and comparable objects. FITC, fluorescein isothiocyanate; GFP, green fluorescent protein; qdot, green (4 nm, top) and red (6.5 nm, bottom) CdSe/ZnS qdot; qrod, rod-shaped qdot (size from Quantum Dot Corp.'s Web site). Three proteins—streptavidin (SAV), maltose binding protein (MBP), and immunoglobulin G (IgG)—have been used for further functionalization of qdots (see text) and add to the final size of the qdot, in conjunction with the solubilization chemistry (Fig. 2).

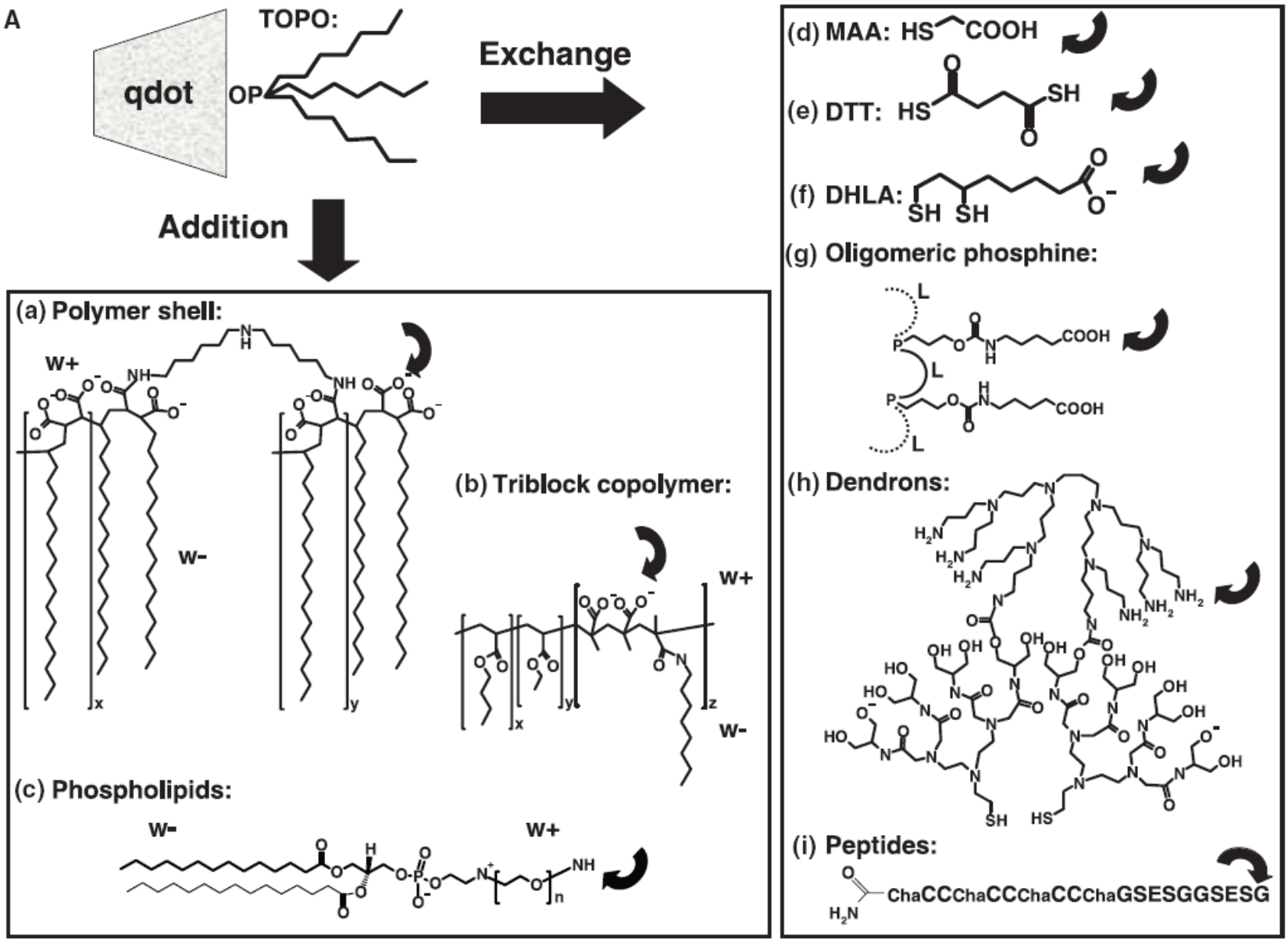
A
qdot
TOPO:
OP
Exchange
Addition
(a) Polymer shell:
W+
W-
(b) Triblock copolymer:
W+
W-
(c) Phospholipids:
W-
W+
(d) MAA: HS COOH
(e) DTT: HS SH
(f) DHLA: SH SH
(g) Oligomeric phosphine:
COOH
COOH
(h) Dendrons:
(i) Peptides:
ChaCCChaCCChaCCChaGSESGGSESG

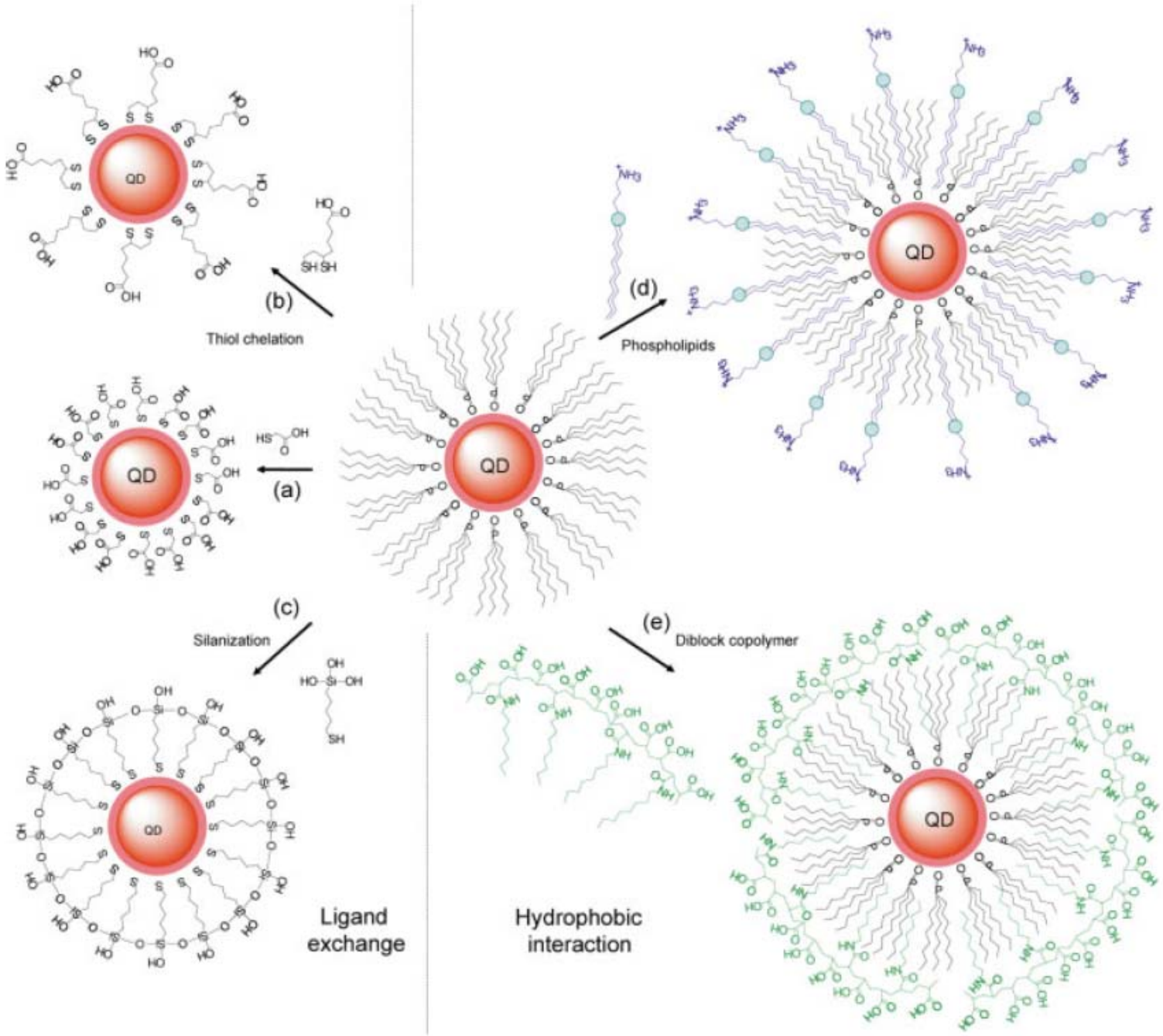
QD
(a)
(b)
Thiol chelation
(c)
Silanization
Ligand exchange
(d)
Phospholipids
(e)
Diblock copolymer
Hydrophobic interaction

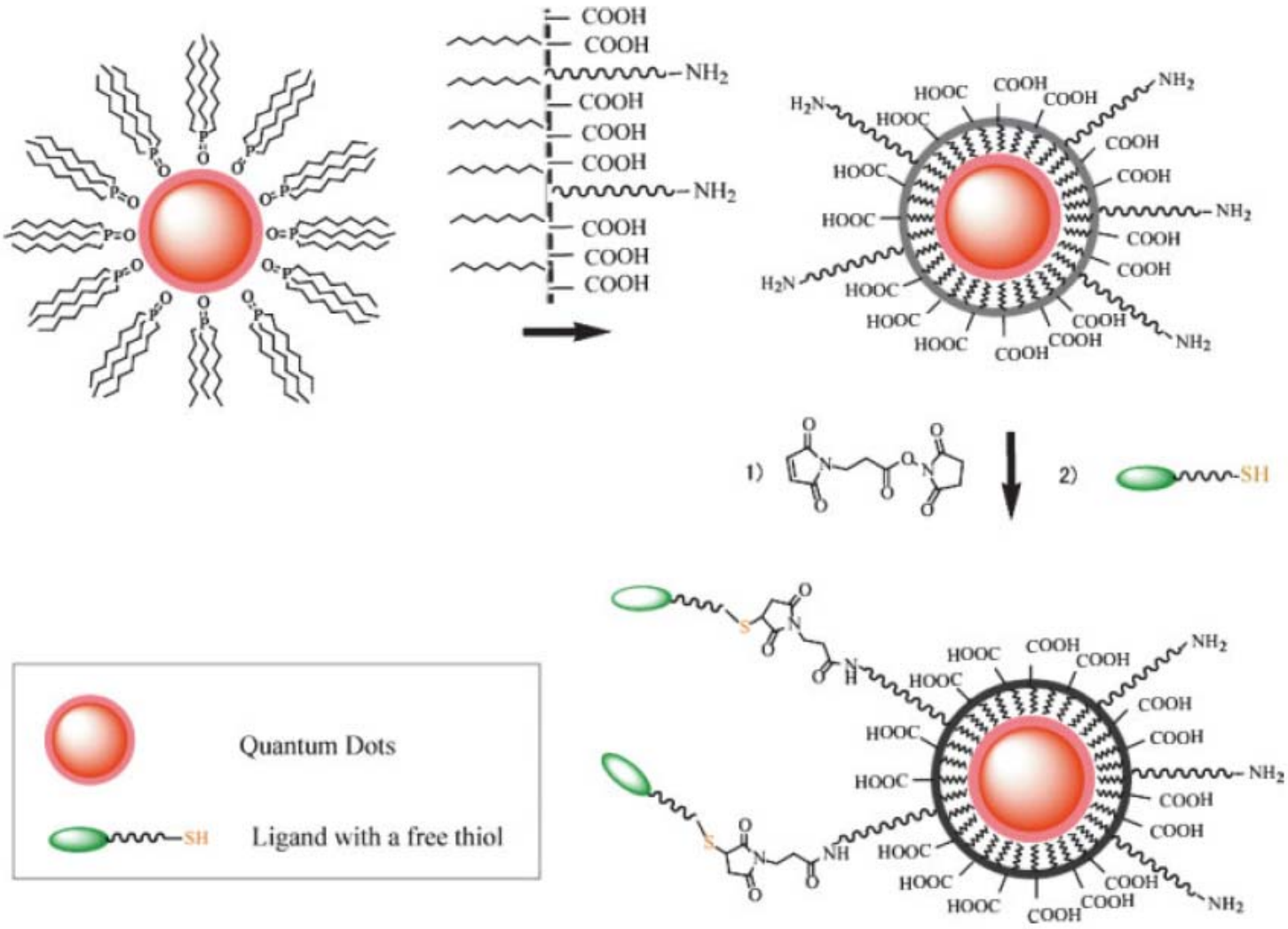

FIGURE 3 Maleimide functionalized QDs for conjugating thiol-containing ligands. TOPO stabilized QDs are coated with a primary amine functionalized tri-block amphiphilic copolymer for producing water-soluble QDs, which facilitate further conjugation to ligands with free thiols through bi-functional cross-linkers.

Cells incubated with tiopronin coated QDs

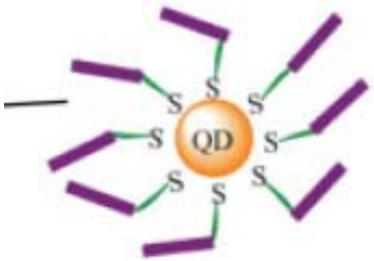

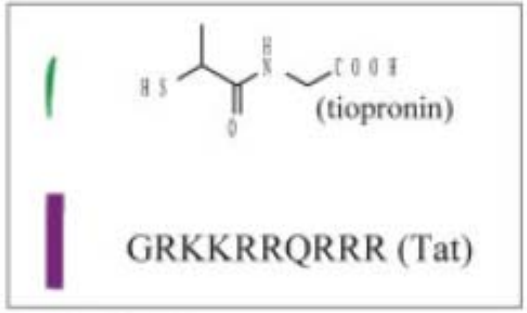

Cells incubated with Tat functionlized QDs

Scheme 1. Modular Design of Hydrophilic Ligands with Terminal Functional Groups Used in This Study

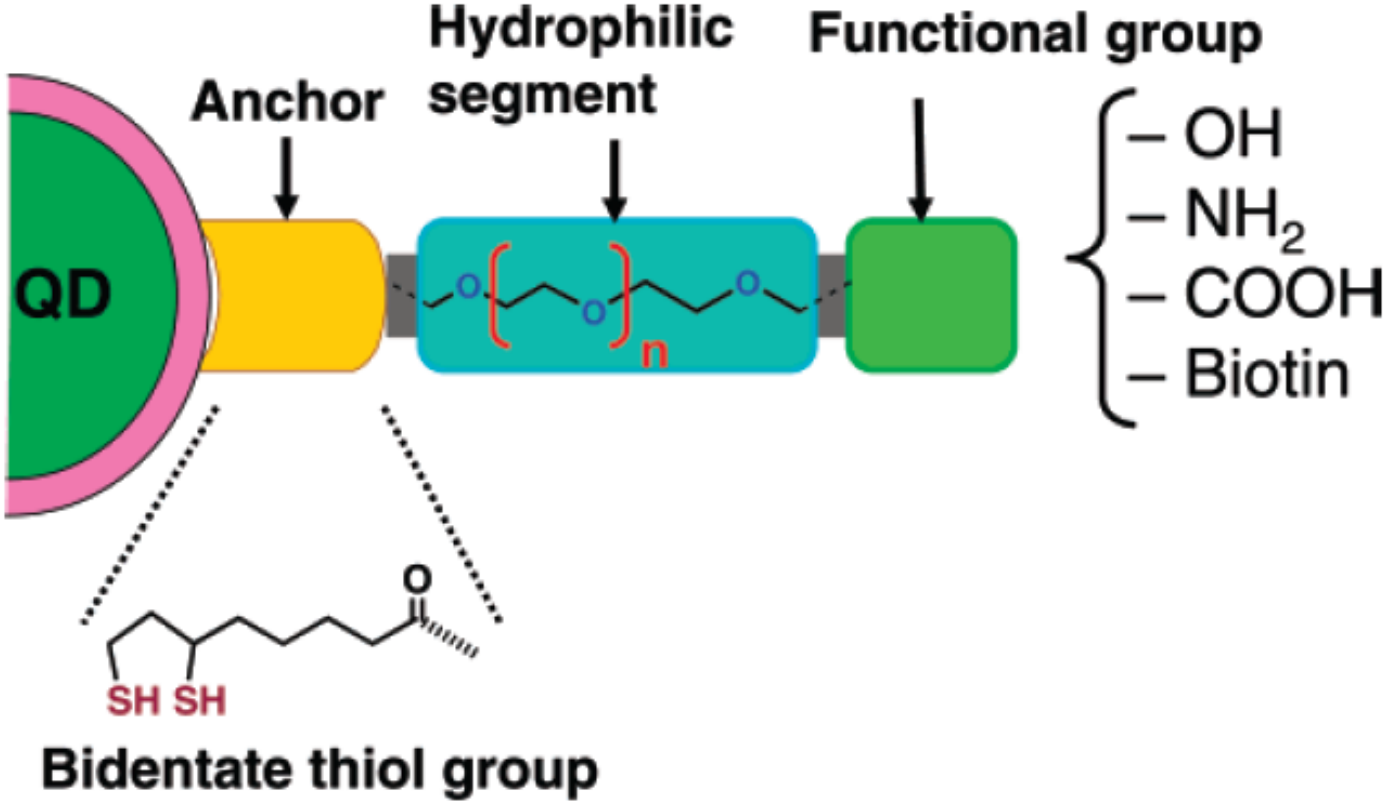

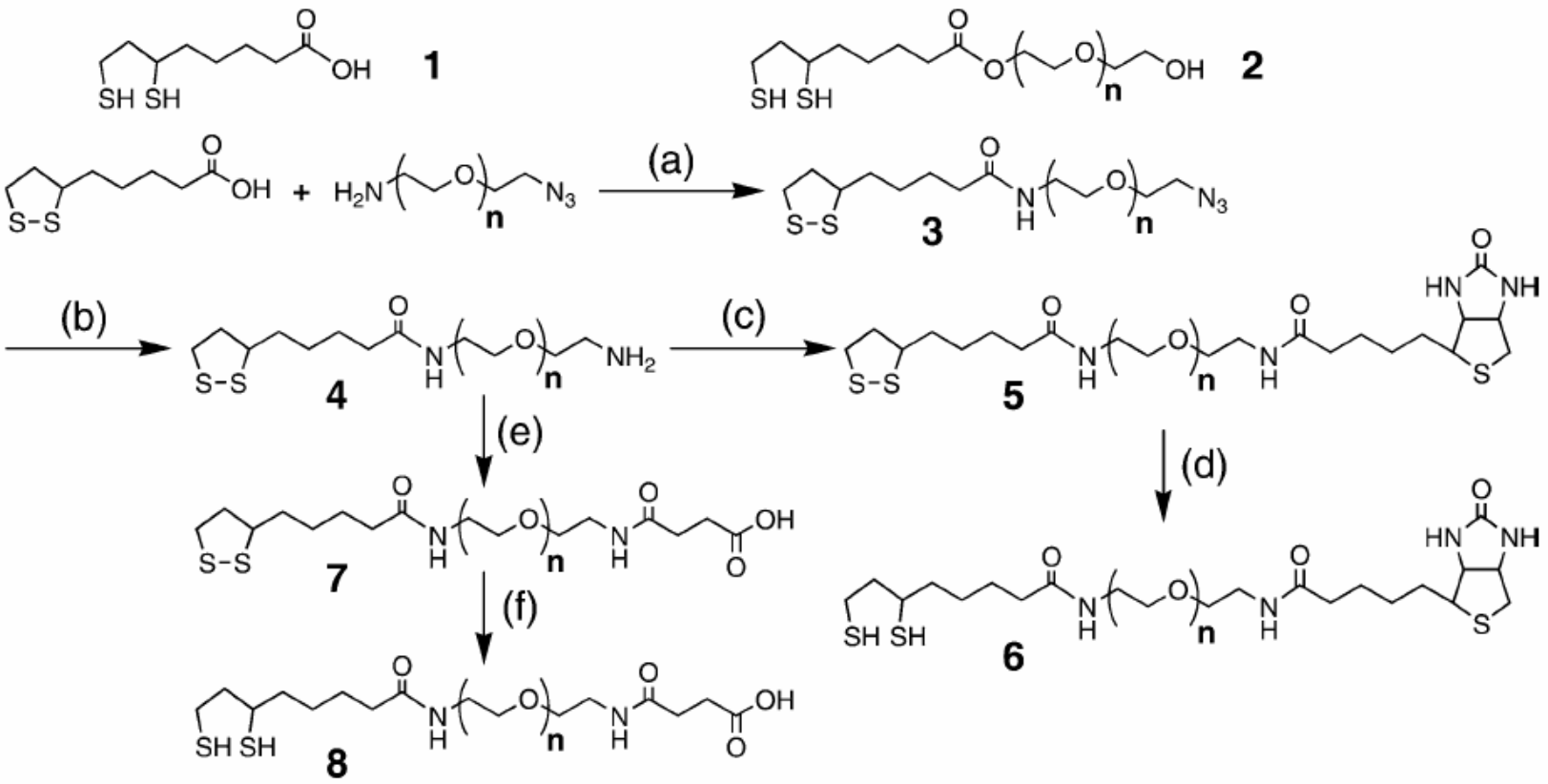

Figure 1. Chemical structures and synthetic routes of the surface ligands used in this study: (a) DCC, DMAP, CH_2Cl_2; (b) PPh_3, H_2O, THF; (c) biotin *N*-hydroxysuccinimide ester, Et_3N, DMF; (d) $NaBH_4$, EtOH, H_2O; (e) succinic anhydride, pyridine; (f) $NaBH_4$, EtOH, H_2O.

Fig. 2. Qdot solubilization and functionalization. (**A**) Surface chemistries. TOPO (trioctylphosphine oxide)–passivated qdots can be solubilized in aqueous buffer by addition of a layer of amphiphilic molecules containing hydrophilic (w+) and hydrophobic (w–) moieties, or by exchange of TOPO with molecules that have a Zn-coordinating end (usually a thiol group, SH) and a hydrophilic end. Examples of addition include (a) formation of a cross-linked polymer shell (*31*), (b) coating with a layer of amphiphilic triblock copolymer (*26*), and (c) encapsulation in phospholipid micelles (*29*). Examples of exchange include (d) mercaptoacetic acid (MAA) (*20*), (e) dithiothreitol (DTT) (*21*), (f) dihydrolipoic acid (DHLA) (*33*), (g) oligomeric phosphines (*22*), (h) cross-linked dendrons (*23*), and (i) peptides (*24*). The curved arrow indicates sites available for further functionalization. (**B**) Peptide toolkit. The light blue segment contains cysteines and hydrophobic amino acids ensuring binding to the qdot (*24*) and is common to all peptides. S, solubilization sequence; P, PEG; B, biotin; R, peptide recognition sequence; Q, quencher; D, DOTA; X, any unspecified peptide-encoded function. Qdot solubilization is obtained by a mixture of S and P. Qdots can be targeted with B, R, or other chemical moieties. Qdot fluorescence can be turned on or off by attaching a Q via a cleavable peptide link. In the presence of the appropriate enzyme, the quencher is separated from the qdot, restoring the photoluminescence and reporting on the enzyme activity. For simultaneous PET and fluorescence imaging, qdots can be rendered radioactive by D chelation of radionuclides; for simultaneous MRI and fluorescence imaging, qdots can be rendered radioactive by D chelation of nuclear spin labels.

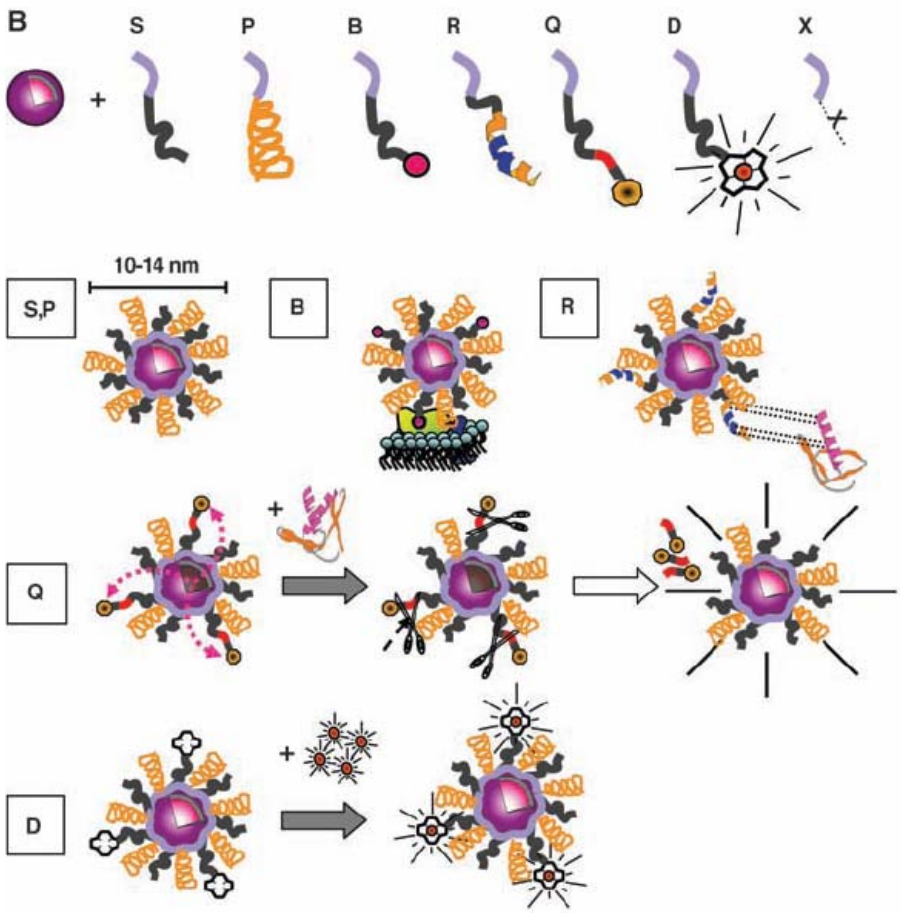

Chapter 26
SPR/SERS

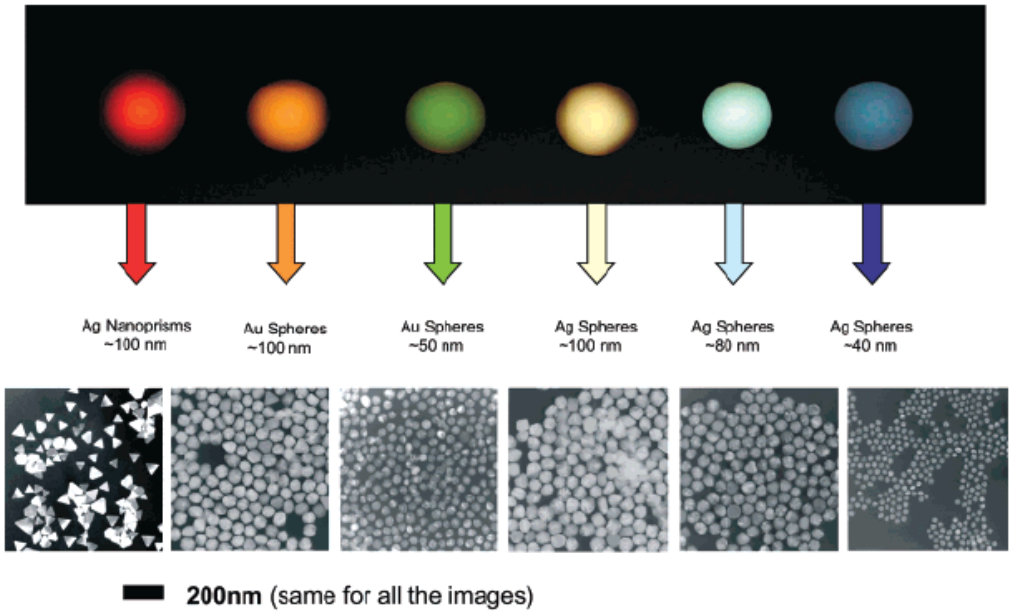

Figure 1. Sizes, shapes, and compositions of metal nanoparticles can be systematically varied to produce materials with distinct light-scattering properties.

Shape-Controlled Synthesis and Surface Plasmonic Properties of Metallic Nanostructures

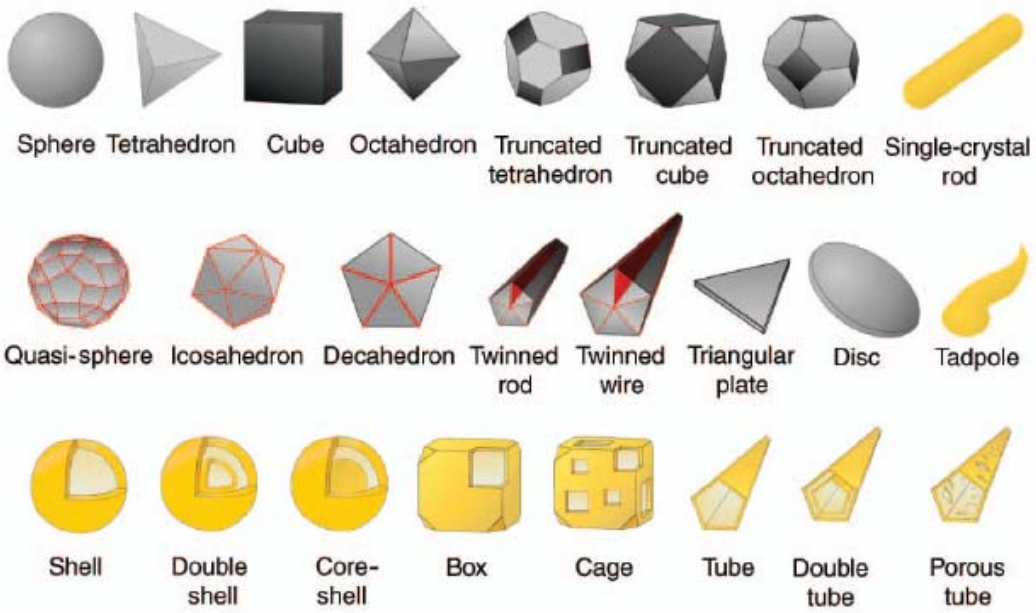

Figure 1. Schematic illustration of nanostructure shapes. The shapes in the top row are single crystals, in the second row are particles with twin defects or stacking faults, and in the third row are gold shells. All twinned and single-crystal shapes shown, with the exception of the octahedron, can be synthesized in solution. Control of shape allows control of optical and catalytic properties, as well as suitability for electronic applications in the case of wires, tubes, and possibly rods. Dark facets are (100) planes, light gray are (111) planes, and {111} twin planes are shown in red. Gold shapes represent gold particles, and gray shapes represent silver particles, although spheres, twinned rods, icosahedrons, and cubes can also be made from gold.

For a bulk metal with infinite sizes in all three dimensions, ω_p can be expressed as

$$\omega_p = (Ne^2/\varepsilon_0 m_e)^{1/2}, \quad (1)$$

where N is the number density of electrons, ε_0 is the dielectric constant of a vacuum, and e and m_e are the charge and effective mass of an electron, respectively. Quantized plasma oscillations are called *plasmons*.

Drift: Drude model

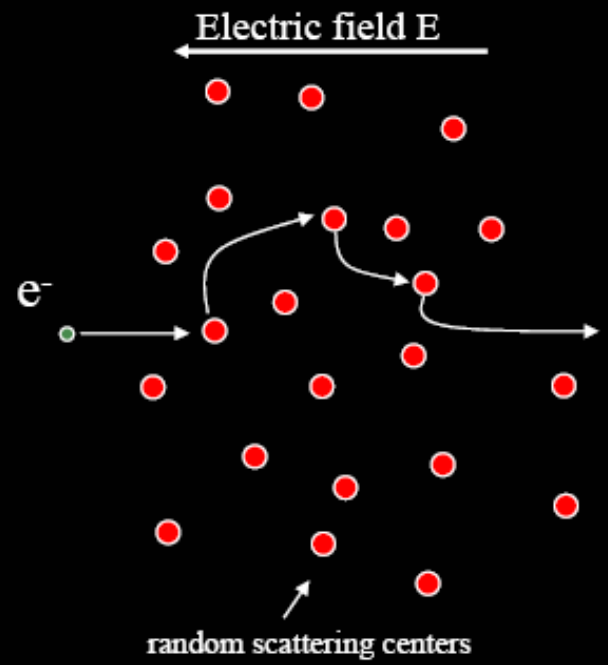

$$F = ma$$

$$eE = m\frac{\partial v}{\partial t}$$

$$v_{avg} = \underbrace{\frac{e\tau}{m}}_{\mu} E$$

$$j = nev_{avg} = \underbrace{\frac{ne^2\tau}{m}}_{\sigma} E$$

$$m\frac{\partial}{\partial t}\langle\vec{v}\rangle = q\vec{E} - \gamma\langle\vec{v}\rangle$$

$$\sigma(\omega) = \frac{\sigma_0}{1 + i\omega\tau}$$

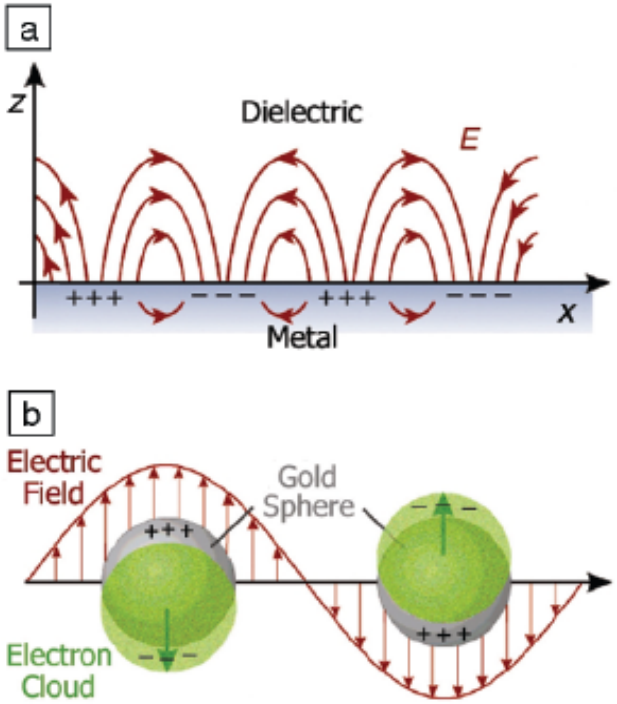

Figure 2. Schematic illustration of the collective oscillations of free electrons for (a) a metal–dielectric interface and (b) a spherical gold colloid. Excited by the electric field of incident light, the free electrons can be collectively displaced from the lattice of positive ions (consisting of nuclei and core electrons). While the plasmon shown in (a) can propagate across the surface as a charge density wave, the plasmon depicted in (b) is localized to each particle. (Courtesy of R. Van Duyne and T. Schatz, Northwestern University.)

Thin film
Nanoparticle
Nanoparticle array

Far-Field Optical Microscopy of Single Metal Nanoparticles

Acc. Chem. Res. **2005**, *38*, 594–601

The optical properties of metals are, to a large extent, determined by conduction electrons. The response of these free electrons follows the Drude model. They collectively react to perturbation by an external electric field. The Coulomb restoring force between the electrons and the lattice leads to harmonic oscillations with the plasma frequency $\omega_p^2 = Ne^2/(m_e\epsilon_0)$ where N is the electron density and m_e the electron mass. The damping of the oscillation is described by a phenomenological damping constant, γ. In this model, the dielectric function, $\epsilon(\omega)$, equals

$$\epsilon(\omega) = 1 - \frac{\omega_p^2}{\omega(\omega + i\gamma)}$$

For noble metals, the contribution of the bound d-electrons to the optical properties cannot be neglected.[9]

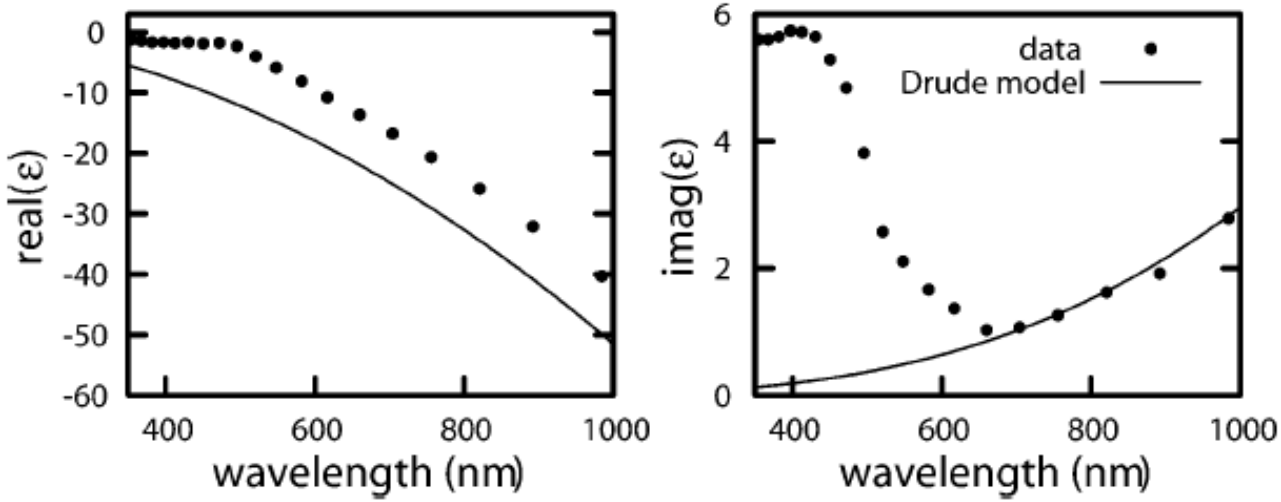

FIGURE 1. Dielectric function of gold[8] compared with the free electron model of Drude. The deviations are due to the interband contribution.

$$\sigma_{\text{ext}} = \sigma_{\text{abs}} + \sigma_{\text{sca}}.$$

Mie's theory

$$\sigma_{\text{ext}} = 2\frac{2\pi}{k^2}x^3\ \text{Im}\left(\frac{m^2-1}{m^2+2}\right)$$

$$m^2 = \frac{\epsilon_{\text{metal}}}{\epsilon_{\text{medium}}} \qquad -2$$

$$\sigma_{\text{sca}} = \frac{4}{3}\frac{2\pi}{k^2}x^6\left|\frac{m^2-1}{m^2+2}\right|^2$$

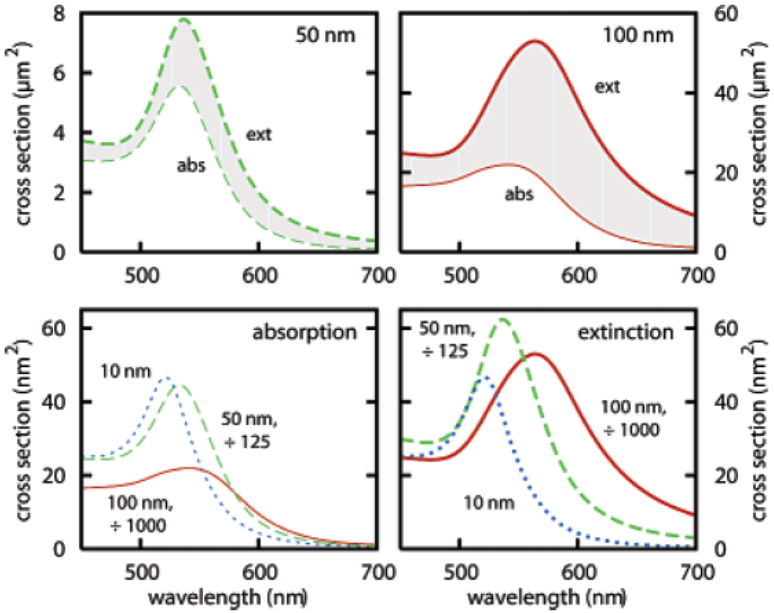

FIGURE 2. Extinction (thick lines) and absorption (thin lines) spectra of gold particles with a diameter of 10 nm (blue, dotted), 50 nm (green, dashed), and 100 nm (red, solid) plotted in different combinations of the same curves. The surrounding medium is water ($n = 1.3$). In the top panels, with increasing colloid size the additional scattering contribution to the extinction becomes more important; the gap between absorption and scattering spectra gets larger. In the bottom panels to compare colloids of different sizes the spectra are scaled with d^3 to the 10-nm particle. Both absorption and scattering spectra show a red shift and broadening of the plasmon resonance with particle size.

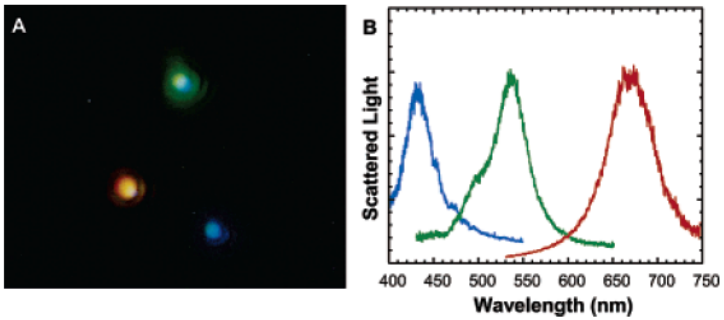

FIGURE 3. Dark-field image of silver particles of different sizes leading to different colors in the scattered white light.[15] The spot size is about 400 nm, and the height of the image is about 9 μm. The corresponding spectra are shown in the right panel. Reprinted with permission from ref 15. Copyright 2000 National Academy of Sciences, U.S.A.

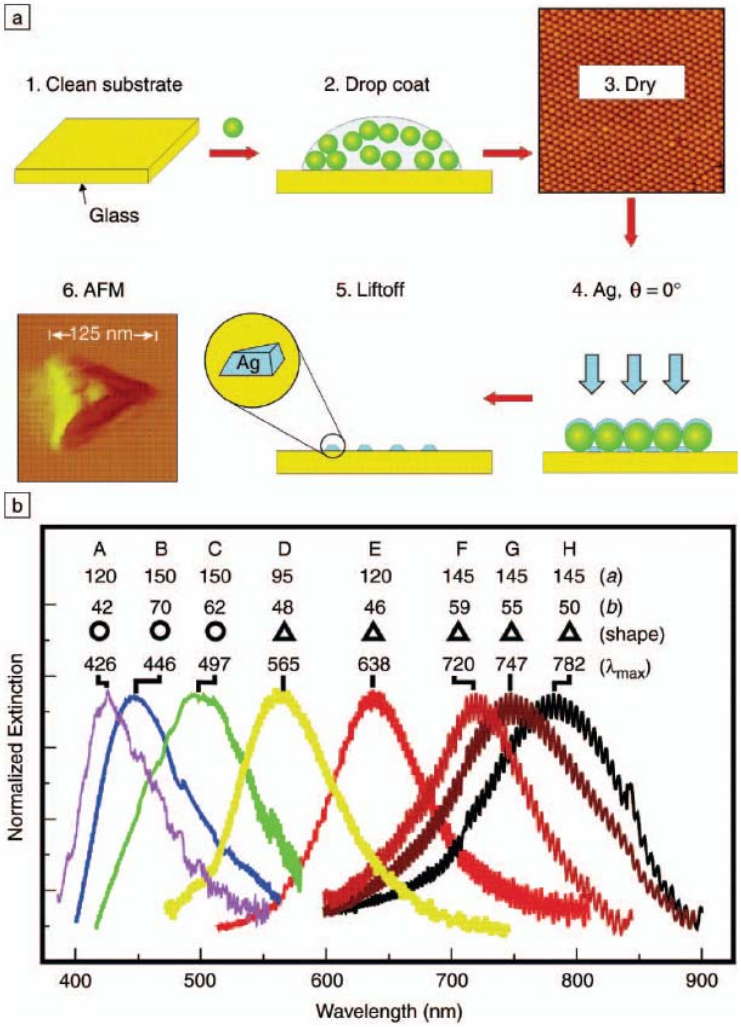

Figure 1. (a) Schematic representation of the nanosphere lithography (NSL) fabrication process. The AFM image in step 3 is 5 μm × 5 μm. (b) Size- and shape-tunable localized surface plasmon resonance spectra of various Ag nanoparticles (labeled A–H) fabricated by NSL. The wavelength of maximum extinction, λ_{max}, is changed by varying the in-plane width a *and out-of-plane height* b *of the nanoparticles.*

The simplest theoretical approach available for modeling the optical properties of nanoparticles is classical electrodynamics (i.e., solving Maxwell's equations with the metal dielectric constant taken from bulk measurements). For spherical particles, this leads to the following (Mie theory) expression for the extinction coefficient $E(\lambda)$ in the long-wavelength limit:[23]

$$E(\lambda) = \frac{24\pi N_A a^3 \varepsilon_m^{3/2}}{\lambda \ln(10)} \times \left[\frac{\varepsilon_i}{(\varepsilon_r + 2\varepsilon_m)^2 + \varepsilon_i^2} \right]. \quad (1)$$

Here, N_A is the areal density of the nanoparticles, a is the radius of the metallic nanosphere, ε_m is the dielectric constant of the medium surrounding the nanosphere (assumed to be a positive, real number), λ is the wavelength, and ε_r and ε_i are the real and imaginary parts of the metal dielectric function. This formula predicts a resonant peak when $\varepsilon_r = -2\varepsilon_m$, which for silver and gold occurs in the visible portion of the spectrum. In addition, any change in the dielectric constant of the medium (e.g., when molecules adsorb on the particle) leads to a change in the resonance wavelength.

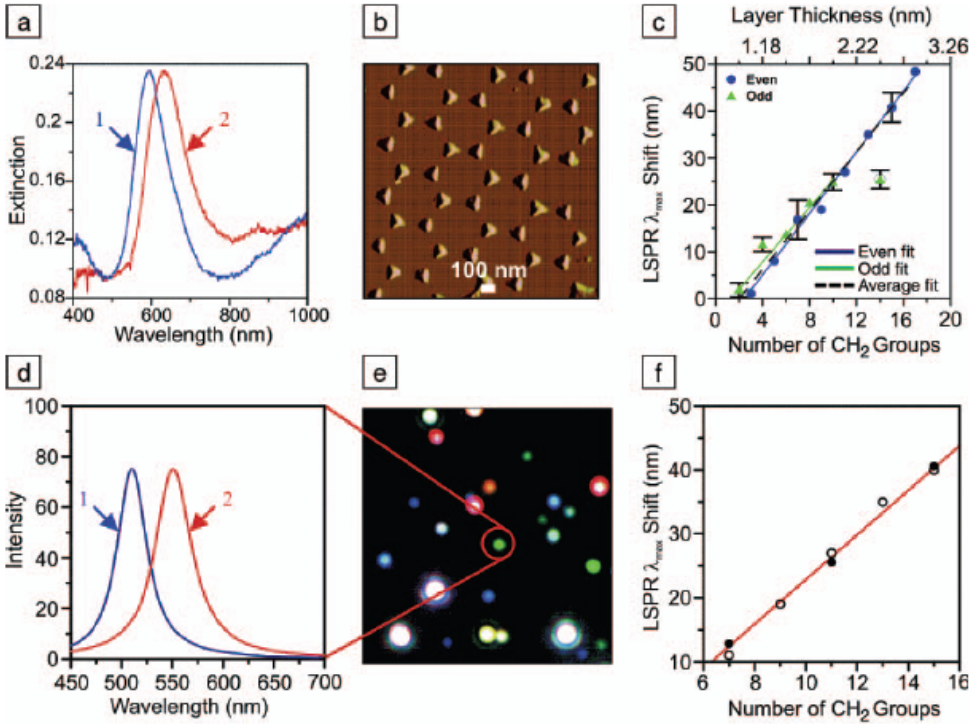

Figure 3. (top row) Localized surface plasmon resonance (LSPR) spectroscopy of a Ag nanoparticle array fabricated by nanosphere lithography in a N_2 environment: (a) Extinction spectrum of the array (curve 1) before chemical modification, wavelength of extinction maximum λ_{max} = 594.8 nm, and (curve 2) after modification with 1 mM hexadecanethiol, λ_{max} = 634.8 nm. (b) Tapping-mode atomic force microscopy (AFM) image of the array in (a); nanosphere diameter D = 390 nm, deposited mass thickness d_m = 50 nm; Ag on mica substrate; scan area, 3.0 μm^2. After solvent annealing, nanoparticle in-plane width is 100 nm and out-of-plane height is 51 nm. (c) Alkanethiol chain length dependence on the LSPR spectral peak shifts for the array. Even and odd carbon chain lengths are depicted with different symbols to emphasize the difference in the terminal bond orientation with respect to the substrate, which leads to different observed trends for the two cases. (bottom row) LSPR spectroscopy of single Ag nanoparticles produced by chemical synthesis: (d) scattering spectrum of a single Ag nanoparticle (curve 1) before chemical modification, λ_{max} = 510.2 nm, and (curve 2) after modification with 1 mM hexadecanethiol, λ_{max} = 550.9 nm. The circled nanoparticle in (e) produced the signal for these curves. (e) Dark-field resonant Rayleigh scattering image of a random array of chemically synthesized Ag nanoparticles (image dimensions, 130 $\mu m \times 130 \mu m$). (f) Alkanethiol chain length dependence on the LSPR spectral peak shifts for a single Ag nanoparticle. The open circles represent an overlay of the array data from (c). The solid circles are single nanoparticle measurements.

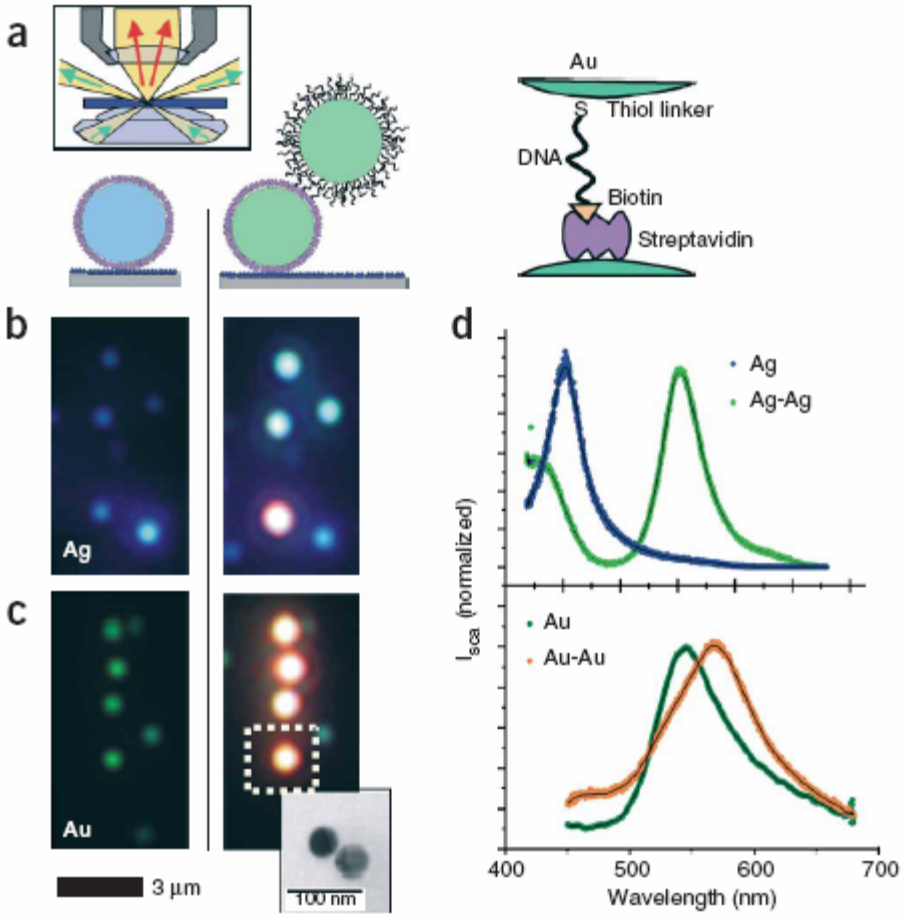

Figure 1 Color effect on directed assembly of DNA-functionalized gold and silver nanoparticles. (**a**) First, nanoparticles functionalized with streptavidin are attached to the glass surface coated with BSA-biotin (left). Then, a second particle is attached to the first particle (center), again via biotin-streptavidin binding (right). The biotin on the second particle is covalently linked to the 3′ end of a 33 base pair long ssDNA strand bound to the particle via a thiol group at the 5′ end. Inset: principle of transmission darkfield microscopy. (**b**) Single silver particles appear blue (left) and particle pairs blue-green (right). The orange dot in the bottom comes from an aggregate of more than two particles. (**c**) Single gold particles appear green (left), gold particle pairs, orange (right). Inset: representative transmission electron microscopy image of a particle pair to show that each colored dot comes from light scatted from two closely lying particles, which cannot be separated optically. (**d**) Representative scattering spectra of single particles and particle pairs for silver (top) and gold (bottom). Silver particles show a larger spectral shift (102 nm) than gold particles (23 nm), stronger light scattering and a smaller plasmon line width. Gold, however, is chemically more stable and is more easily conjugated to biomolecules via –SH, –NH2 or –CN functional groups.

should increase the electrostatic repulsion between the charged gold particles[26]. Consistent with this model, a blue-shift in the spectrum of individual nanoparticle pairs occurred when we decreased the salt concentration of our buffer (normally 0.1 M NaCl) to 0.005 M NaCl (Fig. 2a). When we restored the ionic concentration to the original

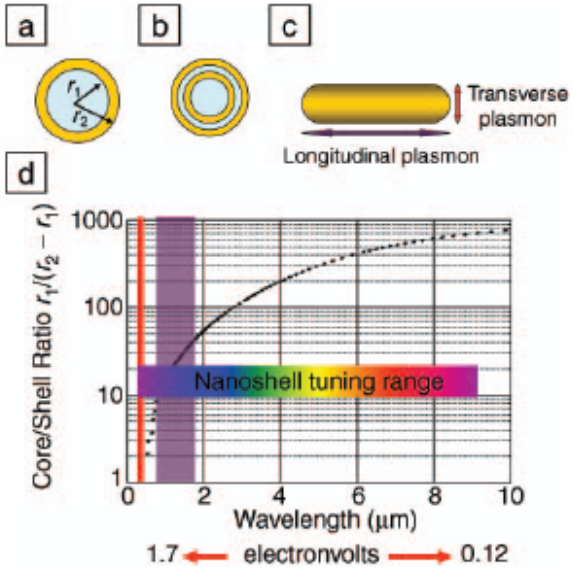

Figure 1. (a) Schematic illustration of a silica-core, gold-shell nanoshell, indicating inner (r_1) and outer (r_2) radii of the shell layers. (b) Depiction of a four-layer, concentric nanoshell. (c) Schematic illustration of a metallic nanorod. (d) Plot of nanoshell resonance as a function of core and shell dimensions, overlaid with reported spectral ranges of nanorod resonances (red, transverse plasmon; purple, longitudinal plasmon), and reported nanoshell and concentric nanoshell combined spectral range of plasmon response.

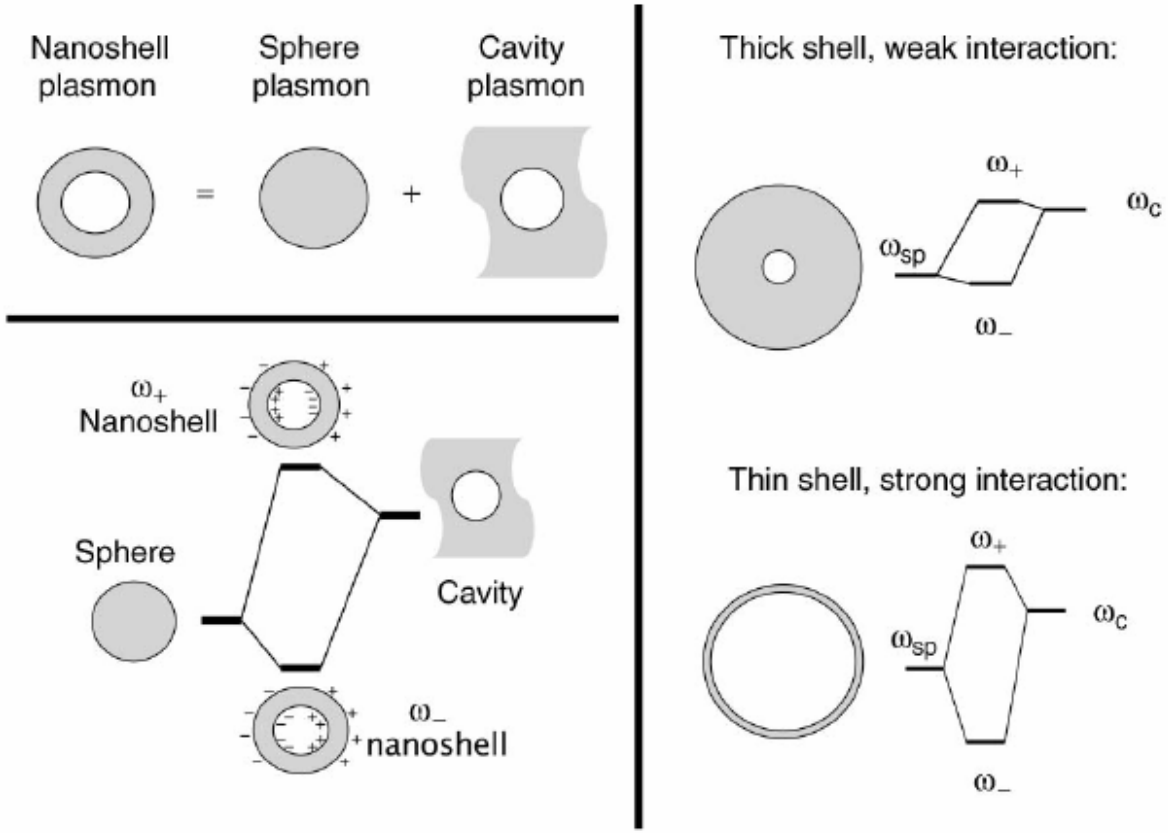

Figure 2. Plasmon hybridization and the sphere–cavity model for nanoshells: the interaction between a sphere (resonance frequency, ω_{sp}) and a cavity plasmon (resonance frequency, ω_c) is tuned by varying the thickness of the shell layer of the nanoparticle. Two hybrid plasmon resonances, the ω_- "bright," or "bonding," plasmon and the ω_+ "dark," or "anti-bonding," plasmon resonances are formed. The lower-energy plasmon couples most strongly to the optical field.

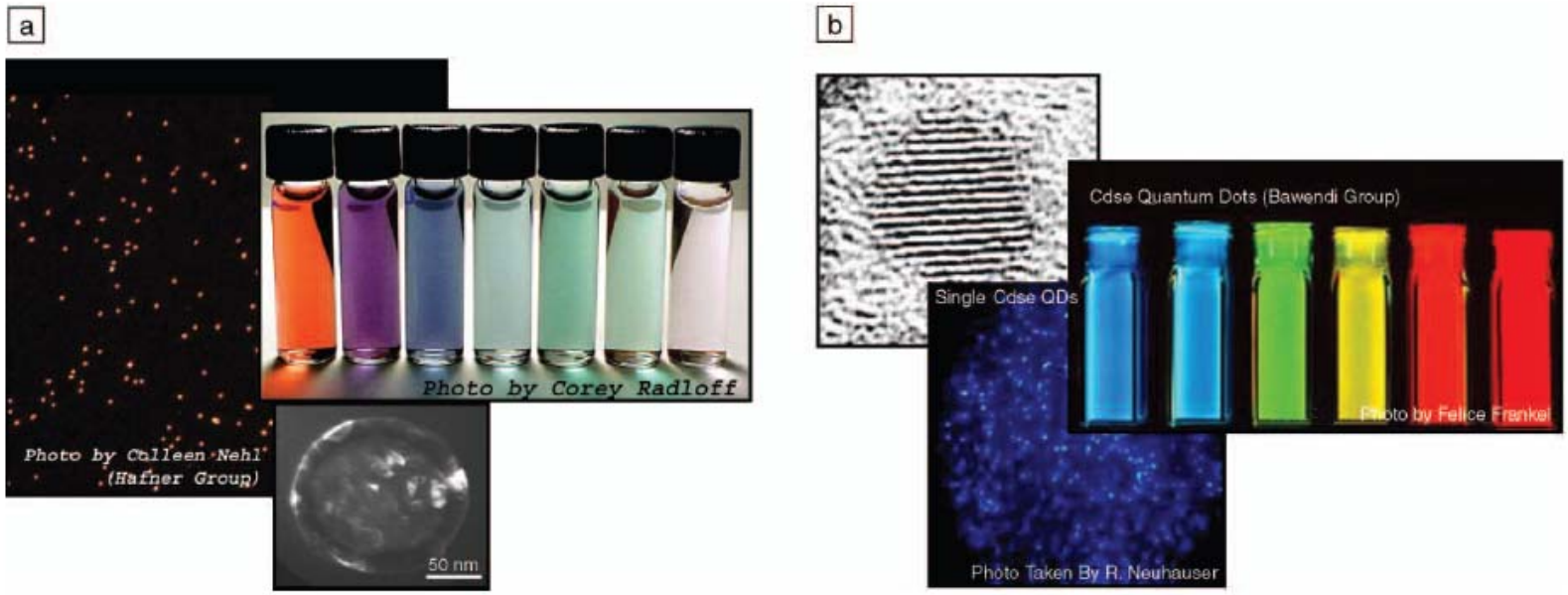

Figure 3. (a) Nanoshells are tunable plasmonic nanoparticles. Micrographs show a field of many nanoshells (large micrograph) and one nanoshell (small micrograph). Vials show nanoshells in solution. (b) Semiconductor quantum dots are tunable excitonic nanoparticles (courtesy of the Bawendi group). A field of quantum dots is displayed in the bottom image; an individual quantum dot is shown in the upper-left micrograph. Vials of quantum dots are also shown. Comparing single nanoshells to single quantum dots, nanoshells typically have a 10^6 larger absorption cross section, nominally five times the physical cross section of the nanoparticle.

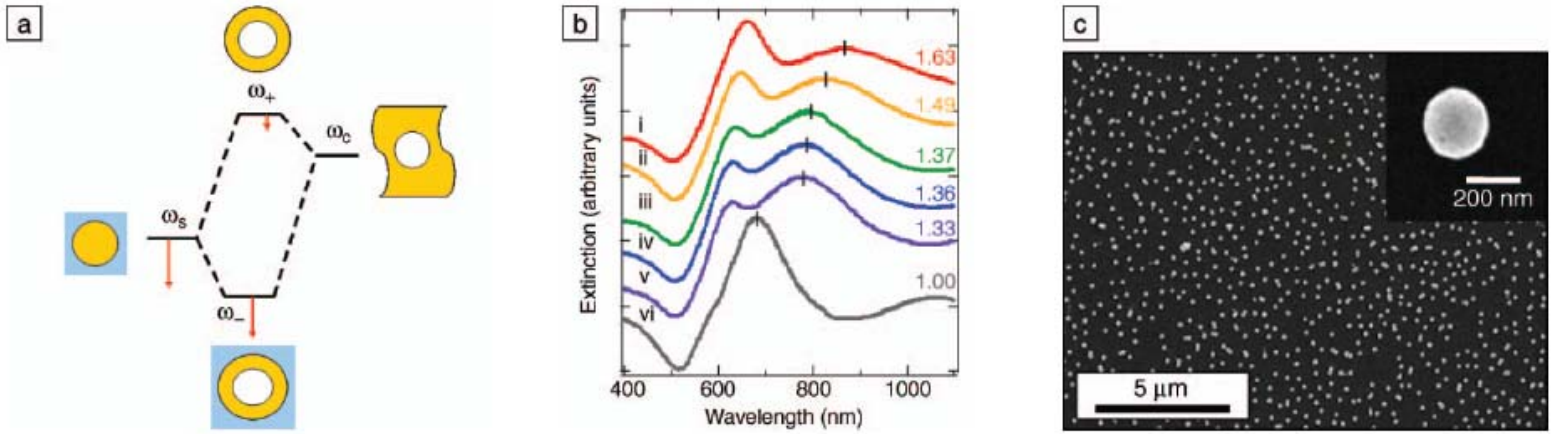

Figure 5. (a) Plasmon hybridization picture applied to surface plasmon resonance sensing with nanoshells: the low-energy "bonding" plasmon, ω_-, is sensitized to changes in its dielectric environment. The blue background schematically denotes the embedding medium for the nanoparticle. (b) Experimental curves showing plasmon resonance shifts for nanoshell-coated films in various media: (i) carbon disulfide, (ii) toluene, (iii) hexane, (iv) ethanol, (v) H_2O, and (vi) air. The index of refraction for each embedding medium is noted on the far right of the spectra. Spectra are offset for clarity. (c) Scanning electron micrograph of nanoshells deposited onto a poly(vinyl pyridine) functionalized glass surface, as used to acquire data in (b). Inset: individual nanoshell.

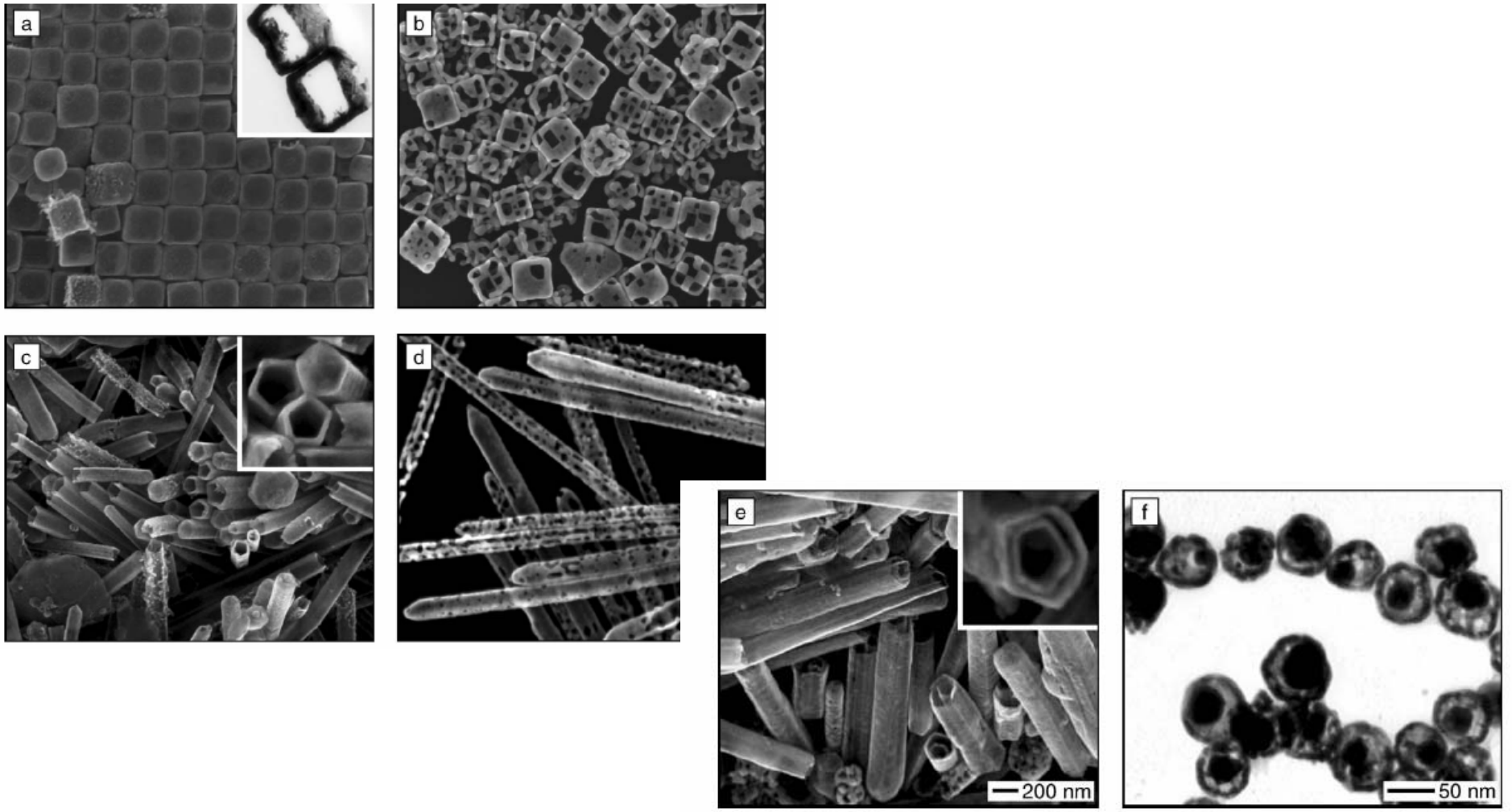

Figure 3. (a) Scanning electron microscopy (SEM) image of Au/Ag alloyed nanoboxes synthesized by reacting Ag nanocubes with $HAuCl_4$ in an aqueous medium. The inset shows a transmission electron microscopy (TEM) image of two microtomed boxes, confirming their hollow structure. (b) Addition of more $HAuCl_4$ induced the dealloying of silver from the walls and the formation of pinholes. (c), (d) Alloying and dealloying were also observed when silver nanowires served as the template. Note the hollow interior matching the pentagonal cross section of the nanowire. (e), (f) SEM and TEM images of double-walled nanotubes and nanorattles of Au/Ag alloys that were produced by combining the galvanic replacement reaction with the electroless plating of silver. The SEM images in (a)–(e) are at the same scale, as shown by the scale marker in (e); the scale of (f) is noted in the micrograph.

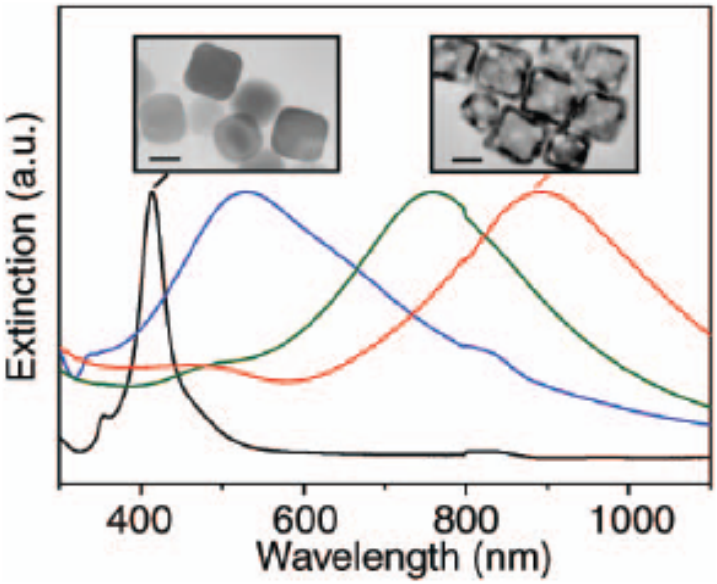

Figure 4. Transformation of 30 nm Ag nanocubes into Au/Ag alloyed nanoboxes and nanocages resulted in a continuous shift of their surface plasmon resonance (SPR) peak from 400 nm to 900 nm, which is in the transparent window of biological tissue. The SPR peak position is determined by the molar ratio between $HAuCl_4$ and Ag involved in the replacement reaction. Insets show TEM images of the cubes and cages; scale bar in each figure represents 20 nm.

INTERFACES AND THIN FILMS AS SEEN BY BOUND ELECTROMAGNETIC WAVES

Wolfgang Knoll

character of an electromagnetic mode. The component perpendicular to the interface, E_z, however, does not fall to zero abruptly, but decays exponentially with a decay length l which is a function of the angle of incidence

$$l = \frac{\lambda}{2\pi\sqrt{(n \cdot \sin\theta)^2 - 1}}, \quad \theta > \theta_c. \qquad 1.$$

Such an electromagnetic field distribution is called an evanescent wave.

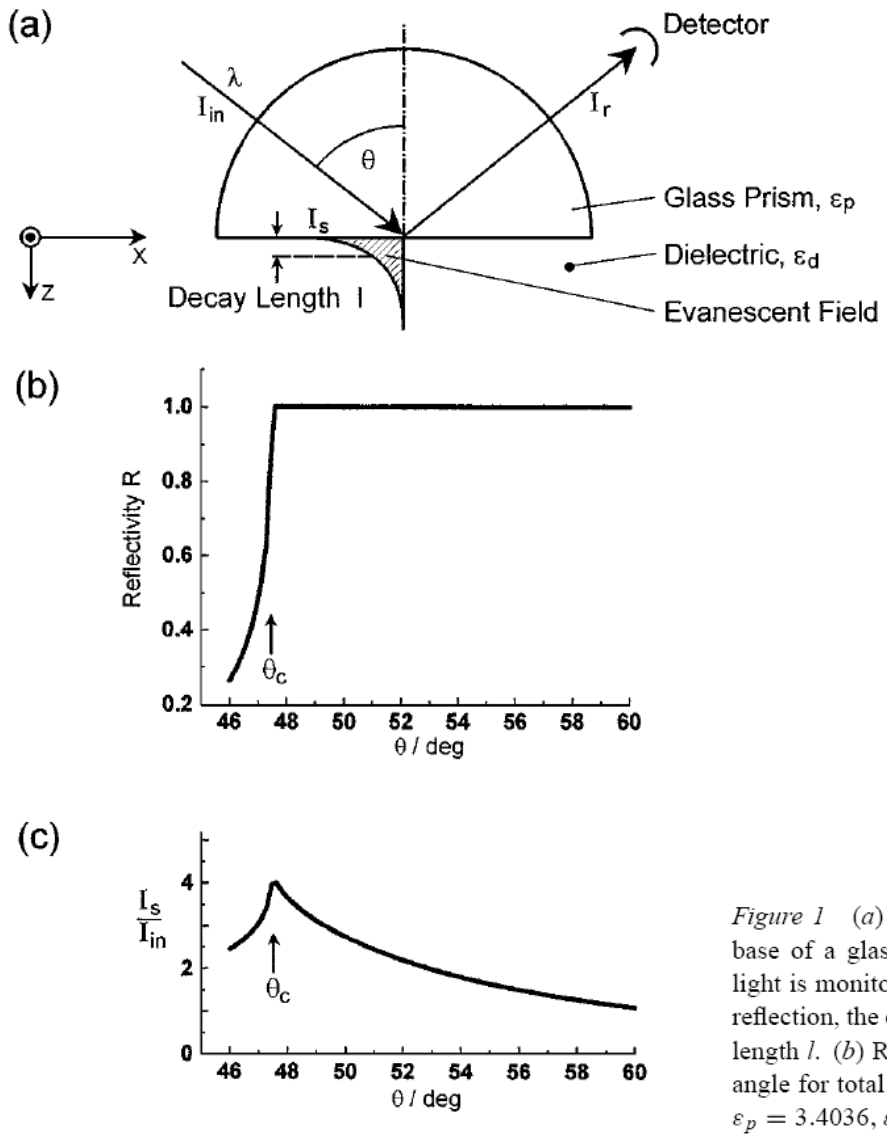

Figure 1 (*a*) Total internal reflection of a plane wave of wavelength λ and intensity I_{in} at the base of a glass prism with ε_p in contact with a dielectric medium of $\varepsilon_d < \varepsilon_p$. The reflected light is monitored with a detector. For incident angles $\theta > \theta_c$, the critical angle for total internal reflection, the evanescent field at the interface decays exponentially into the dielectric with a decay length l. (*b*) Reflectivity, i.e. I_r/I_{in}, as a function of the incident angle θ. θ_c denotes the critical angle for total internal reflection, and is given by $\sin\theta_c = \sqrt{\frac{\varepsilon_d}{\varepsilon_p}}$. The curve was calculated with $\varepsilon_p = 3.4036$, $\varepsilon_d = 1.778$. (*c*) Intensity enhancement, I_s/I_{in}, at the interface ($z = 0$) as a function of the incident angle θ.

We consider an interface in the xy-plane between two half-infinite spaces, 1 and 2, of materials the optical properties of which are described by their complex frequency-dependent dielectric functions $\tilde{\varepsilon}_1(\omega)$ and $\tilde{\varepsilon}_2(\omega)$, respectively. We ignore magnetic materials. Surface polaritons can only be excited at such an interface if the dielectric displacement $\vec{D}$ of the electromagnetic mode has a component normal to the surface ($\|\vec{z}$) which can induce a surface charge density σ,

$$(\vec{D}_2 - \vec{D}_1) \cdot \vec{z} = 4\pi\sigma. \qquad 2.$$

S-polarized light propagating along the x-direction possesses only electric field components, $\vec{E}_i$, parallel to the surface ($\|$y-direction), i.e. transversal electric (TE) waves have $\vec{E}_i = (0, E_y, 0)$, and hence are unable to excite surface polaritons. Only p-polarized light (transversal magnetic TM) modes with $E = (E_x, 0, E_z)$, or, equivalently, $\vec{H} = (0, H_y, 0)$, can couple to such modes. The resulting surface electromagnetic wave, therefore, will have the following general form

$$\vec{A}_1 = \vec{A}_{10} e^{i(\vec{k}_{x1}\vec{x} + \vec{k}_{z1}\vec{z} - \omega t)} \text{ in medium } 1, z < 0 \qquad 3a.$$

and

$$\vec{A}_2 = \vec{A}_{20} e^{i(\vec{k}_{x2}\vec{x} - \vec{k}_{z2}\vec{z} - \omega t)} \text{ in medium } 2, z > 0, \qquad 3b.$$

where $\vec{A}$ stands for $\vec{E}$ and $\vec{H}$; $\vec{k}_{x1}$, and $\vec{k}_{x2}$ are the wavevectors in the x-direction; $\vec{k}_{z1}$, and $\vec{k}_{z2}$ those in the z-direction, i.e. normal to the interface; and ω is the angular frequency. Both fields $\vec{E}$ and $\vec{H}$ must fulfill the Maxwell equations:

$$\nabla \cdot \vec{H} = 0, \tag{4.}$$

$$\nabla \cdot \vec{E} = 0, \tag{5.}$$

$$\nabla \times \vec{E} + \frac{1}{c}\frac{\partial \vec{H}}{\partial t} = 0, \tag{6.}$$

$$\nabla \times \vec{H} - \frac{\varepsilon}{c}\frac{\partial \vec{E}}{\partial t} = 0, \tag{7.}$$

with c being the speed of light in vacuo and ε the dielectric function of the material. The tangential components of $\vec{E}$ and $\vec{H}$ have to be equal at the interface, i.e.

$$E_{x1} = E_{x2} \tag{8.}$$

and

$$H_{y1} = H_{y2}. \tag{9.}$$

From Equation 8 it follows immediately that $k_{x1} = k_{x2} = k_x$. On the other hand, it follows from Equations 3 and 7 that

$$k_{z1} H_{y1} = \frac{\omega}{c} \varepsilon_1 E_{x1} \tag{10.}$$

and

$$k_{z2} H_{y2} = -\frac{\omega}{c} \varepsilon_2 E_{x2}. \tag{11.}$$

This leads to the only nontrivial solution if:

$$\frac{k_{z1}}{k_{z2}} = -\frac{\varepsilon_1}{\varepsilon_2}. \tag{12.}$$

Equation 12 indicates that surface electromagnetic modes can only be excited at interfaces between two media with dielectric constants of opposite sign.

Here we are dealing with the interface between a metal with its complex dielectric function ($\tilde{\varepsilon}_m = \varepsilon'_m + i\varepsilon''_m$) and a dielectric material ($\tilde{\varepsilon}_d = \varepsilon'_d + i\varepsilon''_d$), hence, with coupling the collective plasma oscillations of the nearly free electron gas in a metal to an electromagnetic field (5). These excitations are called plasmon surface polaritons (PSP) or surface plasmons, for short. From Equations 6, 7, 10, and 11 we obtain

$$k_x^2 + k_{zd}^2 = \left(\frac{\omega}{c}\right)^2 \varepsilon_d \qquad 13.$$

or

$$k_{zd} = \sqrt{\varepsilon_d \left(\frac{\omega}{c}\right)^2 - k_x^2}. \qquad 14.$$

With Equation 12 this leads to the dispersion relationships (i.e. the energy-momentum relation) for surface plasmons at a metal/dielectric interface:

$$k_x = \frac{\omega}{c}\sqrt{\frac{\varepsilon_m \cdot \varepsilon_d}{(\varepsilon_m + \varepsilon_d)}}. \qquad 15.$$

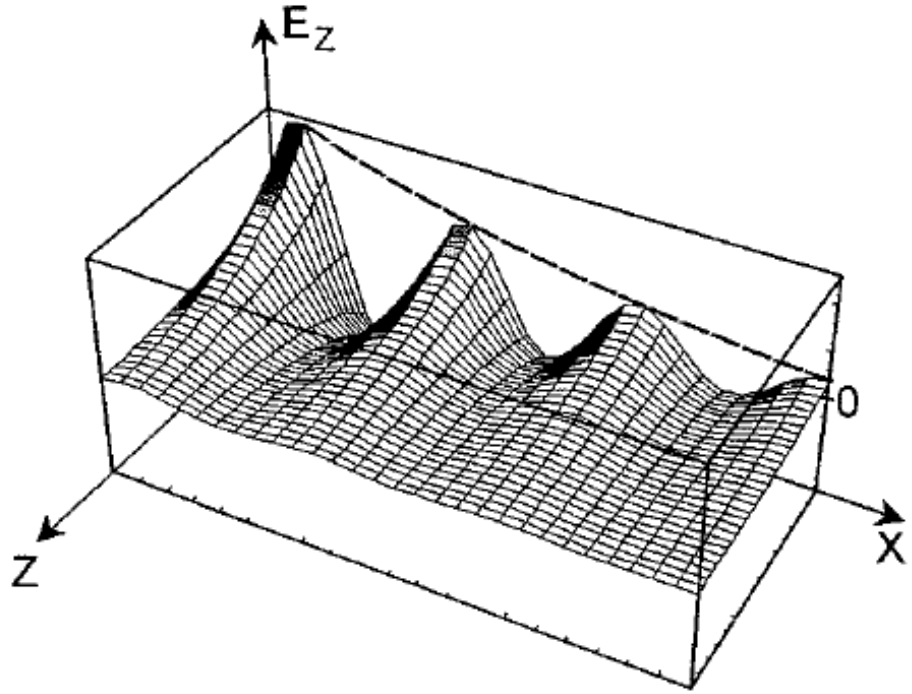

Figure 2 Schematic of the evanescent character of a surface plasmon mode excited at a metal/dielectric interface in the x-, y-plane propagating as a damped oscillatory wave in the x-direction. The electric field components along the z-direction, normal to the interface, decay exponentially, here shown for the E_z component.

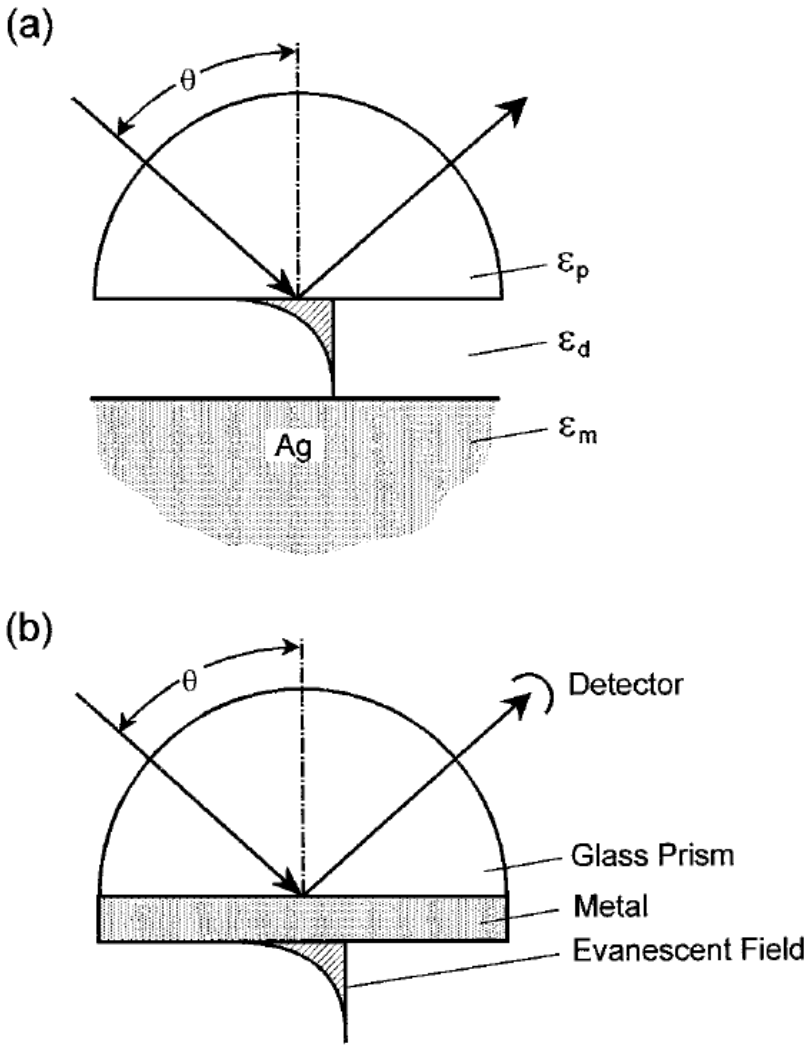

Figure 4 (*a*) The Otto configuration is based on the total internal reflection of a plane wave incident at an angle θ at the base of a prism. The evanescent tail of this inhomogeneous wave can excite PSP states at an Ag-dielectric interface, provided the coupling gap is sufficiently narrow. (*b*) Attenuated total internal reflection (ATR) construct for PSP excitation in the Kretschmann geometry. A thin metal film ($d \sim 50$ nm) is evaporated onto the base of the prism and acts as a resonator driven by the photon field incident at an angle θ.

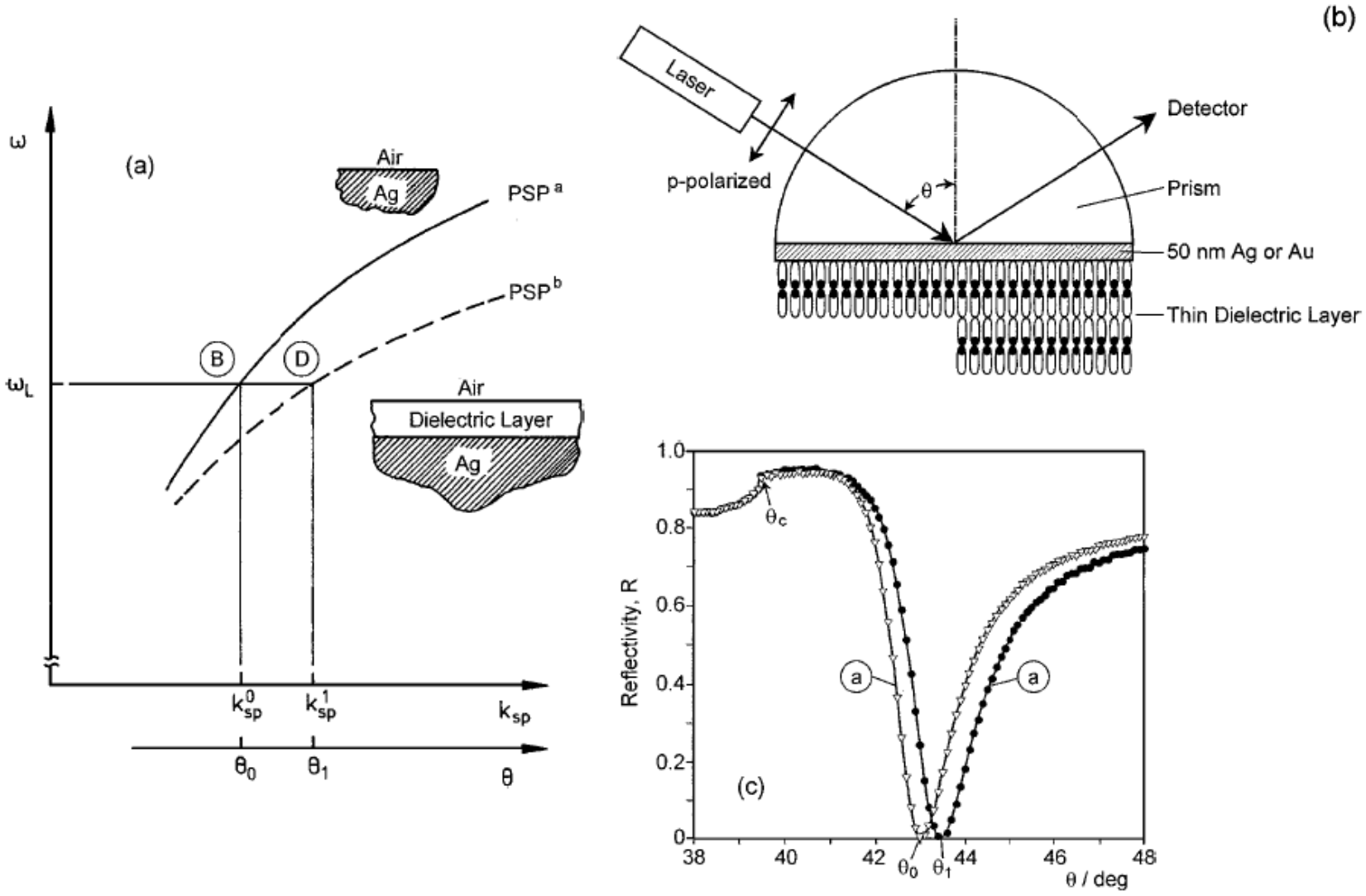

after self-assembling a monomolecular layer of HS-$(CH_2)_{21}$-OH. The symbols are experimental data points; the full curves are Fresnel fits with $\varepsilon_{BK7} = 2.29$, $\tilde{\varepsilon}_{Au} = -12.45 + i \cdot 1.3$, $d_{Au} = 46.9$ nm, $\varepsilon_{layer} = 2.1025$, $d_{layer} = 2.65$ nm. Data were taken at $\lambda = 633$ nm in air.

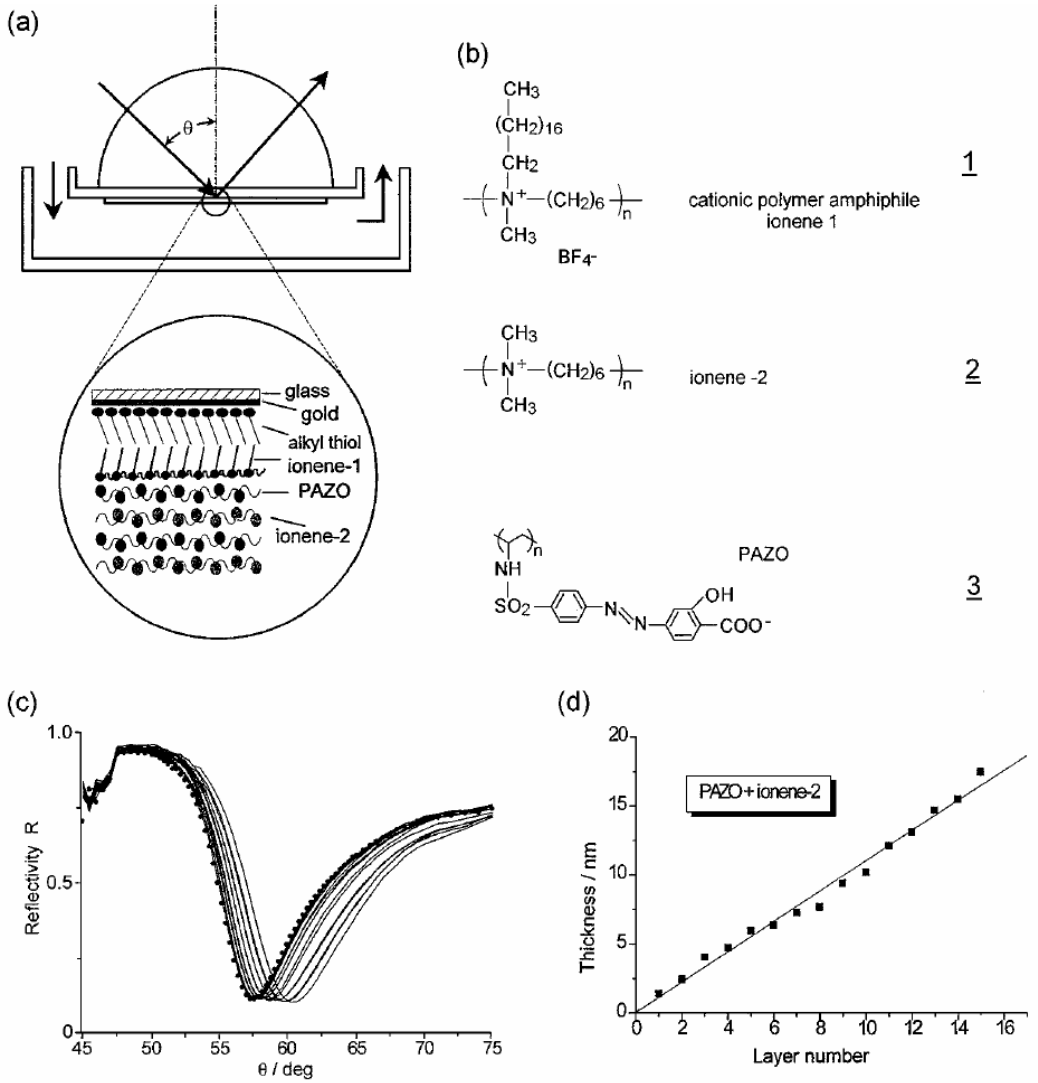

Figure 14 (*a*) Experimental construct for on-line surface plasmon optical observation of the alternating deposition of cationic and anionic polymers from solution to an Au substrate precoated by an alkyl thiol and an ionene-1 monolayer [refer to (*b*)]. The build-up architecture is given in the enlargement. (*b*) Structural formulas of the employed materials. (*c*) Series of ATR scans taken after each polyelectrolyte monolayer deposition. (*d*) Thickness increase as obtained from the ATR scans given in (*c*).

Probing Single Molecules and Single Nanoparticles by Surface-Enhanced Raman Scattering

SCIENCE • VOL. 275 • 21 FEBRUARY 1997

Shuming Nie* and Steven R. Emory

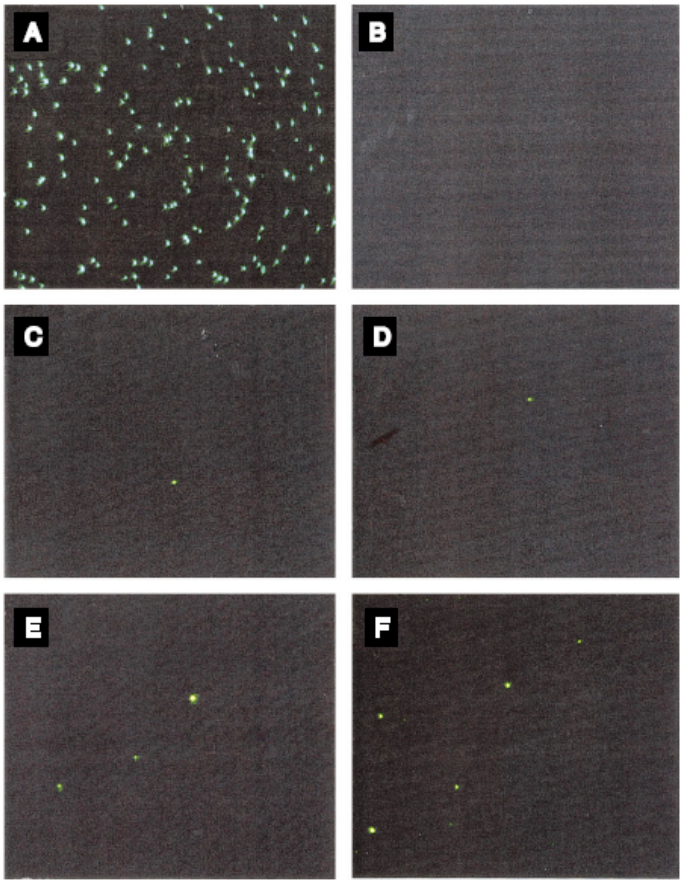

Fig. 1. Single Ag nanoparticles imaged with evanescent-wave excitation. Total internal reflection of the laser beam at the glass-liquid interface was used to reduce the laser scattering background. The instrument setup for evanescent-wave microscopy was adapted from Funatsu *et al.* (*11*). The images were directly recorded on color photographic film (ASA-1600) with a 30-s exposure by a Nikon 35-mm camera attached to the microscope. (**A**) Unfiltered photograph showing scattered laser light from all particles immobilized on a polylysine-coated surface. (**B**) Filtered photographs taken from a blank Ag colloid sample (incubated with 1 mM NaCl and no R6G analyte molecules). (**C**) and (**D**) Filtered photographs taken from a Ag colloid sample incubated with 2×10^{-11} M R6G. These images were selected to show at least one Raman scattering particle. Different areas of the cover slip were rapidly screened, and most fields of view did not contain visible particles. (**E**) Filtered photograph taken from Ag colloid incubated with 2×10^{-10} M R6G. (**F**) Filtered photograph taken from Ag colloid incubated with 2×10^{-9} M R6G. A high-performance bandpass filter was used to remove the scattered laser light and to pass Stokes-shifted Raman signals from 540 to 580 nm (920 to 2200 cm^{-1}). Continuous-wave excitation at 514.5 nm was provided by an Ar ion laser. The total laser power at the sample was 10 mW. Note the color differences between the scattered laser light in (A) and the red-shifted light in (C) through (F).

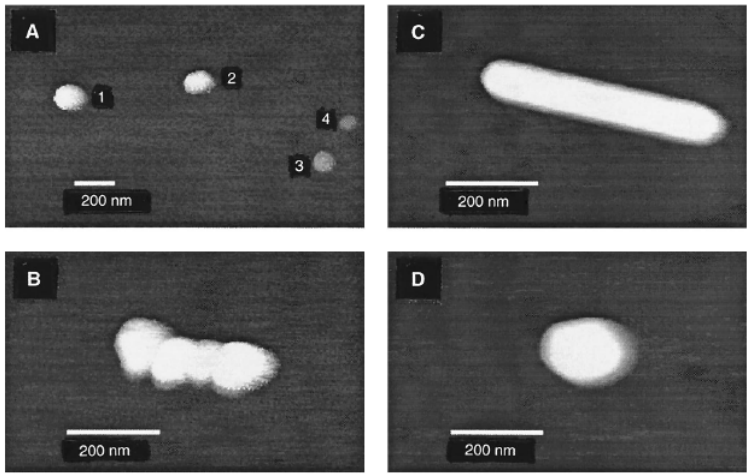

Fig. 2. Tapping-mode AFM images of screened Ag nanoparticles. (**A**) Large area survey image showing four single nanoparticles. Particles 1 and 2 were highly efficient for Raman enhancement, but particles 3 and 4 (smaller in size) were not. (**B**) Close-up image of a hot aggregate containing four linearly arranged particles. (**C**) Close-up image of a rod-shaped hot particle. (**D**) Close-up image of a faceted hot particle.

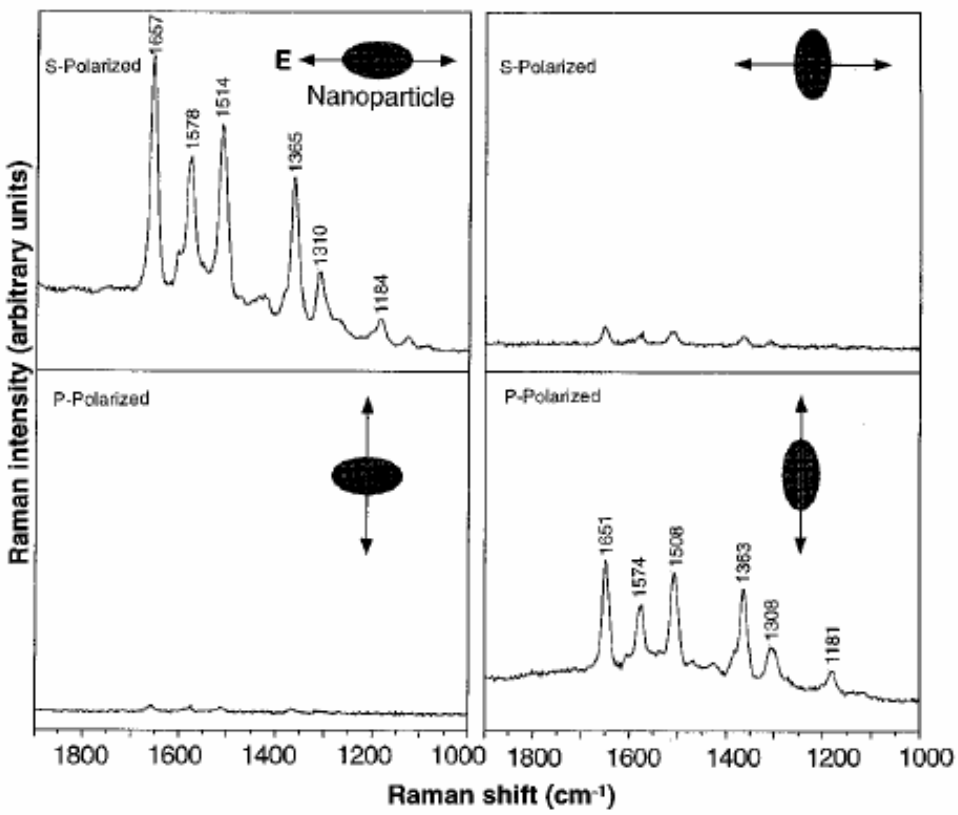

Fig. 3. Surface-enhanced Raman spectra of R6G obtained with a linearly polarized confocal laser beam from two Ag nanoparticles. The R6G concentration was 2×10^{-11} M, corresponding to an average of 0.1 analyte molecule per particle. The direction of laser polarization and the expected particle orientation are shown schematically for each spectrum. Laser wavelength, 514.5 nm; laser power, 250 nW; laser focal radius, ~250 nm; integration time, 30 s. All spectra were plotted on the same intensity scale in arbitrary units of the CCD detector readout signal.

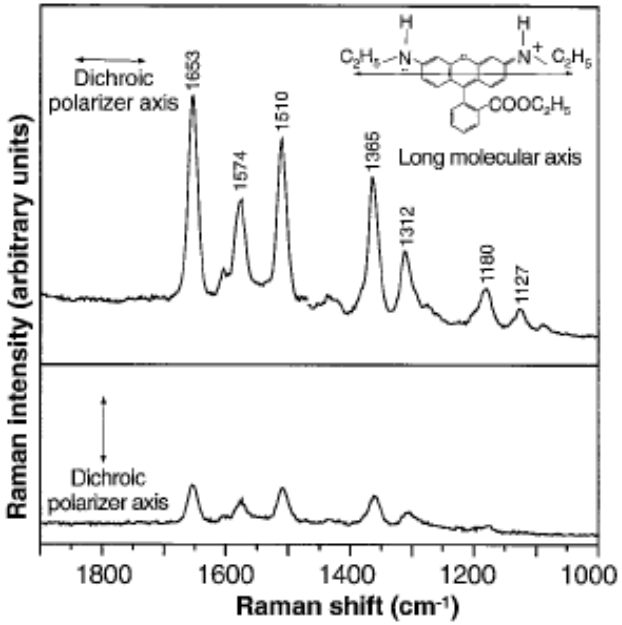

Fig. 4. Emission-polarized surface-enhanced Raman signals of R6G observed from a single Ag nanoparticle with a polarization-scrambled confocal laser beam. A dichroic sheet polarizer was rotated 90° to select Raman scattering signals polarized parallel (upper spectrum) or perpendicular (lower spectrum) to the long molecular axis of R6G. (**Inserts**) Structure of R6G, the electronic transition dipole (along the long axis when excited at 514.5 nm), and the dichroic polarizer orientations. Other conditions as in Fig. 3.

troscopic signatures of adsorbed molecules. For single rhodamine 6G molecules adsorbed on the selected nanoparticles, the intrinsic Raman enhancement factors were on the order of 10^{14} to 10^{15}, much larger than the ensemble-averaged values derived from conventional measurements. This enormous enhancement leads to vibrational Raman signals that are more intense and more stable than single-molecule fluorescence.

Electromagnetic contributions to single-molecule sensitivity in surface-enhanced Raman scattering

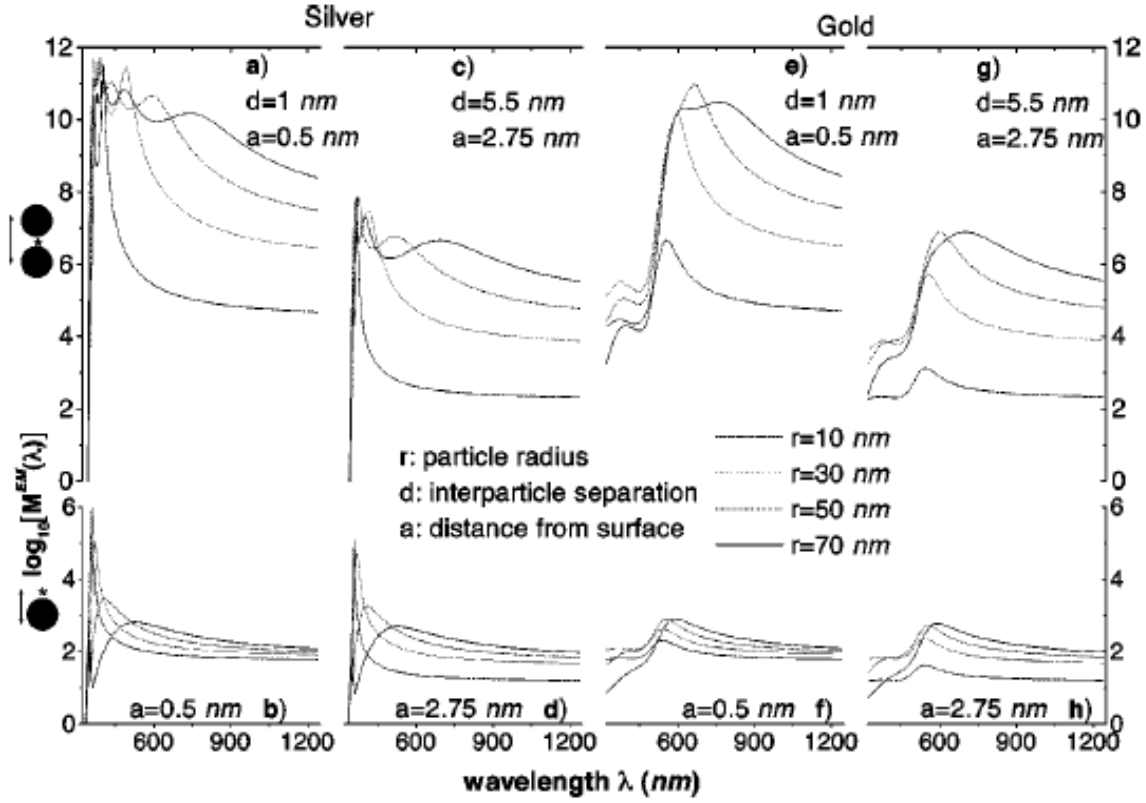

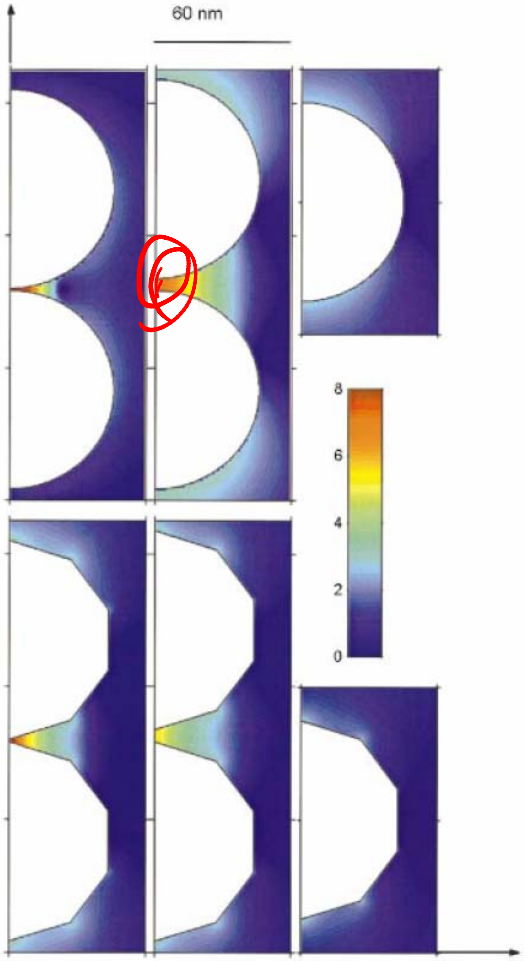

FIG. 3. (Color) EM-enhancement factor M^{EM} at a cross section through six different silver particle configurations. The wavelength of the incident field is $\lambda = 514.5$ nm with vertical polarization. The left-hand column illustrates the EM enhancement for dimer configurations of two spheres (top) and two polygons (bottom) with a separation of 1 nm. The middle column shows the same situation, but with a separation distance of 5.5 nm. The right-hand column shows the case of an isolated single particle. All particles share a common largest dimension of 90 nm. Note that the color scale from dark blue to dark red is logarithmic, covering the interval $10^0 < M^{EM} < 10^8$. Regions with enhancement outside this interval are shown in dark blue and dark red, respectively.

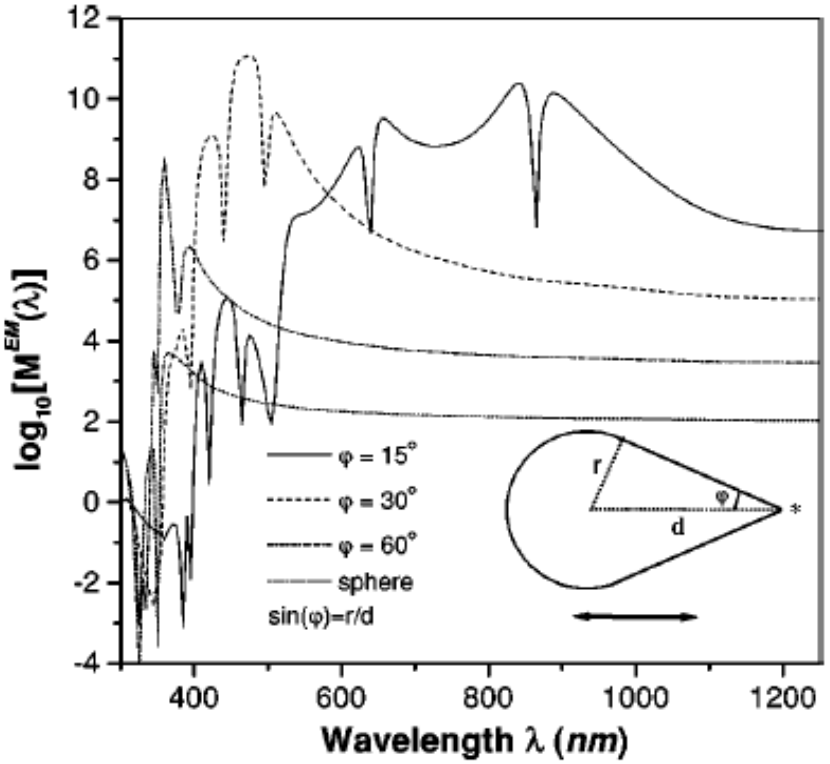

FIG. 5. EM-enhancement factor for a rotationally symmetric silver droplet as a function of the angle defining the opening edge ϕ. The field is polarized parallel to the axis of the droplet and the evaluation position (star) is located 0.5 nm outside the tip. As the droplet becomes sharper the enhancement increases several orders of magnitude.

Nanosphere Arrays with Controlled Sub-10-nm Gaps as Surface-Enhanced Raman Spectroscopy Substrates

J. AM. CHEM. SOC. 2005, *127*, 14992−14993

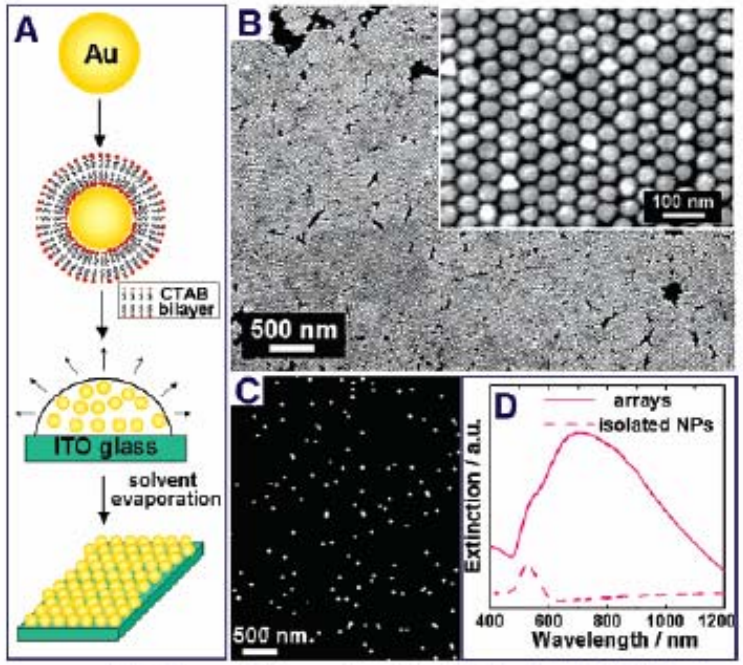

Figure 1. (A) Schematic illustration of the fabrication of sub-10-nm gap Au NP arrays. (B) SEM image of the arrays. (C) SEM image of monolayer of isolated Au NPs on ITO glass. (D) Vis−NIR extinction spectrum of the monolayer of isolated Au NPs and arrays.

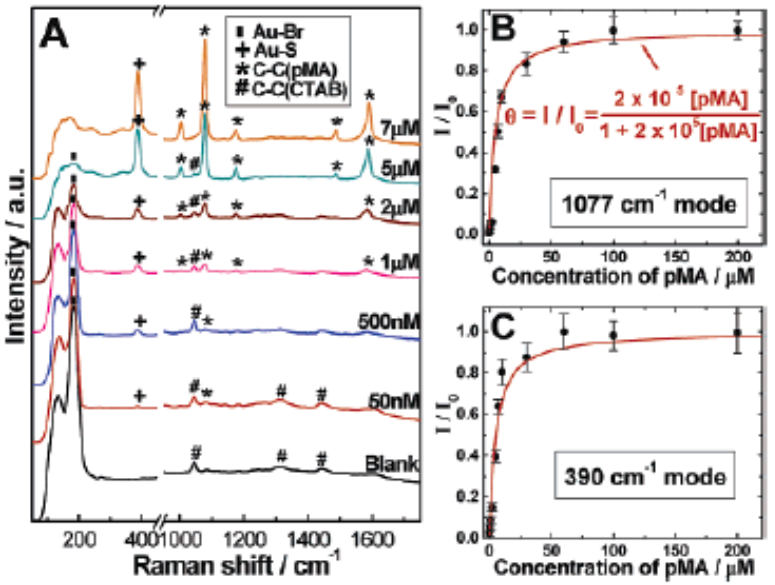

Figure 2. (A) SERS spectra of 5 μL of pMA with different concentrations deposited on the NP arrays. The excitation laser wavelength is 785 nm. Adsorption isotherm of pMA on the NP arrays obtained according to (B) 1077 and (C) 390 cm^{-1} modes in the SERS spectra. I_0 is the peak intensity of a saturated pMA monolayer.

Profiling the Near Field of a Plasmonic Nanoparticle with Raman-Based Molecular Rulers

NANO LETTERS

2006
Vol. 6, No. 10
2338−2343

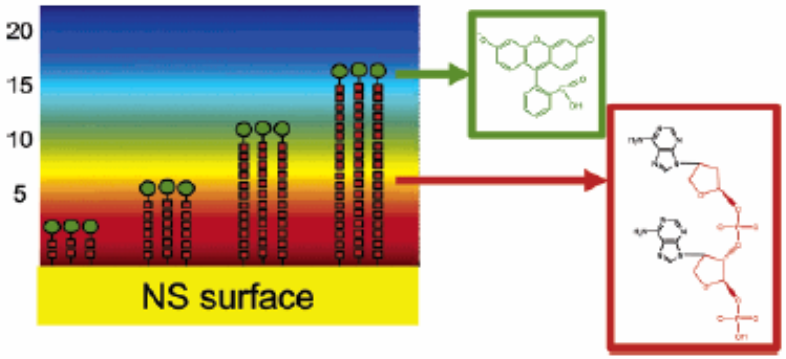

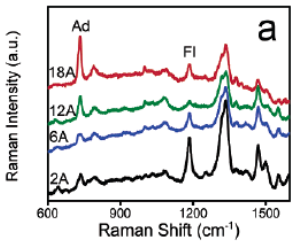

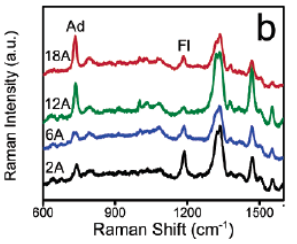

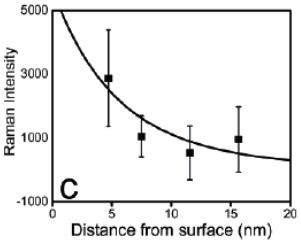

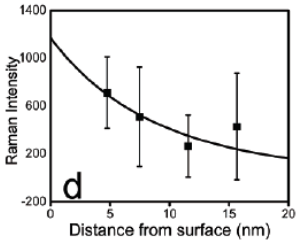

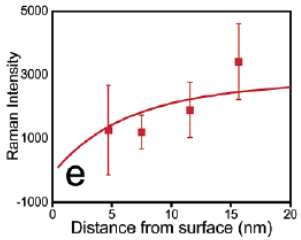

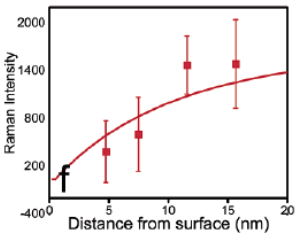

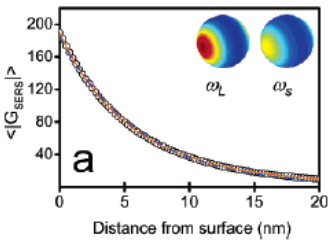

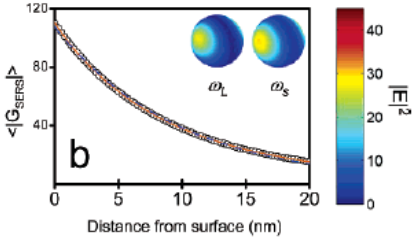

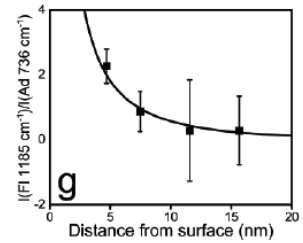

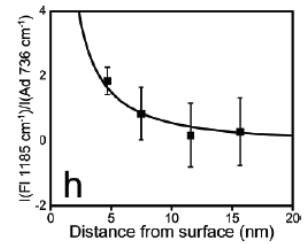

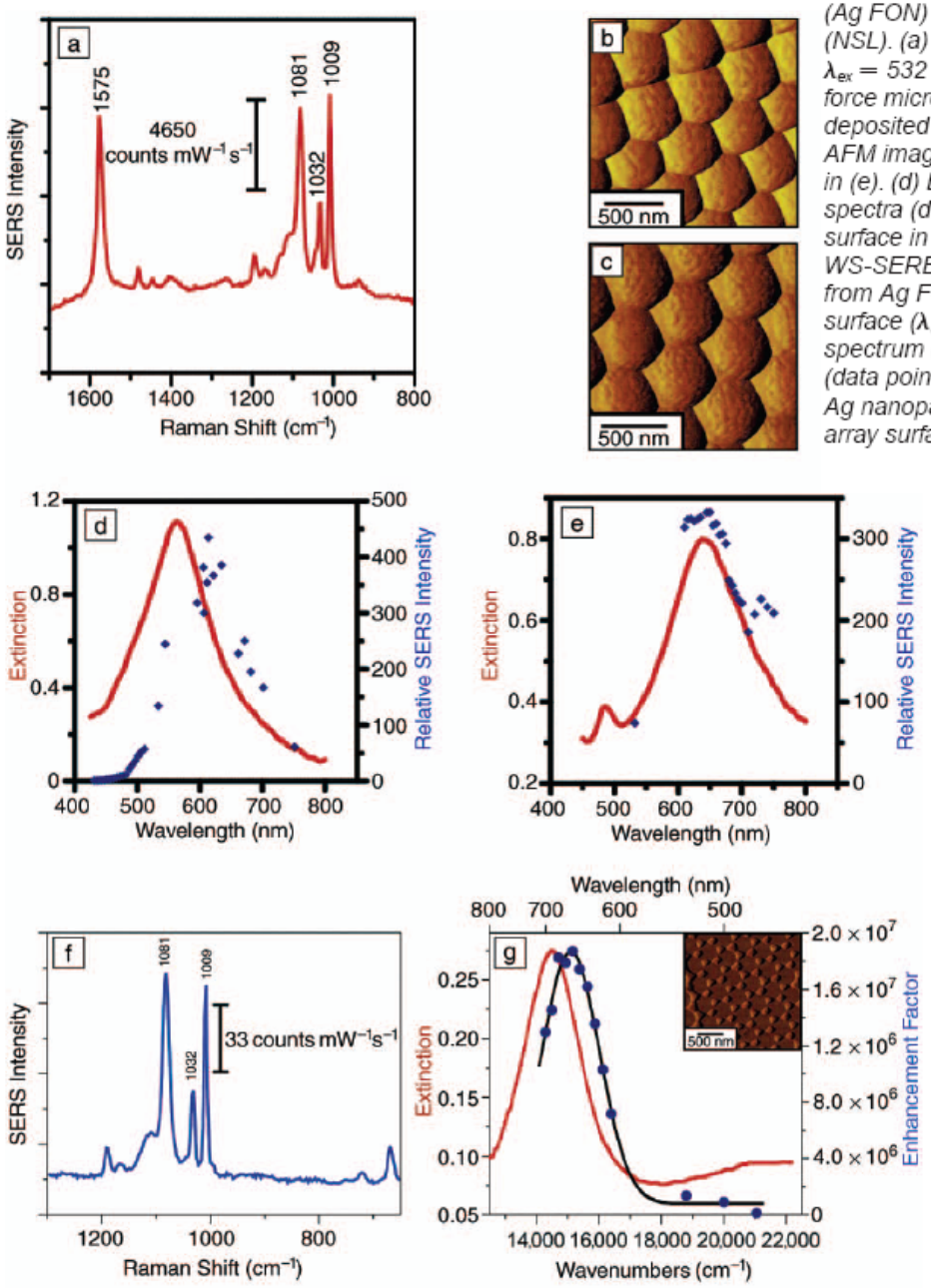

Figure 6. Localized surface plasmon resonance (LSPR), surface-enhanced Raman spectroscopy (SERS), and wavelength-scanned surface-enhanced Raman excitation spectroscopy (WS-SERES) results for benzenethiol adsorbed on Ag film-over-nanosphere (Ag FON) surfaces and nanoparticle arrays fabricated by nanosphere lithography (NSL). (a) SERS spectrum measured from Ag FON surface with excitation wavelength λ_{ex} = 532 nm, power = 3.0 mW, and 100 s data acquisition time. (b) Contact-mode atomic force microscopy (AFM) image of Ag FON surface (nanosphere diameter D = 410 nm, deposited mass thickness d_m = 200 nm) used for SERS in (a). (c) Contact-mode AFM image of Ag FON surface (D = 500 nm, d_m = 250 nm) used for WS-SERES in (e). (d) LSPR spectrum (solid line, λ_{max} = 562 nm, FWHM = 144 nm) and WS-SERES spectra (data points) for the 1081 cm^{-1} band of benzenethiol measured from the Ag FON surface in (b). (e) LSPR spectrum (solid line, λ_{max} = 638 nm, FWHM = 131 nm) and WS-SERES spectra (data points) for the 1081 cm^{-1} band of benzenethiol measured from Ag FON surface in (c). (f) SERS spectrum measured from Ag nanoparticle array surface (λ_{ex} = 532 nm, power = 3.0 mW, 100 s data acquisition time). (g) LSPR spectrum (solid line, λ_{max} = 688 nm, FWHM = 95 nm) and WS-SERES spectra (data points) for the 1081 cm^{-1} band of benzenethiol measured from a Ag nanoparticle array surface. (inset) Tapping-mode AFM image of a representative array surface.

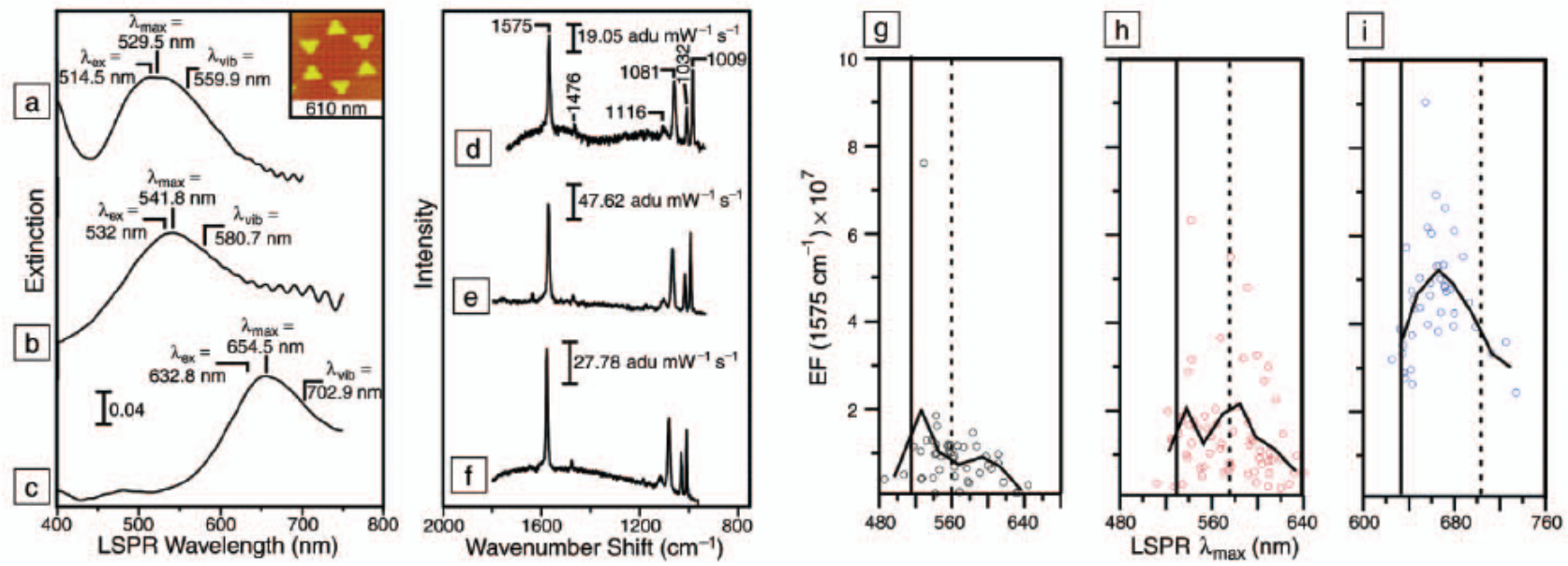

Figure 5. (a)–(f) Correlated, spatially resolved, localized surface plasmon resonance (LSPR) and surface-enhanced Raman spectroscopy (SERS) results for benzenethiol adsorbed on Ag nanoparticle arrays fabricated by nanosphere lithography. (a), (d) Ag nanoparticles fabricated with nanosphere diameter D = *280 nm and deposited mass thickness* d_m = *36 nm, probed with an excitation wavelength* λ_{ex} = *514.5 nm, power = 0.7 mW. A representative atomic force micrograph of the substrate is shown in the inset. (b), (e) Ag nanoparticles fabricated with* D = *280 nm,* d_m = *36 nm, probed with* λ_{ex} = *532.0 nm, power = 0.7 mW. (c), (f) Ag nanoparticles fabricated with* D = *400 nm,* d_m = *56 nm, probed with* λ_{ex} = *632.8 nm, power = 1.2 mW. (g)–(i) Plasmon-sampled surface-enhanced Raman excitation spectroscopy (PS-SERES) results for the 1575 cm^{-1} band of benzenethiol with three different excitation wavelengths: (g)* λ_{ex} = *514.5 nm, (h)* λ_{ex} = *532.0 nm, and (i)* λ_{ex} = *632.8 nm. For each* λ_{ex}, *both the wavelength location of the excitation (solid line) and the scattering (dashed line) are marked. The overlaid curves represent the bin-averaged values of the LSPR* λ_{max} *and the enhancement factor. Bin widths are (g) 24 nm, (h) 16 nm, and (i) 16 nm.*